The Pennsylvania State University
The Graduate School
Eberly College of Science

UNDERSTANDING AND CONTROLLING THE KINETICS OF ELECTRON TRANSFER EVENTS IN THE WATER-SPLITTING DYE-SENSITIZED PHOTOELECTROCHEMICAL CELL

A Dissertation in
Chemistry
by
Nicholas S. McCool

Submitted in Partial Fulfillment
of the Requirements
for the Degree of

Doctor of Philosophy

August 2016

The dissertation of Nicholas S. McCool was reviewed and approved* by the following:

Thomas E. Mallouk
Evan Pugh Professor of Chemistry
Dissertation Advisor
Chair of Committee
Chair of the Chemistry Department

John Asbury
Associate Professor of Chemistry

Benjamin J. Lear
Associate Professor of Chemistry

Chris Giebink
Assistant Professor of Electrical Engineering

*Signatures are on file with the Graduate School

Abstract

Water-splitting dye-sensitized photoelectrochemical cells utilize a sensitized metal oxide and water-splitting catalyst in order to split water in to oxygen and hydrogen gas as a possible clean, renewable source of molecular hydrogen. Upon light absorption, the excited dye molecule injects an electron into the conduction band of the metal oxide. Once in the electrode, the electron percolates through the material through a complicated network of trapping and detrapping events to a dark cathode where protons are reduced to hydrogen. The holes on the dye molecules diffuse across the electrode surface to catalytic water oxidation particles. These particles oxidize water to protons and oxygen, thereby using water as a clean, renewable source of protons and electrons. Despite a growing amount of research in molecular sensitizers, electrode material and catalysts, power conversion efficiency remains very low. In this dissertation, we focus on understanding and controlling the electron transfer events that dictate the efficiency of these devices.

Chapter 1 presents an overview of the development of water oxidation systems, originating with simple UV-driven water oxidation at bare metal oxide surfaces and moving in to the more complex molecular sensitizer, metal oxide support and water splitting catalyst triad largely used today. We also discuss the corresponding light-driven cathode system and the potential for developing a 2-photon 1-electron Z-scheme through utilizing both systems in conjunction. Chapter 2 discusses the electron injection and recombination dynamics in various model metal oxide systems that represent the systems most commonly used for water splitting and analyzes the impact of a core/shell structure on charge injection. In Chapter 3, we revisit proton intercalation in order to demonstrate how proton-induced trap states impact overall charge mobility and stability as well as how these impact overall device performance. Chapter 4 extends on the previous study to determine the effect of shell thickness on charge injection dynamics in an energy-cascade core/shell structure. Chapter 5 expands on this by utilizing a wide band-gap semiconductor to control injection and recombination kinetics. Finally, Chapter 6 examines a monomeric iridium molecule, which has previously been shown to negatively impact device performance, as a precursor for an active, single-site water oxidation catalyst, as well as discusses the recent observations of adventitious catalysis.

TABLE OF CONTENTS

List of Figures

List of Tables

List of Schemes

Acknowledgements

Without doubt, pursuing a Ph.D. has been one of the most difficult experiences of my life. That, in itself, is something to be thankful for in many ways. I have learned a great deal about myself during this time. However, I am also fortunate enough to be surrounded by a wealth of supportive friends and family who have always been there to celebrate with me at my successes, but just as importantly there to support me through my struggles. First and foremost, I want to thank my advisor, Tom Mallouk. For 5 years, Tom has allowed me to study anything that interested me and to spearhead my own projects, while remaining at my side, ready to assist me if I ever faltered. Despite the fact that this sometimes resulted in a difficult road, I readily accepted the challenge as I know it has allowed me to grow both as an individual and a scientist.

I also would like to thank my committee, Ben Lear, Mary Beth Williams, John Asbury, and Chris Giebink, for their continuing support and willingness to guide me through my graduate career.

I want to thank the all of members of the Mallouk lab, both past and present. Specifically, I would like to thank a few previous members, John Swierk, Nella Vargas-Barbosa and Megan Strayer. Over the past couple of years, John has been a great mentor, teammate, and friend. He has had a substantial influence on my time at Penn State and I easily would not have made it to where I am today without his help and guidance. Megan and Nella both have been my friends and sounding boards in the Mallouk lab from day one. They have been the kind of friends that one needs in a stressful environment; supportive but realistic. They have been my crutch when I needed support, are always open for scientific discussion if I'm struggling, and my smack in the face when I need to be snapped out of it. Their honesty, coupled with unyielding support and friendship, has made them two of my very closest friends.

To my friends that I have had for many years before embarking on this journey, I also wish to say thank you. They have stuck with me through this hefty roller coaster ride and are always available to distract me with lengthy chats about nonsense, no matter how long it has been since we have last spoke.

And finally, to my family; my parents, Brandon and Megan, I wish to express my deepest thanks. Thank you for everything. Thank you for your encouragement when I felt

like I was pounding into a wall. Thank you for continuing to believe in me in the times when I felt most down. Mom and Dad, thank you for always being there for me and being a place where I know I can always return to. Brandon, thank you for your support and always giving me a reason to smile; your efforts to always boost my mood were certainly not lost on me. And Megan, thank you for sticking with me through it all. You willingly put up with me when I get overly excited about science and ramble on about what cool things I'm doing, but also when I feel down and out, wondering if I want to continue with it. Since the day we met, you have been there to cheer me on or boost me up, no matter what I've needed.

This has been both a wonderful and difficult time in my life, and I know without any of you, I would not be where I am today.

Chapter 1

Parameters That Control the Performance of Water-Splitting Dye-Sensitized Photoelectrochemical Cells: Injection, Charge Mobility, and Identity of the Dye Anchoring Group

Nicholas S. McCool,[1] Thomas E. Mallouk[1,3,4]

[1]Department of Chemistry, [3]Department of Biochemistry and Molecular Biology, and [4]Department of Physics, The Pennsylvania State University, University Park, Pennsylvania 16802 United States

1.1 Introduction

Water-splitting dye-sensitized photoelectrochemical cells (WS-DSPECs) are an adaptation of the Grätzel dye-sensitized solar cell (DSSCs)[2] that utilize solar energy to directly oxidize (and reduce) water into its elemental constituents.

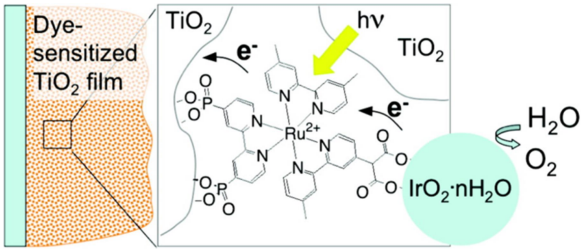

Scheme 1.1. Schematic representation of a WS-DSPEC. Reproduced from ref 3.

Scheme 1.1 shows a cartoon representation of the anode of a WS-DSPEC.[3] A transparent conducting oxide (TCO)-coated glass electrode is coated with a mesoporous metal oxide film and then sensitized with a molecular absorber and a water splitting catalyst. The absorber is excited by visible light and injects an electron into the TiO_2. The resulting hole on the dye travels across the surface via intermolecular hopping between dye molecules until it finds a catalytic site, which then collects the holes to oxidize water generating protons and molecular oxygen. Injected electrons percolate through the mesoporous electrode via a random walk, trapping/detrapping process to the TCO back-contact. Once reaching the TCO, the electrons move out through an external circuit to a dark cathode where the electrons are used to reduce protons to molecular hydrogen. Within the context of a single absorber driving both water oxidation and reduction, the components are modular and can be readily substituted provided that 1) the dye has an excited state potential sufficiently negative to inject into the metal oxide, and 2) the dye has sufficiently positive ground state potential to oxidize the water oxidation catalyst. Use of a high surface area support also relaxes the catalytic turnover requirements needed for the catalyst to keep up with solar flux. The modular nature of WS-DSPECs has resulted in a wide variety of semiconductors, absorbers and catalysts being employed. In order for water splitting to occur in such a system without any input of electrical power,

there is a third requirement that the conduction band (CB) edge potential of the semiconductor be negative of the hydrogen/water formal potential. The most commonly used oxide semiconductors in WS-DSPECs, TiO_2 (due to trapping pulling the Fermi energy below the CBM) and SnO_2, do not meet this requirement, and thus an added bias voltage – typically on the order of 200-300 mV - or a second light absorber at the cathode is needed for overall water splitting to occur.

The minimum thermodynamic potential for water splitting is 1.23 V. This corresponds to a photon with a wavelength of roughly 1100 nm. A WS-DSPEC, however, typically employs dyes with moderately large HOMO-LUMO gaps (2-3 eV) due to losses associated with each electron transfer needed to drive directional electron flow, as well as a significant kinetic overpotential (350-500 mV) associated with the water oxidation catalyst.

Despite its important role in relaxing requirements on the molar absorptivity and catalytic turnover frequency, the high surface area of the oxide semiconducor film can introduce complications in electron transport through the film as well as proton management, as will be discussed later. These issues cause the overall power conversion efficiency of these devices to remain low, despite extensive research efforts. In the following sections, we discuss current research focused on metal oxides for WS-DSPECs, specifically focusing on the parameters affecting interfacial electron transfer and transport. Additionally, we review current research on dye binding groups and their impact both on dye stability for long-term device operation and their ability to facilitate charge transfer to the metal oxide support. Water oxidation catalysts have been reviewed in detail elsewhere, and we refer interested readers to several recent reviews.[4–8]

1.2 Mesoporous Support

In a dye-sensitized solar cell (DSSC), the metal oxide must meet certain criteria. The material should be able to be prepared as a nanoparticulate, mesoporous high surface area support to facilitate light absorption via high dye loading. Furthermore, the film should be transparent to visible light with minimal scattering for efficient light harvesting. The material should have a conduction band minimum (CBM) sufficiently below the excited

state of the dye to introduce a high driving force for injection, while maintaining a high charge mobility to move the electrons away from the oxidized dye molecules. It should also be electrochemically inert to the electrolyte used.

When moving from DSSCs to WS-DSPECs, some of those criteria become much more limiting, such as stability against the solvent/electrolyte. The electrode material used must be stable in aqueous solution. Additionally, in the case where one photon is used to drive both the water oxidation and reduction reactions, the CBM must also lie sufficiently above the H^+/H_2 couple to drive proton reduction at the cathode. In the following section, we will explore the intrinsic parameters of several possible metal oxide support structures that impacts device performance.

1.2.1 Titanium Dioxide. Anatase TiO_2 is ubiquitous in the field of dye-sensitized solar cells DSSCs and WS-DSPECs. Anatase has a well-positioned CBM that maximizes the photovoltage generated by the devices while still permitting a high driving force for charge injection. Additionally, it has a sufficiently high charge mobility to facilitate the separation of injected electrons and holes at the surface. The similarities between DSSCs and WS-DSPECs make anatase TiO_2 a good candidate for a support in the latter system as well; the CBM lies above the proton reduction couple yet is sufficiently far below the excited state potential of the dye to promote injection from it (below pH ~7). TiO_2 is also stable in acid, basic, and neutral aqueous solutions, making in an excellent support for the WS-DSPEC.

1.2.1.1 Electron Injection into TiO_2. In order to facilitate rapid charge injection, the metal oxide needs a high density of acceptor states at an energy level close to the energy of electrons in the excited state of the dye molecule.[9–14] Injection into TiO_2 is generally found to be kinetically multiphasic, as a result of the complex manifold of excited states for the most commonly used dyes.[15–21]

The injection processes for ruthenium(II) polypyridyl dyes are shown in Figure 1.1.[20] Upon light absorption, the dye is excited into a singlet metal-to-ligand charge transfer state (^{1}MLCT). Injection from this high energy, short-lived state results in the fast ("hot") injection component.[19,20,22] Intersystem crossing to the lower energy triplet state

(^{3}MLCT) rapidly occurs (on the 100 fs time scale for $[Ru(bpy)_3]^{2+}$).[23] Injection can also occur from this state, but at the lower energy state and a lower density of acceptor sites, this injection process is slower than from the singlet. This is a relatively long-lived state since the decay to ground state is spin forbidden, so some injection intensity is derived from the triplet MLCT state despite the fact that it is a slower process.

Injection from porphyrin derivatives is slightly more complicated.[24–26] Excitation of the porphyrin Soret band (or B band) populates a short-lived, high-energy singlet, S_2, state that decays to a lower energy singlet, S_1, on the femtosecond timescale. The S_1 state can also be accessed directly by excitation of the Q-bands. If the central atom of the porphyrin is a heavy metal cation (e.g., Pd, Pt) intersystem crossing from the S_1 into a triplet state also occurs rapidly. All or some of these states can be accessible for injection depending on the porphyrin substituent and central cation.

In TiO_2, the CB is comprised primarily of empty Ti^{4+} 3d orbitals and has a high density of states (DOS).[11,27] This is the primary reason for the rapid electron injection dynamics in TiO_2, with most of the injection occurring within the first few hundred femtoseconds in organic solvents.[10,19,28–30] The requirement for good orbital overlap between the excited state of the dye and the CB of the metal oxide was demonstrated recently by several groups with the incorporation of an alkyl group between the chromophore and the anchoring group, thereby disrupting the conjugation to the anchoring group and, consequently, the metal oxide which resulted in reduced injection yields.[31–33] This phenomenon is discussed in more detail in Section 1.3.2.

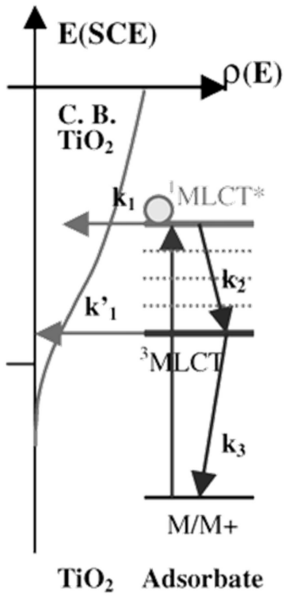

Figure 1.1. Possible electron transfer pathways in common ruthenium(II) polypyridyl dyes. Excitation occurs via visible light absorption to the singlet state (^{1}MLCT), from which the electron can be injected in to the CB (where there is a higher density of acceptor states) of TiO_2 (k_1) or through intersystem crossing can relax (k_2) to a manifold of triplet states (^{3}MLCT). The triplet state can also inject into TiO_2 (k'_1), although there is a lower density acceptor states at that energy. The triplet can also relax back to ground state (k_3). Reproduced from ref 20.

Electron trap states in TiO_2 can also act as acceptors for change injection. This has been demonstrated by Asbury, et al. who observed that under a negative bias (filling empty traps in the TiO_2), the total injection rate slows down.[20] They observed a decrease in the overall injection yield as well as an increase in the ratio of the slow component to the fast component. A similar effect occurs when the pH is changed. Upon increasing the pH of solution, the CBM of a metal oxide shifts to more negative potentials by approximately 59 mV/pH unit. By increasing the pH, the driving force for injection correspondingly decreases since the dye potentials do not change significantly with pH. Because the ^{1}MLCT state is so short lived, small changes in the driving force can result in much of injection yield originating from the ^{3}MLCT state. Qualitatively, work from Swierk et al. in aqueous buffers demonstrates the same effect of pH on injection yields.[21] In these systems the injection kinetics were triexponential and each kinetic component

slower at higher pH. The overall injection yield decreased when the slower kinetic components became the more dominant injection pathway.

Injection dynamics have also been found to be sensitive to the surrounding local environment, where elevated (small radius) cation or proton concentration results in more rapid injection dynamics. Tachibana et al. demonstrated that injection was much slower in pure acetonitrile than in acetonitrile solutions that contained 0.1 M Li^+.[34] This result was consistent with observations that elevated cation or proton concentrations in solution lowered the quantum yield of fluorescence for dyes tethered to the surface.[30,35] This appears to be similar to the effect of Li^+ concentration in DSSCs, where the Li^+ serves to lower the photovoltage of the device. In both cases, the cation decreases the Fermi energy in the metal oxide and thus facilitates charge injection by increasing the density of available acceptor states.[36,37] Similarly, we have recently shown that proton intercalation in WS-DSPECs can result in the creation of surface trap states. These proton-stabilized trap states can actually act directly as acceptor states for injection, trapping the electron for a long enough time to result in recombination (Chapter 3).[38]

1.2.1.2 Charge Mobility and Recombination in TiO_2. The mechanism by which photoinjected electrons are transported in TiO_2 has been extensively studied. There is general agreement that the electron mobility is trap-limited and can be accurately described by a continuous time random walk (CTRW) model.[39,40] Because any long-range electric field generated within the film would be effectively screened by the high dielectric constant of the TiO_2 and the interpenetrating ions in solution, electrons follow a random, non-directional walk through the film before either recombining with a dye or exiting the film into the external circuit through the back contact.[41] As a result of the high surface area of the nanoparticle film, TiO_2 has been described as having an exponential distribution of trap states below the CBM, often ascribed to surface defects or oxygen vacancies.[39,42,43] There is also evidence in rutile TiO_2 that electrons can "self-trap" when interacting with a Ti^{4+} lattice site, creating their own potential well in forming a Ti^{3+} site in the lattice.[44] This is because the CB is comprised primarily of nominally localized, empty Ti^{4+} 3d orbitals. As a result, mobility can be described in one of two different processes: 1) CTRW driven by thermal detrapping of electrons into the mobile

conduction band, motion, and retrapping; or 2) electron hopping/tunneling to nearby trap states.

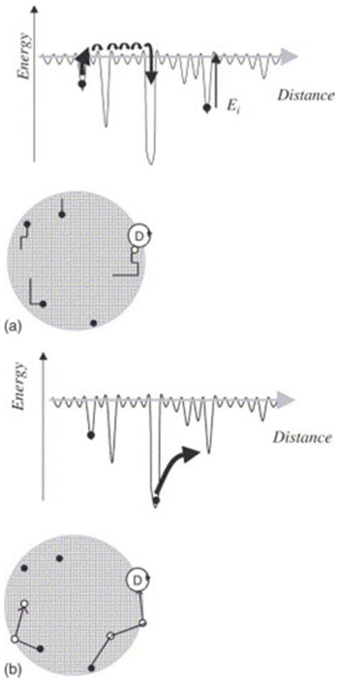

Figure 1.2. Transport models for electrons in TiO_2. (a) continuous-time random walk model in which electrons thermally detrap to the CB and fall into a neighboring trap in a non-directional motion. (b) Electrons tunnelling from one trap to a neighboring empty trap. Reproduced from ref 40.

Charge diffusion throughout the entirety of the film is comprised of both intraparticle and interparticle motion where the net diffusion can be limited by the intraparticle motion within each particle or by electron transfer between adjacent particles. Therefore, to an extent, the processes in which each are understood can be decoupled.

Nelson et al. modeled these processes and compared them to bulk recombination rates with oxidized dye molecules following charge injection.[39] Because charge motion in this system is not directional, the charge diffusion and recombination rates are intimately related.[39,41] This makes the recombination rate a comparative metric for determining the rate of charge diffusion in this system. A schematic representation of the two proposed charge diffusion processes is shown in Figure 1.2.[40] In Figure 1.2a, the electron executes a CTRW, moving randomly through the particle through a process of thermal

detrapping/retrapping. In this model the time an electron spends in a trap (and therefore the relative charge diffusion) is determined only by the depth of the potential trapping the electron. The process ends with eventual recombination with the oxidized dye molecule on the surface of the nanoparticle. In the trap hopping model (Figure 1.2b), the trapped electron experiences a small attractive force from either empty trap sites or the oxidized dye and will periodically tunnel from one trap site to another, again ending when the electron finds the oxidized dye. In this model, the charge diffusion rate is directly related to the distance between traps and is not entirely related to trap depth. The authors conclude that the CTRW model agrees well with experimental findings, which is consistent with the electron randomly walking through a material while being shielded from any directional pull.

Conceptually, this trapping/detrapping model is consistent with observations that the rate of recombination (and presumably the electron mobility) is sensitive to the electron density in/near the TiO_2 CB. This has been conclusively demonstrated in WS-DSPECs by our group as well as by others. Using open circuit photovoltage decay, we observed a strong dependence of the rate of recombination on the photovoltage, which corresponds to an increase in the Fermi energy of the TiO_2 that results from increased trap occupancy.[45] This results in a shorter trapping time as the filling of deeper traps, increasing the charge mobility and, as a result, the recombination rate. This has also been demonstrated elsewhere using optical pump/probe spectroscopy coupled with the use of an external bias.[46,47] By applying an increasingly negative bias and slowly filling trap states in the TiO_2, it was shown that the recombination rate could increase by as much as 6 orders of magnitude when the bias applied approached the working conditions of a conventional DSSC.

Further complicating the trapping dynamics, both recombination and charge mobility have been shown to be sensitive to species in solution. As the trap states are largely attributed to surface sites, the adsorption/coordination of ions in solution is expected to influence the nature of the traps. This has been observed in DSSC literature, where the Li^+ intercalation from solution results in a lowering of the overall photovoltage as a result of the formation of localized trap states.[48] Recently, we found with WS-DSPEC electrodes that proton intercalation can induce trap states in TiO_2 during exposure to

acidic solutions. This is consistent with earlier observations that proton intercalation can cause trap states in metal oxides (Chapter 3).[38,49–52] Although the nature of these trap states is not well understood, studies of reduced anatase nanoparticles suggest that the protons serve to stabilize a surface-disrupted TiO_2 lattice and the disordered lattice results in the formation of additional surface trap states.[53,54] These energetically shallow, electrostatically stabilized trap states can persist for up to milliseconds, compared to the one to tens of nanoseconds expected for a typical TiO_2 trap state in the absence of proton stabilization.[49] The lifetime of proton-stabilized trap states is sufficiently long to facilitate charge recombination with oxidized dyes on the surface.

Interparticle electron transfer is slow relative to intraparticle transport and decreases the effective charge mobility by about one order of magnitude.[55,56] Kroeze et al. used low intensity illumination to saturate trap states before measuring the recombination dynamics and found a maximum intraparticle diffusion coefficient of 10^{-3} cm^2/s, but they measured a bulk diffusion coefficient of $10^{-4}cm^2/s$.[56] Two physical factors that affect charge mobility are the film geometry and the nanoparticle connectivity. The disordered three-dimensional connectivity of TiO_2 nanoparticles strongly affects charge transport through the film to the back contact.[57] This effect has been observed in other disordered media, specifically in porous Si films.[58] Instead of follwing a direct path to the back contact and external circuit, in the nanoparticulate films the electron travels a tortuous path through film. Transport is further complicated by the random movement of electrons; in order for an electron to transit the film, it must randomly walk its way in the direction of the back contact through disordered aggregates of nanoparticles.

Modeling of the connectivity of the nanoparticles in the film indicates a direct effect on the rate charge diffusion across the boundary.[55] This is not unexpected as the size of the neck between particles directly corresponds to particle overlap, which increases the probability that the electron will find a trap nearby in a neighboring particle. Figure 1.3 shows a schematic representation of this phenomenon, where the size of the neck was measured by the angle that a single nanoparticle makes with its conjoining neighbor.[55] The authors found that the necking angle could change the probability of the electron transfer from one particle to another by as much as a factor of 2.

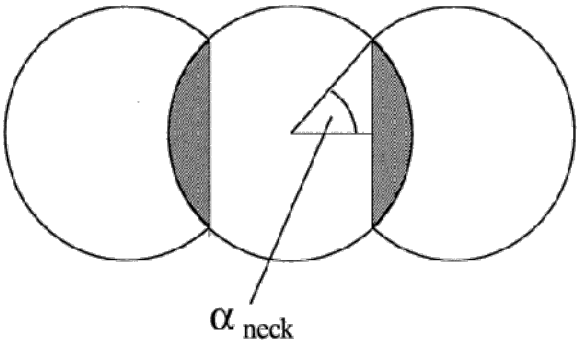

Figure 1.3. Schematic representation of the degree of necking of nanoparticles, defined by the angle, α, that a particle makes when connecting to a neighboring particle. Grey shaded area shows the space in which an electron can move from one particle to the next. Reproduced from ref 55.

Němek et al. discussed the mean free path of an electron within the TiO_2 of a DSSC based on the measured lifetime and found that the mean free path is considerably less than the size of the nanoparticle, roughly only a few nanometers.[59,60] Once the electron finds the boundary between particles, there is also a greater than 90% probability that the electron is reflected back into the nanoparticle from which it originated. This is due to an energetic barrier between the nanoparticles, where the boundary between particles acts to map out a well within the nanoparticle.[60] As a result, the electron diffusion coefficient in mesoporous films is significantly lower than in bulk, single crystals.[49,60] Improving particle overlap is a possible route towards improving transport, however care must be taken as increased particle overlap comes at the cost of lower surface area.

1.2.2 Tin Oxide. SnO_2 has recently generated interest in its use as a metal oxide in DSSCs and WS-DSPECs.[24] SnO_2 has charge transport dynamics that are much faster than TiO_2, in some cases roughly two orders of magnitude greater.[14,61–64] The relative band positions are shown in Figure 1.4.[65]

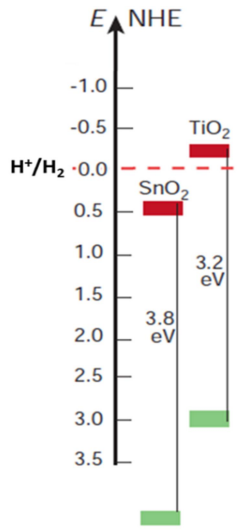

Figure 1.4. Relative energy levels for the conduction and valence bands of TiO_2 and SnO_2. Adapted from ref 65.

As shown in Figure 1.4, the CBM of SnO_2 is several hundred millivolts positive of that of TiO_2.[21,64,65] In the case of a conventional DSSC, this results in a lower overall photovoltage generated by the cell, as the Fermi energy for SnO_2 is lower than that of anatase TiO_2.[66–68] In the case of WS-DSPECs, however, a lower-energy CBM allows enables the use of dyes with a more positive excited state redox potential. This increases the pool of dye choices while additionally allowing for utilization of much more of the solar spectrum than just the blue region. Additionally, the band gap of SnO_2 (3.8 eV) is significantly larger than that of TiO_2 (3.2 eV). These bandgaps correspond to maximum wavelengths of roughly 320 and 390 nm, respectively. As a result, SnO_2 is considerably less likely to absorb solar radiation and generate a hole in the VB. In TiO_2, this highly oxidizing hole can be problematic, leading to ligand oxidation and subsequent loss of active dyes from the surface.[14] In principle, SnO_2 should be a much more stable surface for metal-organic dyes.

In WS-DSPECs, SnO_2 cannot be used for unassisted, single-photon water splitting because the CBM is well below the potential of the H^+/H_2 couple.[65] Despite this drawback, SnO_2 can serve as an interesting metal oxide support for a 2-photon-per-electron water splitting reaction, similar to the natural Z-scheme of photosynthesis. By coupling the SnO_2 photoanode with a photocathode, the overall water-splitting reaction

can be driven by one photon per electron in each half reaction. This in turn limits the requirements of band edge potentials of the metal oxide support.

1.2.2.1 Electron Injection into SnO_2. As Figure 1.4 shows, the driving force for charge injection into SnO_2 is several hundred millivolts greater than for TiO_2, as the CBM of SnO_2 is several hundred millivolts positive of that of TiO_2. However, as noted above, the coupling between the dye excited state and the acceptor states within the metal oxide can have a large impact on the overall injection dynamics.

The CB of SnO_2 is comprised largely of empty s and p orbitals from Sn^{4+}.[12] Typically, bands comprised of s and p orbitals are broader than those made up of d orbitals (as in TiO_2), which results in the s and p bands having lower density of states than the conduction band of TiO_2.[12] Injection into SnO_2 has also been shown to be multiphasic, and the various components of the injection are generally attributed to the same states as they are for TiO_2, with the fast component coming via hot injection from the singlet, ^{1}MLCT, and the slower component coming from the thermalized triplet, ^{3}MLCT.[10,14,21,69] Near the energy of the singlet state, the DOS of TiO_2 is roughly two orders of magnitude higher than of SnO_2.[12] This supports the observed injection dynamics, where the injection yield from the singlet state (the fast component) is generally much less for SnO_2, despite the higher driving force.[12,21,69] Interestingly, however, the triplet state lies close to the CBM of TiO_2 (depending on the local environment), such that the DOS appears to be similar for the two metal oxides, and thus injection occurs at similar rates.[21,69] Additionally the overall injection yield for the two metal oxides has been shown to be very similar within the first nanosecond, despite being more rapid in TiO_2.[21]

1.2.2.2 Charge Mobility and Recombination in SnO_2. In WS-DSPECs, electron-hole recombination between the CB (or traps) of the metal oxide and the oxidized dye represents the fate of as many as 98% of photogenerated electrons.[45] Therefore physically separating the electron and hole in space, as well as rapidly regenerating the dye, are two requirements for a functioning device. In DSSCs, dye regeneration occurs very rapidly (in nanoseconds) by electron transfer from the redox couple in solution. In WS-DSPECs, water oxidation is much slower and dye regeneration occurs on the millisecond timescale.

As a result, metal oxides with high charge mobility are an attractive option for moving the photoinjected electron away from the oxidized dye molecules on the surface.

SnO_2 has been shown to have a charge mobility that is nearly two orders of magnitude faster than that of TiO_2.[61,64] The CB features an exponential tail of trap states below the CBM,[70] however the density of those trap states is low relative to trap states in TiO_2. Furthermore, the dark resting potential for SnO_2 lies just below the CB so that electrons are injected into relatively shallow trap states, which allows for those electrons to be more easily excited thermally into the CB.[64] This has been shown in experiments similarly to those done with TiO_2, in which a steadily increasing potentiostatic bias that increased the occupancy of trap states resulted in a higher recombination rate.[71] As with to TiO_2, the charge mobility in SnO_2 electrodes is also intimately related to the rate of recombination.[64,71] As a result, the recombination dynamics between electrons injected into SnO_2 and the oxidized dye on the surface has been shown to be approximately one to two orders of magnitude faster than with TiO_2. Because recombination is already the major kinetic pathway with TiO_2 electrodes, this increase in recombination rate makes simple SnO_2 electrodes to be poor candidates for use WS-DSPECs.

Some research is being done, however, to treat the surface of these electrodes with thin films of other metal oxides in order to impede recombination. The concept of using core/shell electrodes has been widely studied for DSSC applications and is now increasingly used to improve the kinetics of electron transfer in WS-DSPECs.

1.2.3 Core/Shell Structures. A variety core/shell structures have been studied for applications in DSSC[72] and WS-DSPEC electrodes.[21,73–75] These structures can be used to control the recombination rate or to improve the stability of the sensitizer on the surface of the core material, with both strategies demonstrating some success. The two commonly utilized designs for core/shell electrodes are shown in Figure 1.5. On the left side of Figure 1.5, a cascade electron transfer is shown, in which the shell CB falls between the excited state of the dye and CB of the core. In this case, the electron is initially injected into the shell material before falling into the core. From this point, the electron must tunnel through the shell material to recombine with the dye. In the other design, shown on the right in Figure 1.5, a core material is coated with a wide band gap

material with a CBM well above the excited state potential of the dye. For this structure, electron injection occurs by tunneling through the shell material directly into the core. As in the first case, recombination must occur via tunneling through the shell material.

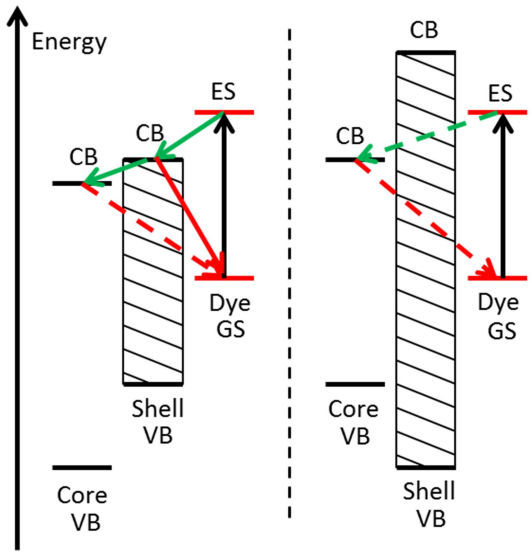

Figure 1.5. Common designs for core/shell structures in DSSCs and WS-DSPECs. (left) Charge injection occurs from the excited state (ES) of the dye into the conduction band (CB) of the shell and electrons subsequently fall into the CB of the core material. Charge recombination with the dye can occur directly from the shell or by tunneling through the shell from the core. (right) Charge injection occurs by tunneling through the shell directly into the core. Recombination also occurs via tunneling through the shell material.

The utilization of core/shell structures for WS-DSPECs began by using a rough solution phase process to deposit a wide band gap semiconductor (ZrO_2, Nb_2O_5) surface film on metal oxide electrodes in order to control back electron transfer (Figure 1.5, right).[73] Because injection occurs many orders of magnitude faster than the relaxation of the dye, sacrificing some driving force for injection by adding a tunneling barrier is not immediately detrimental to the device performance. However, this tunneling barrier has a more significant effect on the recombination pathway, as the electron must tunnel through an even higher barrier in order to recombine with the oxidized dye molecule. The method showed some success but as the authors pointed out, the film was not uniform and the

shell was incomplete.[73] This would allow for recombination sites where voids in the shell material exist, which could be accessible to holes via charge transfer diffusion between dye molecules.

In addition to providing a uniform coating, the deposition process should also allow for very fine control over film thickness. The rate of tunneling decays exponentially with distance[76] and, as such, the film thickness is very important for minimizing recombination without also blocking charge injection.[73,76,77] To address this concern, several studies (detailed below) have moved from solution phase to vapor phase deposition, specifically atomic layer deposition (ALD). ALD works by exposing a heated surface to alternating pulses of an organometallic metal oxide precursor and water vapor in a self-limiting sequence; when the surface is saturated with precursor, deposition stops until the surface-bound precursor is hydrolyzed with a water pulse. This process deposits completely conformal films while allowing for a thickness resolution of a single atomic layer.

Recently, Meyer and coworkers demonstrated a large improvement in device stability and performance when compared to a simple SnO_2 film by using a SnO_2/TiO_2 core/shell structure.[78,79] Rather than requiring that an electron tunnel through the shell layer to reach the core, this alignment permits injection into a thin TiO_2 shell before moving into the SnO_2 core (Figure 1.5, left). Once in the core, the electron must tunnel through the TiO_2 barrier to recombine with an oxidized dye molecule. In studying the injection dynamics of these structures, we recently showed that the electron is injected into the TiO_2 film and is trapped before eventually being released to the SnO_2 core (Chapter 4). This demonstrates the importance of thickness control; if the film is too thick and the electron becomes trapped in the TiO_2, recombination could easily proceed as it would in a simple TiO_2 electrode.[80] With a film that is too thin, recombination would remain a facile pathway in the high charge mobility SnO_2.

A core/shell structure also offers the possibility for improved dye binding and stability. Many studies have explored the stability of anchoring groups on metal oxides, and the commonly used phoshonate group is much more stable with respect to hydrolysis on ZrO_2 than it is on TiO_2.[81] Meyer and coworkers have also recently explored a different stabilizing mechanism, a “mummy” strategy in which the core metal oxide is sensitized

with dye and then ALD is used to create an overlayer of Al_2O_3 that then protects the surface of the dye from hydrolysis.[74,75,82] The authors found that the dye desorption rate decreased by nearly an order of magnitude; however, as the layer thickness increased, the hole transport across the surface via hopping between dye molecules slowed down dramatically.[75] They also noted a lower injection yield, though a later study by Swierk et al. suggests that the injection yield is similar, with a larger contribution from the ultrafast component.[21] Despite showing improvements in stability, the "mummy" strategy does not seem to have a major impact on the rate of recombination, which is clearly the limiting factor in SnO_2-based devices.[75]

1.3 Dye Anchoring Group

In order to address concerns related to injection efficiency and dye stability on the surface of a metal oxide, various different linker groups have been examined for dyes in WS-DSPECs. Primarily, phosphonate has been used due to its much higher stability on TiO_2 in aqueous environments relative to carboxylate.[83–87] More recently, various other groups have been tested for their stability in basic solution as well as for injection dynamics through the ligand. These include catechol, acetylacetonate (acac), and hydroxamate. Figure 1.6 shows the structures of these ligands.

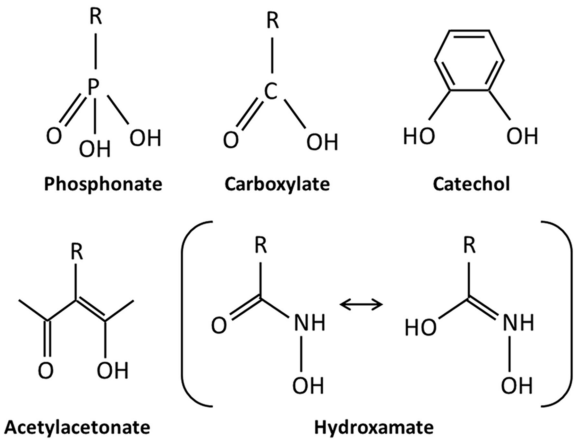

Figure 1.6. Structures of commonly examined linker groups for WS-DSPECs. Hydroxamate is shown as both conformers as DFT calculations have suggested that they are nearly equal in energy. Reproduced from ref 88.

In this section, we will discuss the decision of linker choice and the impact the selection has on device performance, specifically stability for long term applications and the ability of the linker group to facilitate charge injection.

1.3.1 Stability on the Surface. The strength of the bond between the metal oxide surface and the linker ligand determines the long-term stability of these electrodes. In order to improve long-term operation of these devices, the linker group must be carefully considered to allow for a strong interaction between the linker and support.

1.3.1.1 Carboxylate and Phosphonate. In order for WS-DSPECs to be useful for practical applications, the electrodes must be stable for long periods of time. Through three decades of DSSC research, the field has heavily relied on dyes anchored by a carboxylate group.[89,90] Because DSSCs use a non-aqueous electrolyte solution, this is generally not a problem. However, even in long-term applications of DSSCs, depending on the solvent selected, water can be slowly is taken up by the solution and can eventually cause desorption of the dye by hydrolysis of the carboxyate-metal oxide linkage.[89] In order to address this problem, phosphonate anchors are the overwhelming choice for water-sensitive applications. It has been well established that phosphonate groups bind more strongly to metal oxides than carboxylates.[83–87] This is commonly attributed to a higher affinity of the phosphonate ligand to the metal oxide surface as well as the ability of the phosphonate group to be either bi- or tridentate, increasing the stability of the anchor on the surface.[83,87] In fact, it has even been shown that the affinity of phosphonate for TiO_2 is so strong that phosphonic acids can cleave the O-Ti-O bond and solubilize Ti.[84]

Much effort has been dedicated to determining the aqueous stability of phosphonate groups relative to carboxylate.[83,87,91–96] Early work demonstrated that carboxyalkylphosphonic acids form self-assembled monolayers (SAMs) on the surface of TiO_2 by preferentially binding at the phosphonic acid group.[96,97] Generally, dye desorption is ascribed to hydrolytic cleavage and is well-known to be pH dependent, with the rate of desorption increasing dramatically at higher pH.[92,95,98] However, this generally occurs in the dark as a direct sensitivity to water or is inferred from steady state UV/Vis

spectra before and after some fixed illumination time.[94,95,99] Recently, Hanson et al. studied the stability of isostructural dyes anchored by either two carboxylate or phosphonate groups on a single 2,2'-bipyridine ligand on TiO_2 and monitored dye anchoring throughout the course of illumination.[93] The stability of the dye was determined by UV/Vis spectroscopy, in which a decline in the absorption peak signaled loss of dye from the surface of the electrode (Figure 1.6). They found that, even without illumination and under acidic conditions, the dye bound by carboxylate rapidly desorbed (8.5×10^{-5} s^{-1}), consistent with other reports,[95,98,100] whereas the dye anchored by phosphonate did not show any measureable desorption, as shown in Figure 1.7a. This is consistent with results obtained by many other groups. Gillaizeau et al. demonstrated that the phosphonated dye formed an adduct with TiO_2 with a binding constant that was nearly an order of magnitude greater than that of carboxylate.[94] Under illumination at pH 1 (Figure 1.7b), the authors observed a biexponential desorption profile, which they attributed to possible competing desorption/decomposition pathways or due to inhomogeneity in the film.

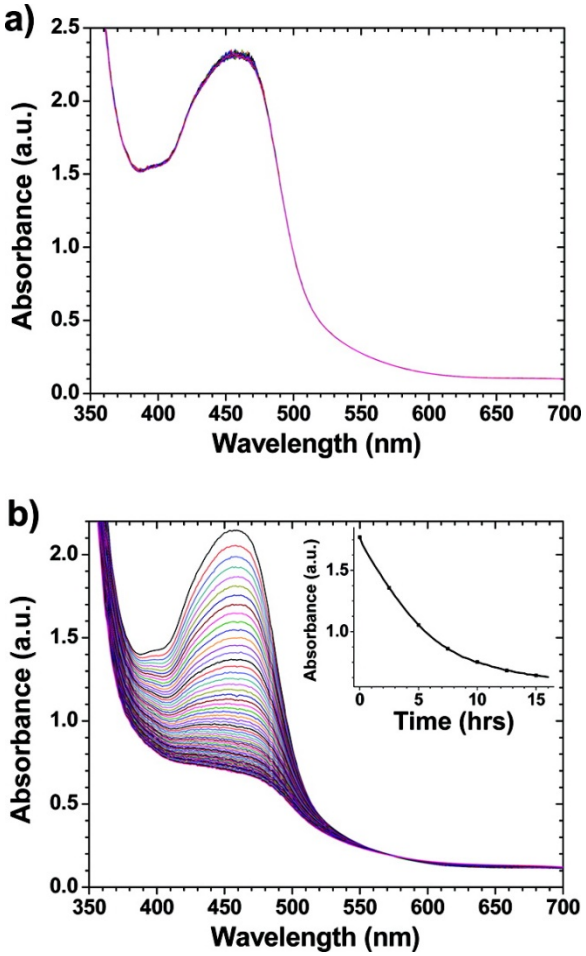

Figure 1.7. Changes in the absorbance of $[Ru(bpy)_2(4,4'\text{-}(PO_3H_2)_2bpy]^{2+}$ on a mesoporous TiO_2 electrode without (a) and with (b) irradiation (475 mW/cm^2 at 455 nm). Inset shows the absorbance change at 480 nm. Reproduced from ref 93.

The weighted rate of photodesorption found for this pathway was 5 x 10^{-5} s^{-1}, still slower than the carboxylated dye in the dark. The authors also note that the rate of dye desorption, regardless of anchoring group used, was sensitive to dissolved oxygen in the electrolyte, noting that under Ar atmosphere the rate of desorption of the phosphonated dye slowed by a factor of 5.

In an effort to eliminate processes related to oxidation of the dye, the authors also studied the stability of the phosphonated dye on a ZrO_2 surface and found that the rate of desorption was roughly one full order of magnitude slower and was still sensitive to oxygen, though less so. It is difficult to tease out which effect resulted in the dramatically increased stability; whether the oxidized dye is more prone to desorption or if the

phosphonate group is much more stable on ZrO_2 compared to TiO_2. It has been shown that phosphonate also has a much higher affinity for and forms stronger bonds with ZrO_2 than TiO_2, however it is not clear to what extent this effect contributes to the slower rate of dye loss from ZrO_2 surfaces.[96]

1.3.1.2 Other Groups. Although phosphonate provides an anchoring ligand with adequate stability to produce a functioning device, the long-term stability of these photoanodes is still poor, especially in weakly acidic or basic solutions. To address the long-term stability concerns, several groups have studied alternative linker groups. The more commonly studied alternative anchoring groups have been catecholate,[97,101–103] acetylacetonate (acac),[32,104] silatranes,[105,106] and hydroxamate.[88,107–109]

Catecholate linkers (see Figure 1.6 for structure) were proposed to be a promising replacement for carboxylate as they form 5-member rings with metal oxide surfaces.[102,110,111] Despite increased resistance to surface hydrolysis, the catecholate linkers resulted in much more rapid electron/hole recombination following charge injection in Mn-based and $Os(bpy)_3$ photochemical systems.[101,103] A similar problem was found for systems using the acac linker (see Figure 1.6 for structure). Despite the fact that TiO_2 sensitized with an acac ligand was less sensitive to desorption under aqueous or oxidative conditions,[104] testing in a regenerative photoelectrochemical cell showed that the acac linker was actually be a less stable than carboxylate under working conditions in a non-aqueous dye cell.[32] The instability was suggested to be due to atmospheric water that was taken up by the solvent used in the DSSC.[89] This suggested that the acac ligand, despite being stable in aqueous solution, may not be especially stable in aqueous media under photoelectrochemical working conditions. More recent work has also examined the ability of silatranes to form stable binding groups on metal oxides. Within the context of DSSCs, these groups were found to perform roughly as well as phosphonates in terms of overall efficiency.[106] Materna et al. recently examined the stability of the silatrane groups in aqueous media and found that they offer improved stability over phosphonate across a wide pH range (2-11) while allowing for reversible redox activity of Ru compounds on the surface.[105] This suggests that silatranes could offer a solution to pH-driven stability issues observed with phosphonate groups.

A different ligand has received growing attention recently as a possible replacement for the common anchoring groups is the hydroxamate group (Figure 1.6 for structure). Folkers et al. studied the stability of self-assembled monolayers tethered to several different oxide surfaces via carboxylate, phosphonate, and hydroxamate and found that hydroxamate was much more stable than carboxylate with respect to hydrolysis.[112] More recently, this work has been supported by others, demonstrating that hydroxamate linkages to metal oxides were dramatically more stable than carboxylate and nearly as stable as phosphonate when exposed to water.[98,109] McNamara and coworkers directly compared the stability of benzyl ligands linked by either hydroxamate or carboxylate after soaking in either water or a mildly basic solution.[109] Within one hour, roughly 70% of the carboxylate ligand had desorbed at neutral pH, and in basic pH more than 90% had desorbed. This is in contrast to the hydroxamate linker which sees no statistically significant desorption at neutral pH and less than 20% in a basic medium over the course of a full 24 hours.

This relationship has been probed using DFT calculations and it has been shown that hydroxamate is 20 – 33% more stable than carboxylate on the surface of TiO_2.[98,109] Reasons for the greater stability of hydroxamate may relate to its dianionic charge or its less strained bite angle (75° vs. 61°). The relative pKas of these linkers could also contribute to the aqueous stability on the surface, with pKas of 8.88, 6.5, and 4.76 for the second hydroxamate proton, the second phosphonate proton, and carboxylate, respectively.[98,102] The less acidic nature of the phosphonate and hydroxamate likely will make them less prone to being hydrolyzed off the surface of TiO_2.

1.3.2 Injection Dynamics Through the Anchoring Group. While the stability of the anchoring group is important for long-term application, the ligand must also facilitate charge injection into the semiconductor from the photoexcited dye. The success of the carboxylate anchor in nonaqueous systems is derived largely from the exceptional injection dynamics through the carboxylate ligand.[88,113] Because of the poor stability of carboxylate on TiO_2 surfaces, WS-DSPEC dyes tend to utilize phosphonate anchors. This comes at the cost of lower injection efficiency in these devices as experiments with DSSCs have shown that electronic coupling through the sigma framework of the

phosphonate group is weaker than it is through the π-coupled carboxylate group.[109,113] Unfortunately, this is a difficult comparison to make directly in WS-DSPECs as studying the injection efficiency of carboxylate-linked dyes in water can be challenging.

A comparison between carboxylate and phosphonate-linked perylene was done on TiO_2 under ultrahigh vacuum conditions in order to rule out any effects on driving force, where the driving force for charge injection from perylene is approximately 800 mV.[97] It was found that the charge injection was roughly twice as fast (13 fs) for the carboxylate than the phosphonate (28 fs). The different rates of charge injection were attributed to the charge density on the LUMO of the chromophore. In the case of the carboxylate ligand, the sp^2 hybridized carbonyl group allows for the delocalized charge density to partially occupy the carboxylate, while the sp^3 hybridized P does not allow for such charge delocalization. In fact, there is roughly an order of magnitude greater partial charge density on the carboxylate ligand in the LUMO.[97] In DSSCs, despite slower injection kinetics in the phosphonate-linked chromophore, both remain much faster than the relaxation pathway and result in a high quantum yield for injection. However, in aqueous media, there is less flexibility in the injection lifetime and, for phosphonate-linked dyes, the injection efficiency falls to ~20% at neutral pH[21,38,45] as a result of slow injection kinetics (likely due both to lower driving force and the phosphonate linker). This effect has been similarly shown using DFT calculations for chromophores with carboxylate, propionate, and acrylate anchoring groups. The injection kinetics were slowest with the fully saturated propionate group compared to the other ligands.[114]

The importance of the electronic overlap between the anchoring ligand and the support is further supported by earlier work by Heimer et al.[32] In an attempt to understand the capability of an acac ligand to act as a chromophore anchor, they synthesized dyes that had a carboxylate, an acac, or a propylcarboxylate anchor that mimicked the propyl group separating the binding site from the dye in the acac ligand. They found that acac- and propylcarboxylate-linked dyes had similar injection kinetics, which were both much slower than the simple carboxylate-linked dye. The recombination rate was also about one order of magnitude slower for the acac and propylcarboxylate dyes. Warnen et al. attributed the low injection efficiency of the acac ligand to the orientation of the ligand with respect to the pyridyl rings.[33] The acac linker orients perpendicularly to the ring

system, breaking the π conjugation and limiting charge density on the anchoring group. They suggested that incorporating degrees of unsaturation into the linker to enforce a planar orientation could improve the injection rate through this ligand. These differences further show the importance of electronically coupling the anchoring group to the metal oxide support in order to drive efficient charge injection.

The nature of catechol binding to TiO_2 is unique; the ligand is capable of forming a stable 5-membered ring with Ti.[102,110,111] Due to the relative energies of the catechol and Ti d orbitals, the binding of catechol to the surface also creates a new optical transition in the visible-near UV region.[97,115–117] This optical transition has been ascribed to an excitation directly from the HOMO of the molecule to unoccupied orbitals localized on the TiO_2 lattice. The benefit of this charge-transfer pathway involves placing an electron directly on the TiO_2 without spending additional energy to drive charge injection. Charge injection/transfer has been shown to occur in less than 100 fs.[102] However, the coupling of the orbitals that results in excitation transfer of the electron also promotes charge recombination or, more accurately, simple relaxation in the case of the catechol system. This has been demonstrated in a system using an $Os(bpy)_3$ derivative, where the dye was bound to the TiO_2 surface using a catechol linker on one of the 2,2'-bipyridine ligands.[103] The authors observed lifetimes for the electrons in TiO_2 ranging from hundreds of picoseconds to nanoseconds, i.e., charge recombination that was 7 orders of magnitude faster than the hundreds of microseconds to milliseconds measured for phosphonated ruthenium(II) polypyridyl derivatives.

Perhaps the most promising ligand being currently studied is the hydroxamate anchoring group, which not only forms a strong bond with the TiO_2 surface in aqueous solutions, but also has injection kinetics that are in most cases faster than those obtained with carboxylate analogues.[107,109,118] Consistent with other findings, Negre et al. have shown that the injection efficiency has a linear relationship with the calculated single molecule conductance of the anchoring ligand.[88] By using different pyridyl-linker ligands, namely carboxylic acid, phosphonic acid, hydroxamic acid, acetylacetonate, and boronic acid, on TiO_2, a high-potential porphyrin, $ZnPF_{10}$-diester, could be bound to the TiO_2 surface through a pendent pyridyl group in the axial position. This linkage is shown

in Figure 1.8. This allowed the authors to directly compare results with different anchoring groups.

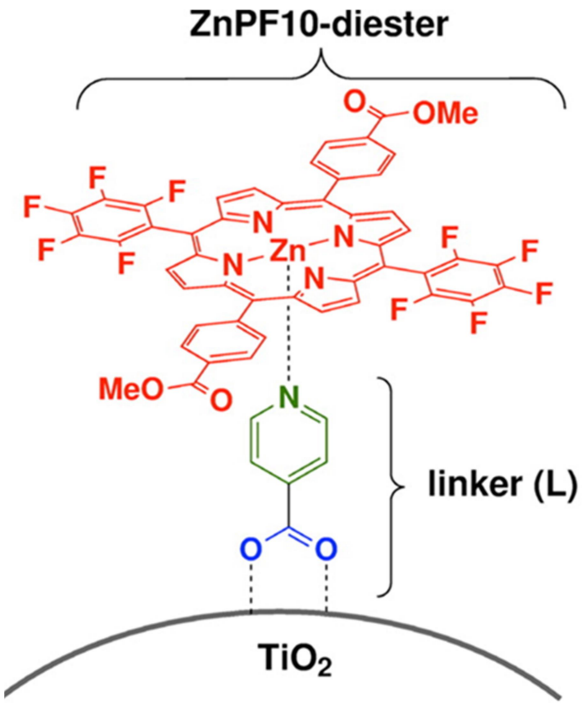

Figure 1.8. Schematic representation of the $ZnPF_{10}$-diester dye bound to the surface of TiO_2 through various linkers. Reproduced from ref 88.

By using this design, the authors were able to synthesize a single chromophore to study injection through multiple linker units. This kept the energetics of injection constant while modulating the coupling between the dye and metal oxide. They were able to directly isolate the ability of the linker to facilitate charge injection into the TiO_2 from the porphyrin dye. Injection yields in this system had a direct correlation with the calculated conductance of the free linker molecule, which further supports the need to focus on delocalized structures that maintain partial charge density on the ligand following excitation. Interestingly, hydroxamate showed an improvement in injection yield over carboxylate by nearly as much as carboxylate improved the yield relative to phosphonate. Coupled with a moderate stability in water, hydroxamate anchoring groups show great promise moving forward as binding ligands for various chromophores on the TiO_2 surface.

1.4 Conclusion

WS-DSPECs provide a possible route to water splitting using solar irradiation. The modular nature of these devices allows for components to be studied and optimized on an individual basis using model systems. As a result, understanding the components that contribute most significantly to the performance of these devices is paramount in directing research forward for each component.

In this review, we have discussed specific details related to charge injection, recombination, charge mobility, and dye stability. The modular nature of the system is hindered by the interplay between all of these components; altering one component can have a direct impact on another; for example, changing the metal oxide support directly impacts each of the above parameters. This supports the need to understand which intrinsic properties about each part of the system contribute most directly to the important parameters in order to guide future research.

In the following chapters, we explicitly measure injection dynamics for various metal oxide supports and detail how trapping in the metal oxide can influence injection and recombination rates as well as overall device performance. Additionally, we have demonstrated that protons, which are produced in stoichiometric quantities as water is oxidized at the surface of the metal oxide, can have dramatic effects on all of the important steps in driving water oxidation.

Chapter 2

Ultrafast Electron Injection Dynamics of Photoanodes for Water-Splitting Dye-Sensitized Photoelectrochemical Cells

John R. Swierk,[†,1] Nicholas S. McCool,[†,2] Coleen T. Nemes,[1] Thomas E. Mallouk,[2-4] Charles A. Schmuttenmaer[1]

[†]equal contribution authorship

[1] Department of Chemistry and Energy Sciences Institute, Yale University, 225 Prospect Street, P.O. Box 208107, New Haven, Connecticut 06520-8107, United States

[2]Department of Chemistry, [3]Department of Biochemistry and Molecular Biology, and [4]Department of Physics, The Pennsylvania State University, University Park, Pennsylvania 16802, United States

J. Phys. Chem. C., **2016**, *120* (11), pp 5940-5948.

2.1 Introduction

In the search for a renewable energy alternative to fossil fuels, solar energy is perhaps the most promising alternative. Despite significant solar irradiance (~120,000 TW impinging on the Earth),[119] capturing and storing this abundant solar energy remains a significant challenge. Natural photosynthesis suggests a possible solution to this challenge: utilize a series of ultrafast electron transfers between spatially separated components to harvest light, convert it to useful potential energy, and finally store that potential energy in reduced carbon products.[120] Artificial photosynthetic systems aim to mimic natural photosynthesis by oxidizing water at an anode via:

$$2H_2O \longrightarrow 4H^+ + 4e^- + O_2$$

to generate protons and electrons, which are subsequently reduced at a cathode to produce molecular hydrogen, or in tandem with CO_2 to yield a reduced carbon fuel. Molecular oxygen is also produced at the anode as a byproduct of the water-splitting reaction, and it is this kinetically slow process that often limits overall efficiency in artificial photosynthetic systems.

Characterizing the myriad of electron transfer events that occur in a functioning artificial photosynthetic device is a significant analytical challenge. Events occurring at nanosecond or faster timescales are typically characterized by spectroscopic techniques such as transient absorbance, where changes in visible or near-IR absorbance are observed. Most artificial photosynthetic systems utilize semiconductor components in which electron dynamics can be difficult to probe with traditional transient absorption techniques because of secondary processes such as luminescence. Even still, at best these techniques can only confirm the presence of an electron in the semiconductor without giving information about its state.[10] Unlike visible or near-IR ultrafast techniques, time-resolved terahertz spectroscopy (TRTS) directly probes changes in oxide conductivity related to photoexcitation with sub-picosecond resolution.[25] Mobile electrons injected into the conduction band attenuate the transmitted terahertz radiation (THz); thus, an increase in conductivity upon photoinjection of electrons is observed as a decrease in the

transmitted THz amplitude. This conductivity increase is in turn proportional to the product of the mobility and the carrier density. If the mobility is constant between samples (as when several different dyes on the same metal oxide are compared) then differences in the THz amplitude are directly proportional to carrier density and by extension the relative injection efficiency. When coupled with complementary transient absorption studies, TRTS provides a fuller picture of the electron injection dynamics and offers a powerful tool for understanding electron transfer into semiconductors from the perspective of the semiconductor itself.

Water-splitting dye-sensitized photoelectrochemical cells (WS-DSPECs) draw inspiration from biological systems, utilizing molecular dyes anchored to a high surface area metal oxide support to harvest light.[5] In the most common example, the photoexcited dye injects an electron into the conduction band of a mesoporous TiO_2 film. The electron then percolates through the film to a transparent conducting oxide back contact and is subsequently transported to a dark cathode. On the surface of the TiO_2, a series of fast electron transfers[1,121] bring the hole to a water oxidation catalyst, which subsequently oxidizes water. Despite numerous examples[3,26,73,78,122–132] of WS-DSPECs utilizing a variety of molecular sensitizers and water oxidation catalysts, overall efficiencies remain low under standard one-sun solar irradiance.

A major cause of the low efficiency in WS-DSPECs is the need to balance electron injection against maintaining sufficient overpotential to drive a water oxidation catalyst. Below pH 4, the Ru(III/II) formal potential of the most common ruthenium sensitizer (4,4'-H_2PO_3-bpy)(bpy)$_2$Ru(II) [bpy = 2,2'-bipyridine, 4,4'-H_2PO_3-bpy = 4,4'-diphosphonato-2,2'-bipyridine] (Ru(II)phos) is too cathodic to drive water oxidation. Unfortunately, Ru(III)(bpy)$_3$ sensitizers are also susceptible to nucleophilic attack under basic conditions.[133] Thus WS-DSPECs that utilize Ru(III) polypyridyl sensitizers must operate at or near neutral pH where the injection efficiency of Ru(II)phos is estimated to be a mere 20%.[38,45] Injection efficiencies of porphyrin sensitizers into TiO_2 is estimated to be even poorer.[24,26] Of those injected electrons only a small percentage (1-2%) persist at timescales relevant to solar fuel production.[45]

Although TiO_2 is the best-studied metal oxide semiconductor in WS-DSPECs, others have recently begun to gain attention. Some studies have utilized oxides with more

positive conduction band potentials aiming to enhance injection kinetics, while others have utilized core/shell electrodes in an attempt to maintain efficient injection and retard recombination.[73,78,128,129] While there are reports utilizing ultrafast transient absorbance to monitor the injection dynamics of Ru(II)phos into TiO_2 and SnO_2,[131,134] as well as porphyrin sensitizers relevant to WS-DSPECs,[24,127,128] there are no reports utilizing terahertz spectroscopy. Furthermore, there is as yet little understanding of the dynamics of electrons after their injection into TiO_2 and core/shell structures that are relevant to WS-DSPECs. In addition, preparation and experimental conditions vary greatly among these studies, making direct comparison difficult. In this study, we explore the injection dynamics of Ru(II)phos on several common photoanode designs for WS-DSPECs utilizing TRTS.[135] To ensure maximum comparability, all of the mesoporous films are sensitized and measured under identical conditions. TRTS provides new insight into the trapping of photoinjected electrons in WS-DSPECs, which adds to the mechanistic understanding gained from other transient spectroscopic and electrochemical techniques.

2.2 Experimental Section

All reagents were purchased from Sigma Aldrich or Alfa Aesar and used as received. Bis(2,2'-bipyridine)(4,4'-diphosphonato-2,2'-bipyridine)ruthenium(II) bromide was prepared as previously described.[94]

2.2.1 Sample Preparation. TiO_2 (< 25 nm) and SnO_2 (22-43 nm) nanoparticles were prepared as a paste for doctor-blading following the method of Ito et al.[136] Briefly, the nanoparticles were successively ground with acetic acid, water, and ethanol and then ultrasonicated for 4 min. at a 70% duty cycle using an ultrasonic horn. α-terpineol and ethyl cellulose were added with additional ultrasonication after each addition. Excess ethanol was removed on a rotary evaporator to produce a paste. The films were prepared by doctor-blading on fused quartz substrates (GM Associates) using Scotch tape as a spacer layer. After each layer the sample was heated at 80 °C for 10 min before application of the next layer. A total of 5 layers of paste were applied to each sample to

give a nominal film thickness of 6 μm for TiO_2 and 8 μm for SnO_2. The films were sensitized for 16 hours in a 0.1 mM solution of Ru(II)phos in anhydrous ethanol.

Core/shell structures were fabricated using a Savannah atomic layer deposition (ALD) system. As-prepared, sensitized TiO_2 and unsensitized SnO_2 films were placed in a 100 ^{0}C ALD chamber, which were ramped to reaction temperature and exposed to alternating pulses of metal oxide precursor and water vapor. Due to the high surface area of the films, each vapor pulse was held in the chamber for 180 s before purging with N_2 for 20 s. Four cycles of Al_2O_3 were deposited on sensitized TiO_2 films using trimethylaluminum as a precursor at a deposition temperature of 130 ^{0}C. The pulse sequence utilized alternating pulses of water vapor (0.015 s) and precursor (0.015 s). Forty cycles of TiO_2 were deposited on the unsensitized SnO_2 films using tetrakis(dimethylamido)titanium as the precursor (the precursor chamber was heated to 75 ^{0}C) with a deposition temperature of 150 ^{0}C and pulse durations of 0.03 and 0.25 s for the water vapor and precursor, respectively. Following the deposition, the SnO_2/TiO_2 electrodes were heated at 450 ^{0}C for 30 min. Approximately 0.4 nm of Al_2O_3 and 2.6 nm of TiO_2 were deposited as measured by ellipsometry on a Si wafer.

After sensitization, the samples were sealed using a second piece of fused quartz sandwiching a 60 μm thick Surlyn spacer (Solaronix). The samples were hot pressed at 250 °C for 45 seconds to melt the Surlyn. The solvent (either pH 1 $HClO_4$ or pH 6.8 100 mM potassium phosphate buffer) was introduced via vacuum backfilling through a previously drilled hole in the second piece of fused quartz. To improve the stability of the samples at pH 6.8, the phosphate buffer was briefly purged with nitrogen to remove oxygen prior to filling.[93] A second piece of Surlyn covered with a microscope coverslip was then used to seal the hole.

Scanning/transmission electron microscopy (S/TEM) and energy dispersive X-ray spectroscopy (EDS) were carried out on an FEI Talos F200X S/TEM instrument.

2.2.2 Time-Resolved THz Spectroscopy. A detailed description of the spectrometer and the technique is available elsewhere.[135,137–140] In short, the output of an amplified Ti:sapphire laser (Spectra-Physics), which produces 35 fs pulses centered at 800 nm at a repetition rate of 1 kHz, is split three ways into a THz generation beam, pump beam, and

detection beam. The pump beam is frequency doubled to 400 nm and attenuated using a variable neutral density filter to achieve a power of 100 mW (100 μJ/pulse) at a spot size of 10 mm, the beam is then passed through a 5 mm aperture before the sample. The THz generation beam is likewise frequency doubled and both the fundamental and second harmonic are focused in air to generate a plasma.[141,142] The forward propagating THz pulse generated by the plasma is collimated and focused using off-axis paraboloidal mirrors. The THz radiation is detected using free-space electro-optic sampling with a ZnTe(110) crystal.[143] The instrument response function of the spectrometer was described by a Gaussian function with a full-width at half-maximum (FWHM) of 0.5 ps. Samples with slow dynamics were collected with data acquisition parameters which yielded a time resolution of ~0.73 ps. Without considering scattering losses, the pump power used in this study results in the excitation of less than 3% of the sensitizers per pulse within the excitation volume.

The following function was fit to the TRTS scans:

$$\Delta THz = \left\{ \Delta THz_0 + \sum_{i=1}^{n} A_i \left[\exp\left(-\frac{t - t_0}{\tau_i} \right) - 1 \right] \right\} \otimes G\left(FWHM \right)$$

where THz_o is a small pre-zero baseline offset, n is the number of exponentials included in the fit, t_0 corresponds to the excitation "time-zero," A_i is the amplitude of a given component and τ_i is the time constant associated with that component, G(FWHM) represents a normalized Gaussian instrument response function, and ⊗ represents a convolution.

2.3 Results and Discussion

2.3.1 Injection into TiO_2. Previous work by Xiang et al.[131] and Giokas et al.[134] gave specific attention to the ultrafast injection dynamics of Ru(II)phos into TiO_2. Additional work by others has also considered injection by ruthenium polypyridyl complexes into TiO_2.[10,22,144] Therefore, we begin by considering the injection of Ru(II)phos into TiO_2.

Figure 2.1 shows the TRTS traces for Ru(II)phos injection into TiO_2 (Ru(II)phos-TiO_2) at pH 1 and pH 6.8 over short (<100 ps) and longer (950 ps) timescales. It is immediately apparent that the magnitude of the injection into the conduction band changes dramatically from pH 1 to pH 6.8. Assuming the electron mobility in TiO_2 remains constant between these two pH conditions, at 950 ps the injection amplitude (and carrier density) at pH 6.8 is roughly one third that of pH 1. If the injection efficiency is near unity at pH 1 then that suggests the upper limit of the injection efficiency at pH 6.8 is 33%, which is in good agreement with previous estimates of the injection efficiency.[38,45]

To fit the TRTS data, we utilized a triexponential function convoluted with a Gaussian instrument response function. This function fit the data well with R^2 values greater than 0.9. Compared to Giokas et al.[134] and Xiang et al.,[131] we observe significantly slower injection kinetics with time constants of 0.7 ps, 9 ps, and 80 ps at pH 1 and 1.3 ps, 33 ps, and 460 ps at pH 6.8 (Table 2.1). It is also possible that there is an additional slower injection (> 1 ns) component that we are unable to resolve with our optical delay stage. After injection we do not see any recovery of the THz amplitude associated with trapping of mobile electrons in sub-bandgap states. Thus trapping by sub-bandgap trap states must occur on timescales longer than ~1 ns.

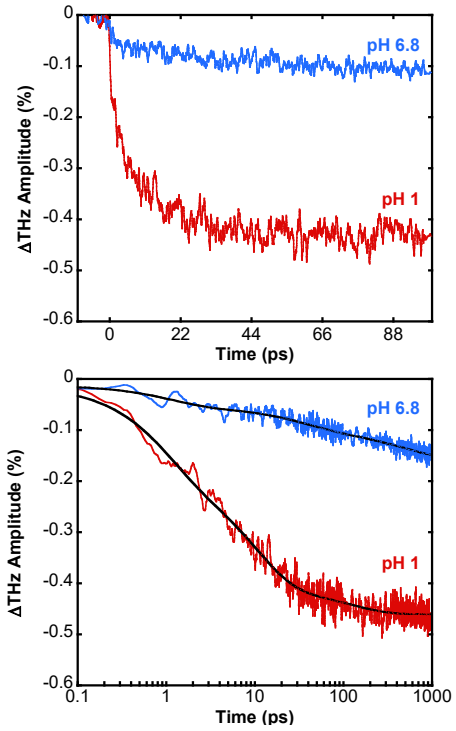

Figure 2.1. TRTS measurement of Ru(II)phos on TiO_2 at short (upper) and long (lower) time scales in 0.1M $HClO_4$ (pH 1, red) and 100 mM potassium phosphate buffer (pH 6.8, blue). Solid black lines are the fitted triexponential functions.

Probing in the mid-IR region, Xiang et al.[131] observed a sub-picosecond component, as well as a pair of components with 11 and 150 ps lifetimes. The sub-picosecond component accounted for 63% of the injection amplitude, while the process with the 150 ps time constant only accounted for 9% of the injection amplitude. It is worth noting that the samples in that study were in air, while our samples were sealed with solvent. Also, in the mid-IR free carriers and trapped electrons in the semiconductor are both detected. Of more direct comparability, Giokas et al.[134] observed injection via transient absorbance at pH 6.7 and found that 59% of the injection occurred within 1 ps, with the remaining 41% injection occurring on a 250 ps timescale. By comparison, we find that only 18% of the injection amplitude is related to the 1.3 ps time constant.

The differences in injection kinetics may be explained by a number of factors. The solvent used for dye deposition can influence electron transfer kinetics, even under identical measurement conditions.[38] Interfacial electron transfer kinetics on nanocrystalline metal oxides are significantly influenced by the surface chemistry and

defects of the nanoparticle, which may be different from study to study. It is also important to note that previous studies of the injection of Ru(II)phos into TiO_2 were sensitive to changes in the dye absorbance[134] and presence of an electron in TiO_2,[131] while in this study we observe mobile electrons (i.e. electrons in the conduction band of TiO_2). The discrepancy between transient absorbance measurements (>50% injection occurring within 1 ps) and TRTS measurements (17% of electrons in conduction band within 1 ps) suggests that at least some of the electron injection in WS-DSPECs follows a two-step process: (1) electrons are rapidly injected into non-mobile TiO_2 states, which are invisible to THz radiation, before (2) decaying into mobile conduction band states.

A two-stage injection process is not without precedent. Working with sensitized ZnO, Furube et al.[145,146] observed that the formation of the dye radical cation occurred on a much faster timescale than the appearance of mobile charges in the conduction band. They suggest that initially an exciplex is formed between the dye and a surface state, which later decays as electrons are transferred into the conduction band. It is possible that the discrepancy between the fast injection observed by transient absorbance and the slow appearance of mobile electrons observed by THz in this study may be related to such a phenomenon.

From the standpoint of a functioning WS-DSPEC, the slow kinetics in near-neutral conditions has important implications regarding device performance. Knauf et al. studied the recombination kinetics of Ru(II)phos and found that a significant fraction of injected electrons recombined on the tens of nanoseconds timescale.[70] This suggests that under the best conditions recombination may only be one or two orders of magnitude slower than the slow injection component and at worst may be occurring to some extent on the same timescale. For comparison, in dye-sensitized solar cells, which exhibit significantly better power conversion efficiencies than WS-DSPECs, the injection kinetics are 6-7 orders of magnitude faster than the major recombination pathway.[147]

2.3.2 Injection into TiO_2/Al_2O_3. Stabilizing dye-sensitized electrodes for long-term operation in oxygen-saturated conditions is an important goal for WS-DSPEC research. Recently Meyer and coworkers have introduced the so-called “mummy” strategy[74,75,82] whereby the sensitized metal oxide is covered by a metal oxide overlayer using ALD.

With the presence of an overlayer, the desorption rate constant can be decreased by nearly an order of magnitude relative to the uncoated films, offering a significant enhancement in long-term stability. Overlayers of Al_2O_3 are grown via a reaction of vapor phase $AlMe_3$ and hydroxyl groups on the surface of TiO_2 to generate Ti-O-$AlMe_2$ and subsequently converted to Ti-O-Al-$(OH)_2$ with the addition of water vapor.[75] Figure A.1 (Appendix A) shows that in the presence of Al_2O_3 there is slight broadening and red shift of the MLCT, however, there does not appear to be a significant loss of sensitizers following the ALD treatment.

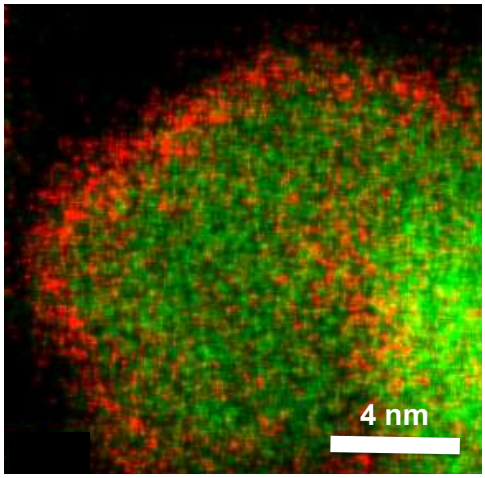

Figure 2.2. High resolution EDS mapping of TiO_2 particles with an ~0.4 nm overlayer of Al_2O_3. Aluminum is colored red and titanium is colored green.

Hanson et al.[75] briefly explored the interfacial electron transfer of a TiO_2 film sensitized with Ru(II)phos and coated by overlayers of Al_2O_3 of varying thicknesses. They found that as the overlayer thickness increased, both the rate of back electron transfer and the electron injection efficiency decreased, suggesting deposition of Al_2O_3 between the dye and TiO_2. Using a slightly modified procedure, we deposited an ~0.4 nm overlayer on a Ru(II)phos-sensitized TiO_2 film (Al_2O_3-Ru(II)phos-TiO_2). The Al_2O_3 layer is conformal (Figure 2.2) and uniform throughout the TiO_2 film.

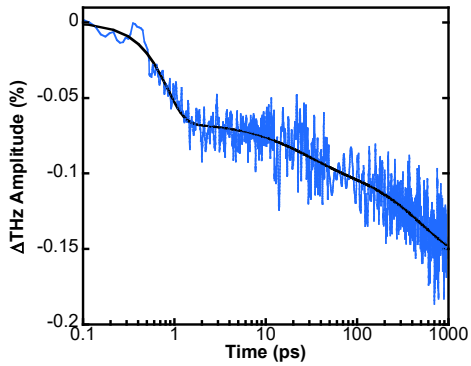

Figure 2.3. TRTS measurement of Al_2O_3-Ru(II)phos-TiO_2 in 100 mM potassium phosphate buffer (pH 6.8, blue). Solid black line is the fitted triexponential function.

To avoid acid hydrolysis of the Al_2O_3, we performed TRTS on Al_2O_3-Ru(II)phos-TiO_2 only at pH 6.8 (Figure 2.3). With a nominally identical sample, Hanson et al.[75] showed a 25% loss of injection efficiency with the introduction of the Al_2O_3 overlayer. Contrary to those results, we observe that at 950 ps the injection amplitudes are nearly identical between Al_2O_3-Ru(II)phos-TiO_2 and Ru(II)phos-TiO_2. This suggests that the Al_2O_3 overlayer may attenuate a slow injection process beyond the timescale we can observe. To gain insight into the electron injection kinetics, we fit a convoluted triexponential function to the TRTS scans of the Al_2O_3-coated sample, which yielded a fast, instrument response limited time constant of less than 0.5 ps as well as longer time constants of 25 ps and 545 ps (Table 2.1). There is a notable difference in the relative injection amplitudes between the two samples. In the uncoated TiO_2 sample, approximately 18% of the injection amplitude was related to injection on the ~1 ps timescale. With an overlayer of Al_2O_3, nearly 43% of the injection amplitude is associated with the 0.4 ps time constant, which is more consistent with the results of Giokas et al.[134] and Xiang et al.[131]

Injection into TiO_2 with ruthenium polypyridyl dyes can occur via a "hot injection" from the singlet state, ^{1}MLCT, or can occur from the relaxed triplet state, ^{3}MLCT, which is properly described as a manifold of triplet states. Injection from the ^{1}MLCT state is rapid and generally occurs on sub-picosecond timescales.[22,144] In this and in previous studies[131,134] the fast injection component can be reasonably assigned to dye molecules in

the ^{1}MLCT state, while the slower components are generally assigned to injection from the triplet manifold.

In the presence of an Al_2O_3 overlayer we see a better than 2-fold enhancement in the number of electrons appearing in the conduction band within one picosecond. We propose that this enhancement in the fast injection component is related to passivation of surface states that can act as non-mobile trap states (Scheme 2.1). Hupp and coworkers,[76] who studied electron tunneling behavior through metal oxide shells deposited by ALD, found that a single ALD cycle of TiO_2 on a SnO_2 particle could significantly slow the rate of electron transfer from the SnO_2 conduction band to an I_3^- acceptor in solution. Their interpretation was that this single ALD cycle passivated surface states that facilitated electron transfer into solution. We suggest that the same phenomenon may be responsible for the enhancement of the fast injection component in Al_2O_3-coated sample: injection from ^{1}MLCT proceeds directly into the conduction band of TiO_2 without going through a surface intermediate. Because the slower time constants (likely related to injection from the ^{3}MLCT) are relatively unaffected by the Al_2O_3, we can speculate that the energies of the non-mobile surface states lay above that of the ^{3}MLCT. A more detailed study is needed to confirm this proposed injection mechanism.

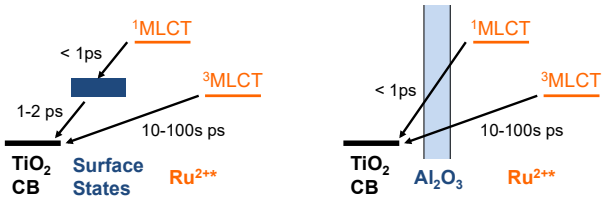

Scheme 2.1. Proposed injection scheme for bare (Ru(II)phos-TiO_2) and Al_2O_3 overlaid (Al_2O_3-Ru(II)phos-TiO_2) samples. For bare samples, injection from the singlet (^{1}MLCT) proceeds through non-mobile surface states, which subsequently decay into the conduction band (TiO_2 CB). In the presence of the Al_2O_3 overlayer, injection proceeds directly from ^{1}MLCT to the conduction band.

2.3.3 Injection into SnO_2. Few sensitizers are able to attain the sufficiently positive ground state potential required to drive a water oxidation catalyst at neutral pH. Furthermore, of those molecules that can drive water oxidation, even fewer possess an

excited state sufficiently negative to transfer an electron into TiO_2. With a conduction band 500 mV more positive than TiO_2 and a higher electron mobility, SnO_2 has recently gained attention as an intriguing alternative to TiO_2 in WS-DSPECs.[24] Despite these desirable qualities, electron injection into SnO_2 is notoriously slow; this effect is generally attributed to a low density of conduction band states in SnO_2.[12,14]

Table 2.1. Fit Parameters for Figure 2.1, Figure 2.3, Figure 2.4, and Figure 2.6

Oxide	pH	A_1	τ_1 (ps)	A_2	τ_2 (ps)	A_3	τ_3 (ps)	A_4	τ_4 (ps)	THz_o	t_0 (ps)	FWHM (ps)	Scaling Factor
TiO_2	1	0.54	0.7	0.36	9.0	0.10	79.8			0.00	-1.1	0.73	-0.65
	6.8	0.18	1.3	0.36	33	0.47	460			0.00	-0.5	0.73	-0.12
TiO_2/Al_2O_3	6.8	0.43	< 0.5	0.17	26	0.40	547			0.00	0.1	0.5	-0.16
SnO_2	1	0.32	1.7	0.50	9.4	0.18	37.4			0.00	0.0	0.73	-1.2
	6.8	0.23	7.7	0.62	50	0.15	435			0.01	-1.3	0.73	-1.2
SnO_2/TiO_2	1	0.13	< 0.5	-0.12	1.4	0.49	98	0.38	388	0.00	0.0	0.5	-0.67
	6.8	0.20	< 0.5	-0.12	1.1	0.23	95	0.57	430	0.00	0.0	0.5	-0.39

A_1, A_2, A_3, and A_4 are normalized amplitudes

The FWHM value was fixed during the fit

Figure 2.4 shows the TRTS traces for Ru(II)phos injection into SnO_2 (Ru(II)phos-SnO_2) at pH 1 and pH 6.8 on both short and long timescales. As with TiO_2, the injection is more rapid at pH 1 than at pH 6.8. For pH 1, the lifetimes extracted by fitting a convoluted triexponential to TRTS traces were 1.7, 9, and 37 ps, while at pH 6.8 the function generates lifetimes of 7.7, 50, and 435 ps (Table 2.1). Unlike the case of Ru(II)phos-TiO_2, the overall injection amplitude at pH 6.8 reaches that at pH 1 at a time-delay of 950 ps, despite slower injection kinetics. With SnO_2 there is still a significant driving force for injection even at pH 6.8, allowing for a more complete injection than in the case of TiO_2. Interestingly, the major difference in the injection kinetics between SnO_2 and TiO_2 is in the initial fast component. At pH 6.8, fast injection into TiO_2 occurred with a time constant of 1.2 ps, whereas the "fast" component of injection into SnO_2 occurred with a time constant of 7.7 ps.

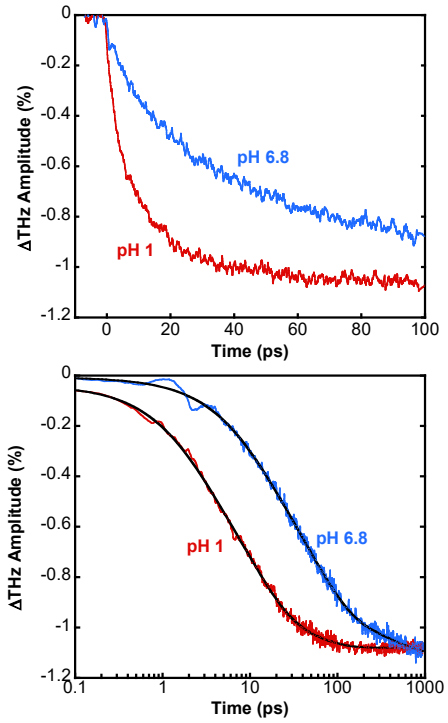

Figure 2.4. TRTS measurement of Ru(II)phos on SnO_2 at short (upper) and long (lower) time scales in 0.1 M $HClO_4$ (pH 1, red) and 100 mM potassium phosphate buffer (pH 6.8, blue). Solid black lines are the fitted triexponential functions.

Xiang et al.[131] also probed the ultrafast dynamics of Ru(II)phos injection into SnO_2 using transient absorbance. Looking at samples in air, they observed lifetimes of 4 ps, 30 ps, and 224 ps, with the injection amplitude split uniformly between the three components. Due to different experimental conditions it is difficult to make a direct comparison with this study, however, we note that at pH 6.8 we see somewhat slower injection kinetics. As with TiO_2, this could imply a similar initial injection into non-mobile states, however, more work is needed to confirm this.

2.3.4 Injection into SnO_2/TiO_2. Back electron transfer is an overwhelming limitation to power conversion efficiencies in WS-DSPECs.[45] One potentially promising strategy is to utilize a core-shell electrode where the electron either tunnels through a thin layer of a wide bandgap metal oxide[73] or proceeds through a "cascade" mechanism wherein the electron is first injected into the conduction band of the shell before relaxing into the

conduction band of the core. Recently Meyer and coworkers have demonstrated an enhancement in photocurrent and stability with WS-DSPECs utilizing SnO_2-cores, TiO_2-shells (hereafter SnO_2/TiO_2) prepared by ALD.[78,79,129] Because of the offset in conduction band potentials, back electron transfer in these electrodes is slowed by approximately an order of magnitude, though the initial injection kinetics are poorly characterized.

Figure 2.5 shows a high resolution EDS image of a pair of SnO_2 particles coated with approximately 2.5 ± 0.1 nm of TiO_2 using ALD. The TiO_2 shell is conformal and uniform throughout the film. This thickness was chosen to correspond to recent work by Meyer and coworkers.[78,79,129] Figure A.1 (Appendix A) shows that addition of the TiO_2 overlayer increases the background scattering, however, when correcting for scattering a nearly identical amount of sensitizer is deposited.

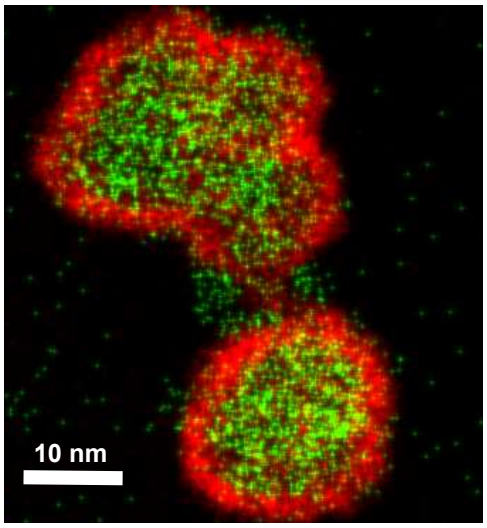

Figure 2.5. High resolution EDS mapping of SnO_2/TiO_2 particles. Titanium is colored red and tin is colored green.

Figure 2.6 shows the TRTS scans for the sensitized Ru(II)phos-SnO_2/TiO_2 films at pH 1 and pH 6.8. The injection kinetics are markedly different when compared to bare SnO_2. One significant difference is that over the 1 ns time scale of the measurement, the injection amplitude does not reach the same magnitude as with Ru(II)phos-SnO_2. This may reflect slower injection kinetics and/or a loss of driving force related to the presence of the TiO_2 shell.

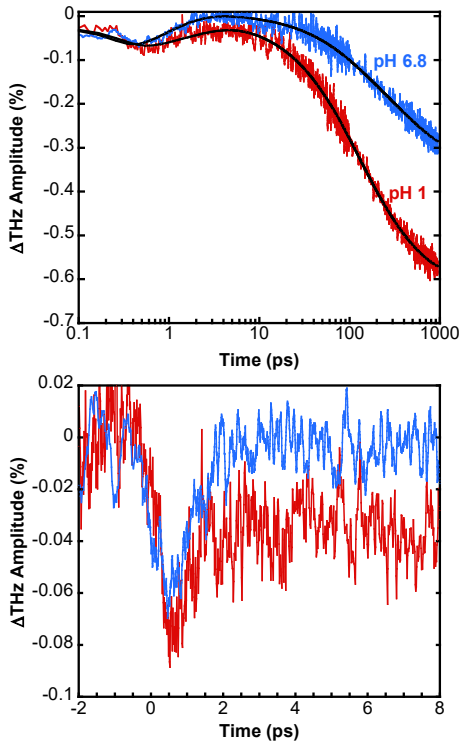

Figure 2.6. (upper) TRTS measurement of Ru(II)phos on SnO_2/TiO_2 in 0.1M $HClO_4$ (pH 1, red) and 100 mM potassium phosphate buffer (pH 6.8, blue). Solid black lines are the fitted functions described in text. (lower) Initial time kinetics of Ru(II)phos on SnO_2/TiO_2 in 0.1M $HClO_4$ (pH 1, red) and 100 mM potassium phosphate buffer (pH 6.8, blue).

A second significant difference is the striking feature immediately after time-zero in the TRTS scans of Ru(II)phos-SnO_2/TiO_2. Initially there is an extremely fast change in THz amplitude, indicating a rapid injection component, which decreases in intensity over a few picoseconds before evolving into slower injection dynamics. Due to this feature, the overall dynamics are not well fit using a convoluted triexponential function, but rather require a four-component function to accurately reproduce the initial kinetics. The initial rapid amplitude change is limited by instrument response, while the relatively slower recovery of the THz amplitude occurs with a time constant of 1.4 ps. There are two additional time constants of 98 and 388 ps associated with the increase in carrier generation following the initial feature. One interpretation is that the initial fast injection and decay correspond to injection into mobile TiO_2 states followed by decay into non-mobile states at the SnO_2/TiO_2 interface and/or in the TiO_2 shell. The slow components

(98 and 388 ps) may relate to electrons being released from non-mobile states and injected into conduction band of the SnO_2 core.

The kinetics are similar at pH 6.8. There is the same instrument response limited rapid injection and amplitude loss as observed at pH 1, however, nearly all the initial amplitude loss is recovered over 1-2 ps. The extracted long time constants (95 and 430 ps) are also very similar to the long time components at pH 1. The similarity in time constants and difference in injection amplitude strongly suggest that in both samples the slow kinetics are related to electron release from non-mobile trap states into the SnO_2 (Scheme 2.2).

At a TiO_2 thickness of ~2.5 nm, tunneling is unlikely on this timescale,[148] and thus the injection efficiency is likely controlled by the energetics of the TiO_2. Due to Nernstian behavior, the relative energy difference between the conduction band of TiO_2 and SnO_2 will be pH independent. Assuming that the energy of the non-mobile trap states is also Nernstian, the release kinetics from these states would also be expected to be independent of pH, which is consistent with the observed behavior. As we observed above, injection at pH 1 is significantly more efficient than pH 6.8 because of the additional 340 mV of driving force. A detailed study to better understand the injection and trapping behavior in SnO_2/TiO_2 films is planned.

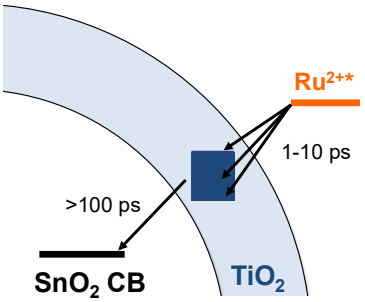

Scheme 2.2. Proposed injection scheme for Ru(II)phos-TiO_2/SnO_2. The excited dye rapidly injects into the TiO_2-shell. Despite some injection into mobile TiO_2 states the electrons eventually reside in non-mobile trap states that slowly decay over 100+ ps into the SnO_2.

2.4 Conclusion

In this paper, we have reported the first TRTS study of four common electrode designs used in WS-DSPECs. By using the same sensitizing and measurement conditions, we are able to directly compare the kinetics between these configurations. Generally, electron injection is more rapid and efficient at pH 1 than at pH 6.8, which is expected based on the increased driving force for injection at pH 1. For both Ru(II)phos-TiO_2 and Ru(II)phos-SnO_2, the appearance of electrons in the conduction band is significantly slower than indicated by transient absorbance experiments under comparable conditions. This suggests a two-step mechanism in these systems in which some electrons are first injected into non-mobile states before decaying into the conduction band. When the Ru(II)phos-TiO_2 surface is passivated with an overlayer of Al_2O_3, the overall injection amplitude at 950 ps remains unchanged but a larger fraction of electrons are injected on a sub-picosecond time scale.

A marked change in the injection behavior is observed when a Ru(II)phos-SnO_2/TiO_2 core-shell architecture is utilized. We observe a rapid injection and decay behavior that we assign to injection into the TiO_2 shell and subsequent relaxation into non-mobile trap states. Electrons in these non-mobile states slowly decay into SnO_2 over hundreds of picoseconds. As expected, the release kinetics from these non-mobile states appears to be largely pH independent. A detailed study into the injection and trapping behavior of core-shell electrodes is planned.

Chapter 3

Proton-Induced Trap States, Injection and Recombination Dynamics in Water-Splitting Dye-Sensitized Photoelectrochemical Cells

Nicholas S. McCool,[1] John R. Swierk,[2] Coleen T. Nemes,[2] Timothy P. Saunders,[1,†] Charles A. Shmuttenmaer,[2,*] Thomas E. Mallouk[1,3,4,*]

[1]Department of Chemistry, [3]Department of Biochemistry and Molecular Biology, and [4]Department of Physics, The Pennsylvania State University, University Park, Pennsylvania 16802, United States

[2]Department of Chemistry and Engineering Sciences Institute, Yale University, 225 Prospect Street, P.O. Box 208107, New Haven, Connecticut 06520-8107, United States

In review at *ACS Applied Materials and Interfaces*.

3.1 Introduction

Wide band gap semiconductors are ubiquitous in the field of solar photochemistry, finding use in a variety of applications such as dye-sensitized solar cells, photocatalysts for environmental remediation or fuel generation, and gas sensors. Of these semiconductors, titanium dioxide (TiO_2) has found the broadest range of application.[149] Unlike many metal oxides, TiO_2 is stable in both acidic and basic media, absorbs near-visible UV to generate a charge-separated state, has a high density of states in the conduction band and is a good photoconductor. There is also increasing interest in TiO_2 as an electronic material given that it is the most common support in dye-sensitized solar cells, and shows promise as a conductive protective layer for photocathodes.[2,5,150,151] As a result of the prevalence of TiO_2 in these applications, understanding electron transport in this material is extremely important.

Electron mobility in high surface area polycrystalline TiO_2 films is several orders of magnitude lower than in single-crystal TiO_2 due to an exponential distribution of trap states at energies below the conduction band edge.[42,43,152,153] In these films, the trap states are largely associated with particle-particle grain boundaries and oxygen vacancies.[42] Diffusion of electrons through these films is further limited by local electric field screening within the film by electrolyte in solution[152] as well as by a simple geometric restriction imposed by the porous nature of the film, as has been shown in porous Si films.[58] This forces the electron motion to be largely diffusion-based, i.e., a random walk through the film in order to exit the electrode at the back contact. Therefore, the electron collection efficiency relies on a complex diffusion pathway in the film comprised of many trapping/detrapping events on the one to tens of nanoseconds timescale.[43,49,154]

Proton intercalation has been shown to widely occur in TiO_2 electrodes.[49,51,52,155–161] It can occur as a charge compensation mechanism for electron injection and has been shown to occur in solutions with very dilute proton concentrations ($-\log(a_{H^+})=23$).[156] Intercalation occurs through protons disrupting the lattice and forming stable Ti^{3+}-OH or Ti^{3+}-H bonds, which produce shallow traps near the conduction band (CB) edge of TiO_2.[53,54,157,160,161] Although the traps are shallow, the lifetime of a trapping event can be up to tens of milliseconds as a result of the electrostatic charge of the traps.[49] Because

they are surface states, proton-induced trap states can contribute substantially to the rate of recombination with oxidized dyes on the surface.[162] Here, we use water-splitting dye-sensitized photoelectrochemical cells (WS-DSPECs) as a platform to further understand the trapping dynamics related to intercalated protons in TiO_2.

WS-DSPECs are an intriguing option for renewable solar fuel generation.[5] Modeled after the standard dye-sensitized solar cell (DSSC), a mesoporous metal oxide semiconductor anode (commonly TiO_2 or core-shell TiO_2/SnO_2[78,79]) is functionalized with a light absorbing molecular sensitizer and a water oxidation catalyst. Under illumination, an excited electron is transferred from the sensitizer into the semiconductor conduction band and oxidizing equivalents diffuse across the surface via a series of intermolecular electron transfers between dye molecules to create a spatially charge-separated state. The electron diffuses through the TiO_2 to a transparent conducting oxide and eventually through an external circuit to a dark cathode where protons are reduced to generate hydrogen while the reduced sensitizer on the surface is regenerated by electron transfer from the water oxidation catalyst.

In WS-DSPECs, regeneration of the dye relies on electrons from the water oxidation half reaction. Because this is a four-electron four-proton catalytic process, regeneration is relatively slow and, as a result, recombination of electrons from the TiO_2 with the oxidized dye molecules is the primary fate of photogenerated electrons, with as many as 98% of electrons rapidly recombining with dye molecules; less than 2% of injected electrons persist to timescales relevant to solar fuel production.[45]

Commonly in WS-DSPECs, the dye is deposited from an aqueous 0.1 M $HClO_4$ solution or from water as this produces a monolayer coating of dye with the most efficient hole transport kinetics.[38,75,80,163] However, we have previously demonstrated that depositing dye from protic solvents results in the formation of proton induced trap states that have a deleterious effect on overall device performance.[38] The mechanism by which the proton-induced trap states impacts overall device performance is poorly understood. Herein, we revisit the issue of proton intercalation in order to gain a more comprehensive understanding of why proton intercalation results in poor device performance.

By coupling transient absorption spectroscopy (TAS), which utilizes changes in dye absorbance to observe recombination kinetics, and time-resolved terahertz spectroscopy

(TRTS), which probes mobile electrons once they are in the conduction band of the electrode, we are able to detail the fate of an electron from the timescale of injection (fs-ns) through the timescale of recombination (ns-ms). This enables a deeper analysis of the relationship between trapping events and recombination. We demonstrate that proton-induced trap states act as non-mobile acceptor states which promote charge recombination on the microsecond timescale. We also demonstrate that by applying a mild heat treatment under vacuum to samples freshly deposited with dye from $HClO_4$, the peak performance of these cells exceeds those prepared from aprotic solvents. This is likely a result of the vacuum treatment effectively removing the proton-induced trap states.[162]

3.2 Experimental Section

3.2.1 Photoanode Preparation. Bis(2,2'-bipyridine)(4,4'-diphosphonato-2,2'-bipyridine)-ruthenium bromide, [Ru(II)phos], was synthesized as previously reported.[94] Different TiO_2 pastes were used for different experiments. For THz spectroscopy, TiO_2 paste was synthesized as previously reported as this paste adhered well to the quartz substrates.[136] The paste used for all other experiments was synthesized via a modified procedure.[164] Briefly, 12 g of glacial acetic acid was added all at once to 58.6 g of rapidly stirring titanium isopropoxide (>97.0%, Sigma). The solution was stirred for 15 minutes and then added all at once to 290 ml of water. After stirring for 1 hour, 4 ml of concentrated nitric acid was added and then the reaction was refluxed at 80 ^{0}C for 75 min. The reaction solution was distributed to bomb reactors and heated to 250 ^{0}C for 12 hours. The resulting particles were sonicated using a horn (Branson, 450 W) to create a suspension and were then centrifuged and washed with ethanol three times. Following the third centrifugation, a solution of 6 g ethyl cellulose (Sigma, 48.0-49.5% w/w ethoxyl basis) in 56 g of terpineol (Sigma, 65% α-, 10% β-, 20% γ- mixture) and 300 ml of anhydrous ethanol were added to the particles and sonicated to resuspend the particles. The ethanol was then stripped via rotary evaporation to leave the final viscous and translucent TiO_2 paste. Photoanodes were prepared as previously reported using a doctor blading method[123] and then sintered at 300 ^{0}C for 20 min, 350 ^{0}C for 10 min and 500 ^{0}C

for 30 min. Electrodes were sensitized with 100 μM Ru(II)phos in anhydrous, denatured ethanol or 0.1 M $HClO_4$ (aq) for 20 hours. Slides that received the vacuum-heating treatment were placed in a dark vacuum chamber under dynamic pumping using a standard oil pump at 200 mtorr with a trap to prevent backstreaming for 24 hours at 80 ^{0}C (heating under vacuum ($HClO_4$-HV) treatment) following dye deposition.

Thicker films needed for THz measurements were made by doctor blading multiple times on a fused quartz substrate using one tape spacer each time with a curing step at 80 ^{0}C for 10 minutes between each deposition. The films were then sensitized and sealed using a 60 μm thick Surlyn (Solaronix) spacer and a second piece of quartz. The slides were hot-pressed together at 250 ^{0}C for 45 s to melt the Surlyn and seal the slides together. The empty space between the slides was vacuum-filled through a small hole in the top piece of quartz with 100 mM pH 6.8 potassium phosphate buffer that had been previously purged with N_2 to remove air. The samples were then sealed using a second piece of Surlyn and a microscope coverslip.

3.2.2 Measurements and Characterization. All photoelectrochemical experiments were carried out using a 300 W Xe arc lamp attenuated with an A.M. 1.5 filter to obtain an intensity of 100 mW/cm^2. A 410 nm long pass filter was placed in front of the sample to eliminate direct band gap excitation of the TiO_2. The photoanodes were tested in an H-cell configuration in 100 mM sodium phosphate buffer (NaPi) at pH 6.8. The anode and a Ag/AgCl (3 M NaCl) reference electrode were placed together in the anode compartment and a Pt mesh was placed in the cathode compartment, separated by a glass frit.

Chronoamperometry was measured using a Pine Instruments bipotentiostat. Prior to each experiment, the cathode compartment was purged with 5% hydrogen balanced with argon. The anode was then biased at 100 mV vs. Ag/AgCl (3 M NaCl) and after several seconds was exposed to light for the duration of the experiment.

Chronopotentiometry was carried out using a Metrohm Autolab potentiostat operated in galvanostatic mode. The photoanode and Ag/AgCl (3M NaCl) reference electrode were placed together in one compartment of an H-cell configuration and a Pt mesh acted as the counter electrode in the second compartment. Electrodes were held at open circuit

conditions under illumination and the generated open circuit photovoltage between the working and reference electrode was recorded.

For transient absorption spectroscopy (TAS) measurements, sensitized electrodes were placed in degassed 100 uM pH 6.8 KPi buffer and irradiated with 420 nm light through a monochrometer. The samples were photoexcited with a 2 mJ 530 nm laser pulse.

The spectrometer used for time-resolved transient spectroscopy (TRTS) is described elsewhere.[135,137–140] Briefly, the output of a Spectra-Physics Ti:Sapphire regenerative amplifier generating 35 fs pulses at 800 nm with a repetition rate of 1 kHz was split into 3 beams: a pump beam, a generation beam, and a detection beam. The pump beam was frequency-doubled to 400 nm then passed through a variable neutral density filter to a final power of 100 mW/cm^2. The generation beam was focused along with the second harmonic in air to generate a plasma which, in turn, generated the THz radiation used to probe the sample conductivity. The transmitted THz amplitude was detected using free-space electro-optic sampling with a ZnTe(110) crystal.[143] TRTS traces were fit with the following function:[21]

$$\Delta\mathrm{THz} = \left\{\Delta\mathrm{THz}_0 + \sum_{i=1}^{n} A_i \left[\exp\left(-\frac{t-t_0}{\tau_i}\right) - 1\right]\right\} \otimes \mathrm{G(fwhm)} \qquad \text{(Eq. 3.1)}$$

where THz_0 is a baseline offset, *n* is the number of exponentials used in the fit, t_0 refers to the excitation time-zero, A_i is the amplitude of the given component, and τ_i is the time constant associated with that component. G(fwhm) represents a normalized Gaussian instrument response function and $\otimes$ is a convolution.

3.3 Results

3.3.1 Photoelectrochemical Water Oxidation. Photoelectrochemical water oxidation requires a catalyst to drive the half reaction in these systems. Despite this, Fielden et al. recently reported photoelectrochemical water oxidation in a dye-sensitized cell without the intentional addition of a catalyst.[132] It is likely that this is a result of catalytically active metal impurities in the starting reagents or leached from glassware or apparati used

in the experiments.[165,166] In this work, we observe the same effect, with oxygen evolution quantified in a well-established generator-collector electrode configuration[3,26,122,132] (Figure B.1). The details of this experiment are discussed in Supporting Information. Because the identity of the water oxidation catalyst is not critical for this work, we used the active electrodes as prepared.

Recently, we analyzed the effect of the solvent from which the dye was deposited on the performance of WS-DSPECs.[38] Despite faster hole transfer across the surface between dye molecules, samples where dye was adsorbed from a 0.1 M $HClO_4$ aqueous solution had dramatically poorer performance than those prepared from neat ethanol. This was attributed to proton intercalation into the crystal lattice of the TiO_2, which resulted in long-lived, shallow trap states that hindered electron mobility. The effect of proton-induced trap states is visible in Figure 3.1a (red trace). In this case, the as-prepared electrodes from $HClO_4$ (Ru-$HClO_4$) show an initial current spike to 202 ± 29 μA/cm^2 before rapidly polarizing to below 5 μA/cm^2 after a few seconds. Interestingly, when Ru-$HClO_4$ slides are exposed to the HV treatment (Ru-$HClO_4$-HV, Figure 3.1a, blue), the peak performance of the devices recovers and reaches 772 ± 36 μA/cm^2. This is nearly double the peak photocurrent for as-prepared EtOH slides (Ru-EtOH, Figure 3.1a, black), which reaches an average peak photocurrent of 441 ± 19 μA/cm^2. However, the Ru-$HClO_4$-HV slides also appear to suffer from very rapid current polarization, similar to the Ru-$HClO_4$ slides.

In order to understand the differences in the polarization of these electrodes, samples were prepared using various combinations of soaking in $HClO_4$, depositing dye from EtOH, the HV treatment or additional sintering steps. Samples were prepared by soaking the electrodes in 0.1 M $HClO_4$ (aq) before (Figure 3.1b, red) and after (Figure 3.1b, black) dye deposition in order to determine if simply exposing the electrode to $HClO_4$ caused the poor performance. Samples were also prepared by subjecting electrodes soaked in $HClO_4$ to either the HV treatment (Figure 3.1b, pink) or a second sintering step (Figure 3.1b, green) before dye deposition to gain insight in to how effectively the HV treatment revitalizes the samples following exposure to $HClO_4$. Additional samples were prepared by exposing fresh TiO_2 electrodes to a second sintering step (Figure 3.1b, blue) before dye deposition from EtOH in order to rule out any effects of the second sintering

step on photoelectrochemical performance. The results are summarized in Figure 3.1b. It is clear from the photocurrent data that any exposure to perchloric acid has a similar effect on the overall performance and polarization. Device performance is then only recovered if followed by the HV treatment, which improves the peak photocurrent, or a sintering step, which improves both the peak and extended performance. The HV treatment, when followed by the dye deposition step, still produces an electrode with poor performance and rapid polarization. This is in contrast with the electrodes that were subjected to an additional sintering step before dye deposition, which resulted in recovery of the initial photocurrent spike as well as slower polarization.

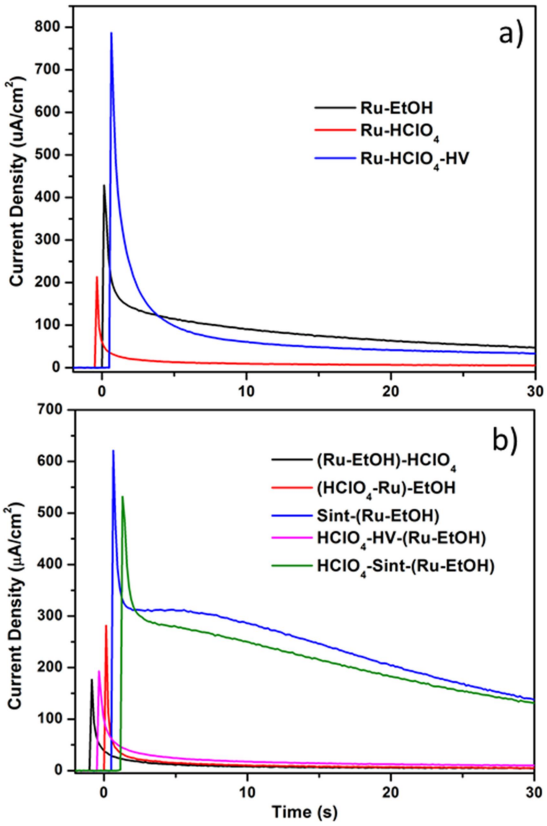

Figure 3.1. (a) Chronoamperometric water oxidation traces for TiO_2 electrodes in which Ru(II)phos was adsorbed from ethanol (black) and $HClO_4$ with (blue) and without (red) heated vacuum treatment prior to testing. (b) Chronoamperometric traces for TiO_2 electrodes sensitized with dye from EtOH with soaking steps in 0.1 M $HClO_4$(aq) after (black) and before (red) dye deposition, an $HClO_4$ soak and HV treatment (pink) or sintering step (green) before dye deposition, and an as-prepared TiO_2 slide sintered an additional time before dye deposition (blue). The dye deposition step is denoted with parentheses. Current was measured at a bias of 100 mV vs. Ag/AgCl (3 M NaCl) in 100 mM pH 6.8 sodium phosphate buffer. Samples were illuminated from time zero for the duration of the experiment, traces are offset by 0.5 s from each other about time zero for clarity.

Chronopotentiometry shows a similar trend in overall photovoltage. The photovoltage is defined as the difference between the potential of the Fermi level in the TiO_2 and the potential of the H_2O/O_2 couple (0.631 mV at pH 6.8).[38] Because the potential of the water/O_2 redox couple is fixed by pH, chronopotentiometry is a good probe of the quasi-

Fermi energy of TiO_2 on longer time scales. Figure 3.2 shows the photovoltage, defined as the photogenerated difference between the TiO_2 Fermi level and the potential of the H_2O/O_2 couple at pH 6.8. Interestingly, the dark resting potential for these electrodes is about 600-700 mV negative of the H_2O/O_2 couple in the dark, meaning that the TiO_2 surface is not initially in electrochemical equilibrium with the H_2O/O_2 redox couple. This effect has been observed previously, and is connected with the fact that the TiO_2 surface is a poor catalyst for oxygen reduction in the dark.[38,45,167] This dark potential difference may be a consequence of electrons in long-lived trap states that are photogenerated before the photoelectrochemical experiment begins. As expected, upon illumination the open circuit photovoltage for Ru-EtOH electrodes grows smoothly over several seconds and reaches a value of about 1.3 V, which is stable for several minutes (Figure 3.2, black).

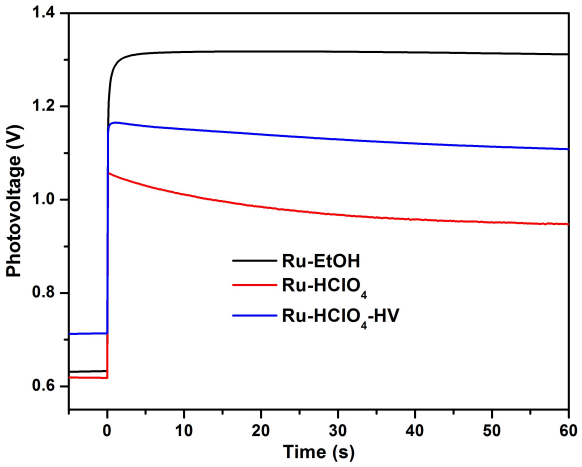

Figure 3.2. Representative chronopotentiometry traces for electrodes sensitized with Ru(II)phos dye from ethanol (black) and $HClO_4$ with (blue) or without (red) heated vacuum treatment. Electrodes held at open circuit galvanostatically in 100 mM pH 6.8 NaPi buffer and illuminated for the duration of the experiment beginning at time zero.

Similarly, upon illumination, the Ru-$HClO_4$ electrodes demonstrate the same instability in photovoltage as shown in the photocurrent (Figure 3.2, red). The photovoltage likely does not decay as quickly as the photocurrent because these are open circuit experiments and charge is not passing. Illumination results in a spike to nearly 1.1 V followed by a decay to below 1 V. In comparison, the Ru-$HClO_4$-HV electrodes both

demonstrate a higher initial photovoltage than the Ru-$HClO_4$ electrodes as well as a more stable photovoltage (Figure 3.2, blue). Interestingly, however, these electrodes produce lower photovoltages than the Ru-EtOH slides despite having a higher initial photocurrent.

3.3.2 Transient Absorption Spectroscopy. Protons are known to function as recombination centers in TiO_2.[38,49,162] Thus, in order to elucidate the mechanism by which protonation affects overall device performance, transient absorption spectroscopy (TAS) was used to measure recombination dynamics. When the dye injects an electron into the TiO_2, the formation of the oxidized dye leads to a bleach of the metal to ligand charge transfer (MLCT) band centered around 450 nm.[1] Following photoinjection, electrons from the TiO_2 then recombine with the oxidized sensitizer, which results in the recovery of the MLCT absorbance. By monitoring the bleaching and recovery of the MLCT absorbance the recombination kinetics can be directly measured. Charge injection typically occurs on the timescale of fs to ps,[134] which cannot be resolved with nanosecond transient absorption spectroscopy. However by using an identical sensitizer and probing samples with comparable optical densities, the magnitude of the bleach can yield information about the relative injection efficiencies resulting from different electrode treatments.

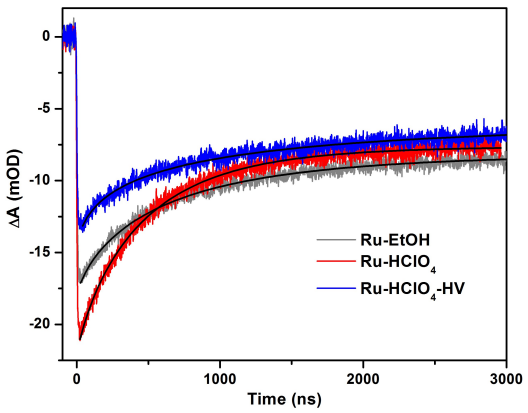

Figure 3.3. Transient absorption traces at 420 nm for TiO_2 electrodes sensitized with dye from ethanol (gray) and $HClO_4$ without (red) and with (blue) the heating vacuum treatment. Spectra were collected in N_2-purged 100 mM pH 6.8 potassium phosphate buffer. Stretched exponential fits are shown in black. Data was smoothed using a 3 point moving average.

The recombination process in sensitized TiO_2 electrodes is complicated as a result of the exponential distribution of trap states below the CB[42,43,152,153] and is usually fitted using a stretched exponential function. A stretched exponential describes a single kinetic process that has a distribution of activation energies, e.g. recombination from various trap state energy levels. The transient absorption traces in Figure 3.3 were fitted with a stretched exponential of the form (Figure 3.3, black lines):

$$y = A * \exp\left(\frac{-t}{\tau}\right)^{\beta} + y_0$$

where τ is the lifetime of the oxidized dye, β is a stretching parameter that represents the breadth of the distribution of activation energies for electron transfer, and can range from 0 to 1, A is a scaling factor, and y_0 is an offset. The average lifetime can be determined using the following analytical expression for the area under the stretched exponential curve:[168,169]

$$< \tau_{ww} > = \frac{\tau}{\beta}\Gamma\left(\frac{1}{\beta}\right),$$

where Γ is the gamma function. A representative recombination rate, k_{rec}, can be taken as the reciprocal of $<\tau_{ww}>$.

Ru-EtOH (gray trace), Ru-$HClO_4$ (red trace) and Ru-$HClO_4$-HV samples (blue trace, Figure 3.3) all show a MLCT bleach characteristic for the formation of Ru(III). The injection efficiencies resulting from the three treatments are similar, with the Ru-$HClO_4$ having the highest injection yield and the Ru-$HClO_4$-HV having the lowest. The recombination kinetics for the Ru-$HClO_4$-HV samples (k_{rec} = 9.91 (± 0.13) x 10^5 s^{-1}) are about twice as fast as for Ru-EtOH (k_{rec} = 4.76 (± 0.20) x 10^5 s^{-1}), while recombination in Ru-$HClO_4$ is significantly more rapid (k_{rec} = 1.70 (± 0.02) x 10^6 s^{-1}).

3.3.3 Time-Resolved THz Spectroscopy. The nature of protonation is directly related to trapping events in the TiO_2 which should ideally be probed directly. Whereas TAS is sensitive to changes in dye absorption related to changes in oxidation state, TRTS is

sensitive to mobile electrons in the TiO_2. Conductivity is proportional to the product of mobility and charge density. Therefore, by utilizing a single material (i.e., TiO_2), the mobility is constant and any differences are due to differences in charge densities, which are directly related to electron injection efficiencies. Mobile electrons in the TiO_2 absorb/reflect THz radiation, which results in a decrease in transmitted THz amplitude.

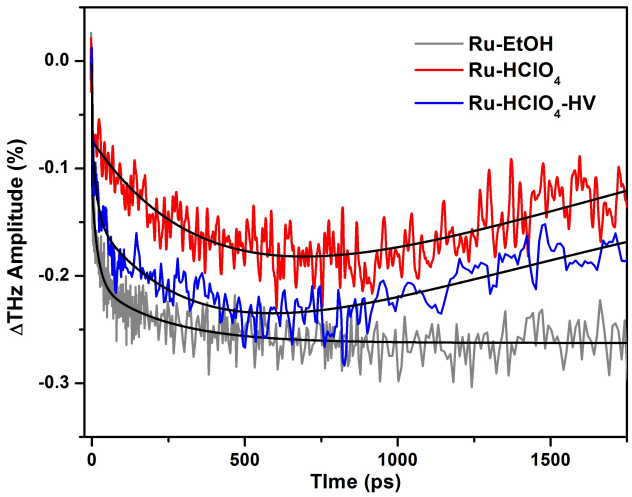

Figure 3.4. THz scans for quartz/TiO_2 slides sensitized with Ru(II)phos from ethanol (grey) and $HClO_4$, without (red) and with (blue) heating under vacuum after dye deposition. Spectra were collected in solvent-sealed devices using N_2 purged 100 mM pH 6.8 potassium phosphate buffer.

Figure 3.4 shows the TRTS scans for Ru-EtOH (grey), Ru-$HClO_4$ (red) and Ru-$HClO_4$-HV (blue) slides, fits of equation 3.1 are overlayed on the respective traces in black and fitting parameters are summarized in Table B.1 in Appendix B. The injection component for Ru-EtOH and Ru-$HClO_4$-HV are fit with a triexponential; the Ru-$HClO_4$-HV requires a forth exponential to describe the trapping dynamics. Ru-$HClO_4$ injection is well described by a biexponential with a third exponential to fit the trapping. Injection occurs over approximately 1 ns, which is consistent with our previous results.[21] As can be seen, after 900 ps the Ru-EtOH slides exhibit a larger attenuation of the THz amplitude than Ru-$HClO_4$, which corresponds to nearly twice the density of mobile electrons within the material after 1 ns. However, in the case of the Ru-$HClO_4$-HV, the THz attenuation

that was initially lost during the $HClO_4$ deposition step is mostly recovered by mildly heating the electrode under vacuum, reaching a maximum attenuation very similar to the Ru-EtOH samples after 1 ns. Between 1 ns and 1.5 ns, both samples exposed to $HClO_4$ show rapid trapping dynamics, demonstrated by the recovery of the THz amplitude, while the Ru-EtOH samples show very little change in THz amplitude after the injection finishes.

3.4 Discussion

3.4.1 Interfacial Electron Transfer Dynamics. TAS and TRTS are complimentary techniques; TAS probes the recombination of photoinjected electrons via the change in absorbance of the MLCT band of the dye whereas TRTS can analyze the mobility of an electron directly in the material following charge injection. This allows for a broader understanding of the fate of electrons through the processes of injection, trapping and eventually recombination.

The timescales of electron injection, recombination, and trapping under illumination are summarized in Scheme 3.1.

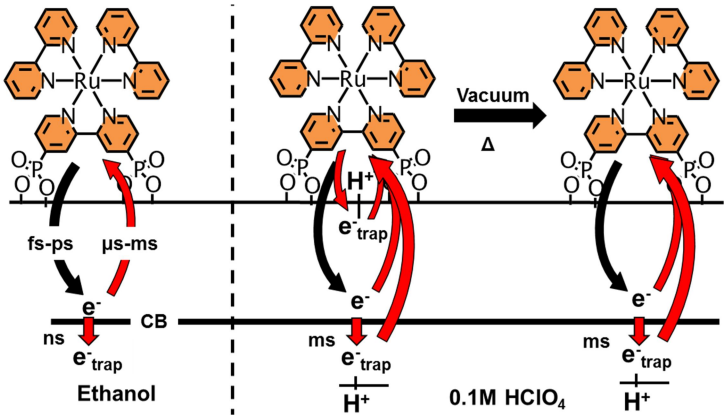

Scheme 3.1. Timescales for the electron pathway from charge injection to recombination, favorable electron transfer events are shown in black, unfavorable are shown in red. Electrons are photoinjected into mobile conduction band (ethanol) or immobile proton induced surface trap states ($HClO_4$) on the fs-ns timescale. Recombination from the semiconductor occurs in the μs to ms range. In Ru-EtOH electrodes, trapped electrons persist for tens of nanoseconds before thermalizing and diffusing via a trapping/detrapping random walk process. Proton-induced trap states can be surface states that accept photoinjected electrons directly from the sensitizer or bulk states that can trap electrons from the conduction band. Proton-stabilized electrons remain trapped for tens of milliseconds and can readily recombine from surface states with oxidized dye molecules. Heating these electrodes under vacuum successfully removes surface states; however, bulk trap states remain unaffected.

Injection from the sensitizer into the TiO_2 occurs on the fs to ns timescale,[10,22,134] with the electrons appearing in the conduction band on the ps to ns timescale.[21] The TRTS scans shown in Figure 3.4 agree with this picture, with mobile electrons appearing on timescales of tens to hundreds of ps. Only mobile electrons in the CB of the TiO_2 absorb/reflect THz radiation so, as seen in Figure 3.4, the Ru-EtOH slides show a higher yield of mobile electrons when compared to the Ru-$HClO_4$ slides. In contrast, the TAS data (Figure 3.3) show that the Ru-EtOH slides have a weaker bleaching signal and, correspondingly, a lower injection yield than films sensitized from perchloric acid. This suggests that electrons are injected more efficiently in the case of the Ru-$HClO_4$, but that a greater fraction of them are injecting into non-mobile acceptor states. Injection into

non-mobile surface states has been observed before in this system[21] and on ZnO sensitized with N719 dye.[145,146] The data in Figure 3.3 and Figure 3.4 suggest that the "missing" photoinjected electrons in Ru-$HClO_4$ are in proton-stabilized trap states near the surface of the TiO_2. Electrons injected directly into or rapidly trapped by these non-mobile acceptor states are invisible to TRTS. This "missing" injection pathway is further supported by the fitting of the TRTS data. The Ru-EtOH samples are fit with a triexponential, with lifetimes of <0.5, 19.1, and 231.1 ps, whereas the injection process for Ru-$HClO_4$ samples only required a biexponential fit with lifetimes of 0.8 and 460.1 ps. At much longer timescales, trapping occurs in the Ru-$HClO_4$ electrodes and by normalizing the injection amplitude to the injection, it can be seen that with a lifetime of 2348 ps, all of the mobile electrons will be trapped by these proton-induced trap states. The Ru-EtOH slides show no trapping dynamics in the timescale of the experiments.

Recombination in Ru-$HClO_4$ samples is also more rapid, with the rate constant for recombination nearly 4 times larger than for Ru-EtOH. Qualitatively this can be seen by observing (Figure 3.3) that within 1 μs more than 50% of the injected electrons have recombined with the oxidized sensitizer in Ru-$HClO_4$, while at 3 μs only about 30% of the injected electrons in Ru-EtOH have recombined. The shorter lifetime observed in the Ru-$HClO_4$ samples can be explained by considering the nature of the proton-induced trap states. These trap states seem to dominate the trapping dynamics and are expected to be primarily surface states and electrostatically charged. As a result, the traps are energetically shallow (due to their charged nature) and can persist for up to tens of milliseconds,[49] or up 6 orders of magnitude longer than the average trapping lifetime in TiO_2 (one to tens of nanoseconds) and at best a similar timescale to recombination (100s of nanoseconds to milliseconds). Because these trap states are surface bound and long-lived, they have a large impact on recombination kinetics, reducing the early-time lifetime of the electrons by 25%. In WS-DSPECs, rapid recombination is arguably the most significant pathway for loss of efficiency, with 98% of injected electrons recombining with a dye cation in less than 1 ms.[45]

Interestingly, when the as-prepared $HClO_4$ slides are subsequently exposed to heating under vacuum, the resulting TRTS scans demonstrate a nearly complete recovery of the mobile electron density in the material, as shown in Figure 3.4. The lifetime for the

injection processes for the Ru-$HClO_4$-HV slides are <0.5, 16.5, and 402.3 ps, very similar to the Ru-EtOH samples aside from the longest lifetime component. Because the longest lifetime component for the Ru-$HClO_4$-HV samples is similar to that for the Ru-$HClO_4$ samples, it seems that this injection pathway could be tied to the proton-induced trap states, which is slowing down how rapidly the mobile electrons appear in the TRTS traces compared to the Ru-EtOH samples. When coupled to the TAS traces, which show a reduced injection efficiency for the Ru-$HClO_4$-HV slides when compared to untreated slides, this further demonstrates that the proton-induced trap states are acting as non-mobile acceptor states to charge injection.

Despite a higher density of mobile electrons than the untreated slides, electron trapping appears to remain an issue in Ru-$HClO_4$-HV samples. Surprisingly, it appears that all of the mobile electrons are being trapped in the Ru-$HClO_4$-HV samples as well, with a trapping lifetime of 1960.6 ps. Interestingly, this suggests that, despite effectively removing the trapping acceptor states, the HV treatment is not completely removing the trap states associated with proton intercalation. It is possible then that the HV treatment is merely removing proton-induced trap states on the surface of the TiO_2 and once electrons move from the surface, they are still trapped by inner proton-induced states.

The trapping found in Ru-$HClO_4$-HV electrodes is consistent with the intermediate recombination dynamics observed for Ru-$HClO_4$-HV samples in Figure 3.3. Figure 3.3 shows that the recombination kinetics for the Ru-$HClO_4$-HV samples are only half as fast as those of the original Ru-$HClO_4$ samples. Taken together, these results suggest that heating under vacuum successfully removes the acceptor states induced by proton intercalation into TiO_2; however an issue still remains at longer time scales.

3.4.2 Implications for WS-DSPEC performance. In WS-DSPECs, the photovoltage and the corresponding device performance are controlled by the position of the Fermi level within the TiO_2, which in turn is dictated by the interplay of injection, recombination, and regeneration. We previously demonstrated that devices sensitized from ethanol had stable open-circuit photovoltages in excess of 1.1 V,[123] which is consistent with the results shown in Figure 3.2. We also see a peak current density in Ru-EtOH samples consistent with our previous results. Similarly, the Ru-$HClO_4$ slides

behave consistently with expectations from earlier work.[38] Upon illumination, the Ru-$HClO_4$ electrodes show a spike in both the photocurrent as well as the photovoltage. The lower overall photovoltage generated from the Ru-$HClO_4$ electrodes indicates a lower Fermi energy in the TiO_2 as a result of proton-induced trap states, as was suggested by the faster recombination and trapping kinetics of Ru-$HClO_4$. This is consistent with shallow proton-induced trap states that promote recombination with oxidized dye molecules on the surface. This also suggests an explanation for the rapid decay in photovoltage as electrons are quickly trapped and thus the mobile electron density within the material is reduced.

Following the HV treatment, the Ru-$HClO_4$-HV electrodes appear to initially recover in both photocurrent and photovoltage, which suggests that heating under vacuum has briefly eliminated the proton-induced trap states by removing the protons from the TiO_2. This has been previously demonstrated by Schulberg et al., who found that (Ba,Sr)TiO_3 that was initially intercalated with deuterium by annealing under a partial D_2 atmosphere could successfully be stripped of D through mild heating under vacuum or at elevated temperatures under an oxygen atmosphere.[162] The initial spike in photocurrent, which exceeds that of Ru-EtOH electrodes, is likely a result of more rapid hole transport kinetics across the surface, as previously measured for Ru-$HClO_4$ electrodes.[38] Interestingly, however, the photovoltage of Ru-$HClO_4$-HV does not exceed that of Ru-EtOH electrodes. This is likely a result of the poor stability of the Ru-$HClO_4$-HV electrodes. It is clear from Figure 3.4 that the recovery in performance from the HV treatment is temporary, where trapping still occurs at time scales faster than the EtOH. These electrodes polarize within the first 5 seconds of illumination (Figure 3.1) and, in fact, produce less photocurrent than the Ru-EtOH electrodes after only a few seconds. Previously, we have shown that degraded electrodes have similar impedance spectra as electrodes freshly prepared from perchloric acid, suggesting that protons generated by water oxidation at the surface of the electrode are intercalated.[38] This suggests that higher photocurrents, i.e. a higher flux of photoelectrochemically generated protons, would result in more rapid polarization in the photocurrent.

In order to gain a deeper understanding of the polarization of the Ru-$HClO_4$ and Ru-$HClO_4$-HV electrodes, samples were prepared with varying orders of exposure to

perchloric acid as well as the HV treatment or an additional sintering step. The most obvious trend shown in Figure 3.1b is that any exposure to $HClO_4$ that is not immediately followed by sintering has a detrimental effect on device performance and stability. Because sintering the electrodes after exposure to the protic solvent not only recovers the initial peak performance but also slows the polarization, this suggests that it could be related to a structural effect. In fact, Mao et al. have demonstrated that, beginning with polycrystalline anatase nanocrystals, proton intercalation results in a dramatically disordered crystal lattice at the surface of the particle, while maintaining an ordered core.[53,54] They suggest that the intercalated protons act to stabilize the distorted lattice by binding to dangling bonds at the surface of the particle.

The instability of electrodes that were not exposed to the second sintering step suggests that something qualitatively similar could be happening with these devices during a soak in a protic solvent. This can also help explain why the electrode that was exposed to $HClO_4$, the HV treatment and then had dye deposited from EtOH performed similarly to the Ru-$HClO_4$ samples; the HV treatment appears to only remove the proton-induced trap states without restoring crystallinity to the TiO_2 film. Surface protons are possibly being driven off as water molecules, removing surface oxygen atoms along with the intercalated proton and leaving a further disrupted lattice as a result. A similar process has been observed with proton-exchanged layered titanates. Upon heating, water is lost to collapse the interlayer galleries resulting in materials with varying degrees of crystallinity.[170–172] As these topochemical dehydration processes are often reversible, re-intercalation of protons may occur after HV treatment, explaining the bulk instability of HV electrodes. Water electrolysis increases the proton concentration at the surface of the electrode and may allow intercalation to occur as a charge compensation mechanism for photoinjected electrons.[173] It is also possible that the HV treatment fails to remove protons that migrate further in to the bulk. This hypothesis supports the trapping dynamics from Figure 3.4; the HV treatment eliminates the trapping acceptor states on the surface without affecting the trapping dynamics observed for the untreated electrodes because proton-induced traps persist in the bulk of the material.

3.5 Conclusion

Recombination of trapped electrons with oxidized dye molecules accounts for the fate of the vast majority of injected electrons in WS-DSPECs. Proton intercalation during exposure to protic solvents results in shallow, long-lived electrostatically charged trap states. These trap states act as non-mobile acceptors and trap electrons directly after injection. These trap states persist for much longer times than the typical lifetime of electrons in TiO_2, which results in efficient electron recombination with surface-bound oxidized dye molecules. As a result, proton-induced trap states exacerbate a problem that already dramatically lowers the efficiency of water splitting in dye-sensitized photoelectrochemical cells. These proton-induced trap states appear to be temporarily removed by heating under vacuum but are removed more completely by sintering the electrode after exposure to protic solvents. The weakness of the HV treatment suggests there might be various stages of proton intercalation, having both surface and bulk sites. This procedure should enable future studies to take advantage of protic solvents for deposition processing and dye deposition without the corresponding loss in device performance.

Chapter 4

Dynamics of Electron Injection in SnO_2/TiO_2 Core/Shell Electrodes for Water-splitting Dye-sensitized Photoelectrochemical Cells

Nicholas S. McCool,[1] John R. Swierk,[2] Coleen T. Nemes,[2] Charles A. Schmuttenmaer,[2] Thomas E. Mallouk[1,3,4]

[1]Department of Chemistry, [3]Department of Biochemistry and Molecular Biology, and [4]Department of Physics, The Pennsylvania State University, University Park, Pennsylvania 16802 United States

[2]Department of Chemistry and Energy Sciences Institute, Yale University, 225 Prospect Street, P.O. Box 208107, New Haven, Connecticut, 06520-8107, United States

Submitted to *the Journal of Physical Chemistry Letters.*

4.1 Introduction

Harnessing and converting solar energy into a useful form, e.g. electricity or a chemical fuel, on a terawatt scale is among the most critical scientific challenges of the 21st century.[174] Natural photosynthesis does so, but with inherent efficiency limitations that can be surpassed in artificial systems.[175] In natural photosynthesis, a hierarchical assembly of light harvesting pigments funnel excitation energy into a reaction center, where a series of sub-nanosecond electron transfers occurs to yield a charge separated state with nearly 100% quantum efficiency.[119,176,177] Efficient charge transfer in natural photosynthesis relies on a finely optimized electron transfer cascade between the various donor and acceptor species. Achieving the same level of control over electron transfer events is a central goal of artificial photosynthesis, which seeks to develop artificial systems capable of using solar energy to photocatalytically drive water splitting and other fuel-forming endergonic reactions.[178–180]

Water-splitting dye-sensitized photoelectrochemical cells (WS-DSPECs) utilize a semiconducting metal oxide film sensitized with a molecular dye, which absorbs visible light and injects an electron into the oxide semiconductor. Holes diffuse across the surface via a series of lateral electron transfer events between dye molecules until they arrive at a catalytic site. This process repeats until the catalyst collects enough holes to oxidize water, generating molecular oxygen and four protons. The injected electrons diffuse through the electrode to a transparent conductive oxide electrode, and ultimately to a dark cathode where protons are reduced to hydrogen.[5]

Unfortunately, the quantum efficiencies of WS-DSPECs are typically only a few percent because the hole transport and catalytic water oxidation processes are slow.[122] As a result, rapid recombination between the injected electron and the oxidized dye is the dominant mechanism for efficiency loss in these devices.[45] The use of visible-absorbing dyes that are sufficiently oxidizing to drive water oxidation near neutral pH results in low injection yields into anatase TiO_2 (η_{inj} = 20-30%).[21,26,45] As an alternative, research on WS-DSPECs has focused on using SnO_2 as the electrode material.[78,79] SnO_2 has a conduction band minimum (CBM) several hundred millivolts below that of TiO_2,[21,64,65] which can lead to improved injection yields[21] and might be expected to reduce the driving

force for recombination. However, the rate of recombination has been found to be much faster for SnO_2 than for TiO_2 electrodes.[64,71]

One strategy for retarding recombination while maintaining efficient injection is the use of a core/shell electrode architecture.[73] Recent work by Meyer and coworkers demonstrated a SnO_2/TiO_2 core/shell structure prepared by atomic layer deposition (ALD) of TiO_2 on SnO_2 nanoparticles that results in an electron transfer cascade from the dye excited state into TiO_2 and subsequently into the SnO_2 CB, as shown in Scheme 4.1.[78,79] They observed efficient electron injection, slower recombination kinetics, and an overall enhancement in device performance. Knauf et al.[80] explored recombination with TiO_2 shells of varying thickness on SnO_2 and ZrO_2. Interestingly they found that for shells thicker than 3.5 nm, electron recombination originated from localized electrons in the TiO_2 shell, whereas for thinner shells recombination proceeded via a tunneling mechanism. Recently, we studied the ultrafast injection dynamics of sensitized bare-SnO_2 and SnO_2 coated with 2.5 nm of TiO_2 using time-resolved terahertz spectroscopy (TRTS).[21] In that study, we demonstrated that addition of the TiO_2 markedly changed the injection kinetics. We suggested that an initial ultrafast injection component not apparent with bare SnO_2 demonstrated injection into the TiO_2 shell, which was followed by fast trapping and subsequent electron release into SnO_2 on a much longer timescale. In this study, we revisit that system and use TRTS and steady state emission measurements to probe the electron injection process as a function of shell thickness.

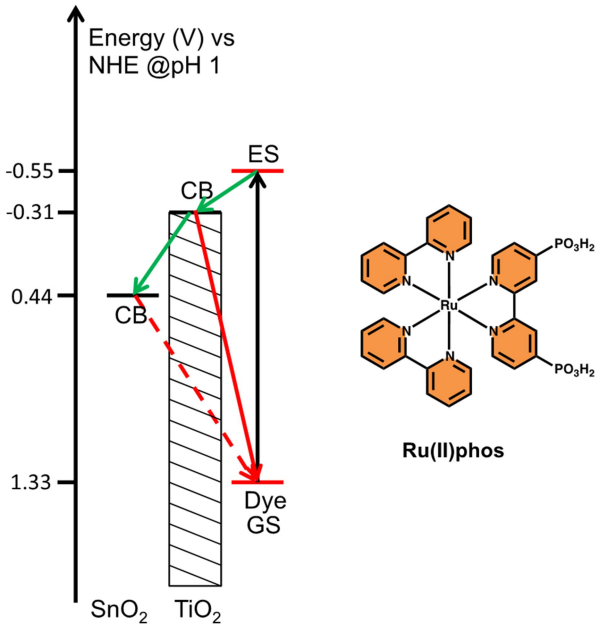

Scheme 4.1. Energy diagram for the SnO_2/TiO_2 structure and structure of Ru(II)phos. Potentials for ES and GS of Ru(II)phos taken from ref. 1, for oxide CBM taken from ref 65.

4.2 Results and Discussion

We utilized atomic layer deposition (ALD) to prepare TiO_2 shells of varying thickness on mesoporous SnO_2. ALD is a well-established technique for the deposition of conformal, atomically thin films of metal oxides on surfaces and has been used with great success in mesoporous structures.[181,182] Our previous work deposited 40 cycles of TiO_2 on SnO_2, resulting in a film thickness of 2.5 nm as measured by deposition on a Si wafer.[21] This normalization infers a deposition of about 0.63 Å per cycle. In order to gain a better understanding of when shell material impacted charge injection, we varied the shell thickness from one to 40 pulse cycles, or a nominal thickness range of sub-monolayer coverage up to 2.5 nm. This deposition process was also carried out on porous nanocrystalline ZrO_2 films in order to probe how effectively the TiO_2 shell alone with varying thicknesses could accept electrons from the dye.

Figure 4.1 shows the peak emission for both SnO_2/TiO_2 and ZrO_2/TiO_2 core/shell structures sensitized with Bis(2,2′-bipyridine)(4,4′-diphosphonato-2,2′-

bipyridine)ruthenium(II) bromide (Ru(II)phos) (Scheme 4.1) at pH 1. Because both SnO_2 and TiO_2 accept electrons from the excited state of the dye, we anticipated significant emission quenching due to injection in the SnO_2/TiO_2 architecture at any thickness of TiO_2, as can be seen in Figure 4.1 (red squares). In the case of the ZrO_2/TiO_2 samples, the ZrO_2 core has a CBM well above the excited state potential of the dye, such that the core should not be able to quench the excited state of the dye. This can be seen in Figure 4.1 (blue circles) where there is significant emission intensity when the TiO_2 shell is thin. With thicker TiO_2 shells, the emission intensity decreases until about 13 Å of TiO_2, after which it is similar to SnO_2/TiO_2, suggesting nearly complete excited state quenching by electron transfer. This suggests that for shell thicknesses below ~2 Å tunneling through the TiO_2 dominates,[76] whereas beyond 10 Å of TiO_2, only the electron cascade is occurring. At intermediate thicknesses, a combination of tunneling and/or electron cascade may be occurring. In this size regime, quantum confinement effects can occur, resulting in an increase in the band gap and a shift of the CBM to more negative potentials.[183]

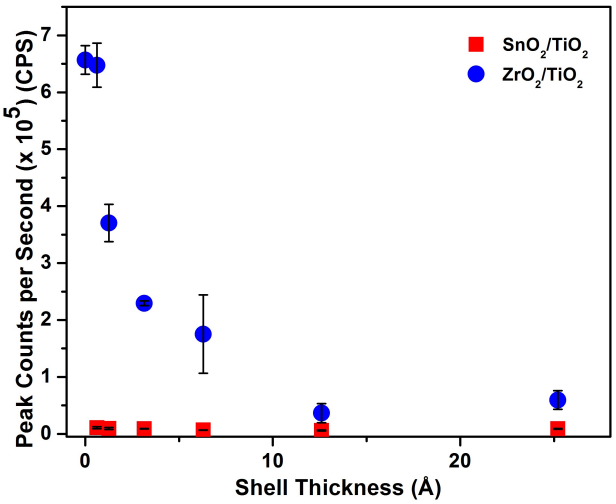

Figure 4.1. Peak emission intensity between 510 and 800 nm measured from Ru(II)phos-sensitized core/shell films with varying thicknesses of the TiO_2 shell on a SnO_2 core (red squares) and a ZrO_2 core (blue circles). Emission was measured in N_2-purged, 0.1 M $HClO_4$ (pH 1) aqueous solution.

We can gain insight into the mechanism of charge transfer (i.e., tunneling or cascade) by monitoring the ultrafast injection kinetics. Despite having a lower CBM energy (and as a result, a higher driving force for injection and lower driving force for recombination), SnO_2 still exhibits slow injection dynamics[12,21,69] when compared to TiO_2. The slow injection kinetics are a result of a low density of states (DOS) in the SnO_2 CB,[12] which is comprised primarily of Sn^{4+} s and p orbitals,[12] whereas TiO_2 has a high DOS due to the CB being made up of mostly Ti^{4+} d orbitals.[11,27] To understand the effect of TiO_2 shell thickness on injection, we utilized time-resolved TRTS, which is an ultrafast, far-infrared technique that is sensitive to changes in conductivity.[21,135,137,138,140] Electrons injected into mobile states (e.g., the conduction band) attenuate transmitted terahertz (THz) radiation such that increases in conductivity following injection are observed as a decrease in the transmitted THz amplitude. Additionally, because the conductivity change depends in part on the electron mobility, TRTS is ideally suited for distinguishing whether the electron is located in the TiO_2-shell or SnO_2-core on the basis of the difference in electron mobility between the two materials.

Figure 4.2 shows the TRTS traces (black) and respective fits (red) using Equation C.1 in Appendix C. The fitting parameters are summarized in Table C.1 in Appendix C. In order to ensure that the decrease in THz attenuation for thicker films is not a result of a lower dye concentration due to blocked pores, UV/Vis spectra were measured for all samples. A summary of the surface coverage for each set of thicknesses is shown in Figure C.1, and it is seen that the coverages are nearly within experimental error of each other. In fact, thicker shells show slightly increased dye loading, and would therefore not be expected to show diminished injection amplitude based on dye loading alone. The injection component of all traces from bare SnO_2 to 6 Å of TiO_2 were successfully fit using a three exponential equation, though slow trapping dynamics observed in the bare samples required a fourth exponential (with a negative amplitude to represent trapping) to be included in the fit. Films coated with 12.5 and 25 Å required a fourth exponential to accurately reproduce trapping which occurs in the initial (0-5 ps) dynamics.

Surprisingly, we observe a higher THz attenuation for samples coated with 0.6 and 1.3 Å of TiO_2 when compared to bare SnO_2, corresponding to a higher density of mobile electrons in the SnO_2 film. As the dye loading is identical between these samples, we

suggest that the increase in injection amplitude is related to passivation of non-mobile surface states. These non-mobile states can act as acceptors states for charge injection and, as a result, will not be observed with TRTS. The passivation of these states is further supported by the lack of slow trapping in any of the ALD coated samples when compared to the bare SnO_2. Hupp and coworkers observed a similar passivation of surface states with ALD.[76]

The dynamics observed for the 25 Å sample agree very well with our previous report on this system.[21] In that report, we assigned the rapid (<0.5 ps) decrease and recovery of the THz amplitude from 0-5 ps as rapid injection into TiO_2 followed by trapping within the TiO_2 or at the TiO_2/SnO_2 interface, with release into the SnO_2 core (Figure 4.2b) at longer timescales. We can clearly distinguish an ultrafast injection component for samples with a TiO_2 shell of 6 Å or more, which strongly suggests that electrons are injecting directly into the TiO_2 shell because injection into TiO_2 is much faster than into SnO_2, which is attributed to a higher DOS in the TiO_2 CB than in SnO_2 as described above.[21] A fast trapping component can be clearly distinguished with increasing shell thickness (Figure 4.2b), suggesting that the trapping sites are located in the TiO_2 shell and not at the SnO_2/TiO_2 interface.

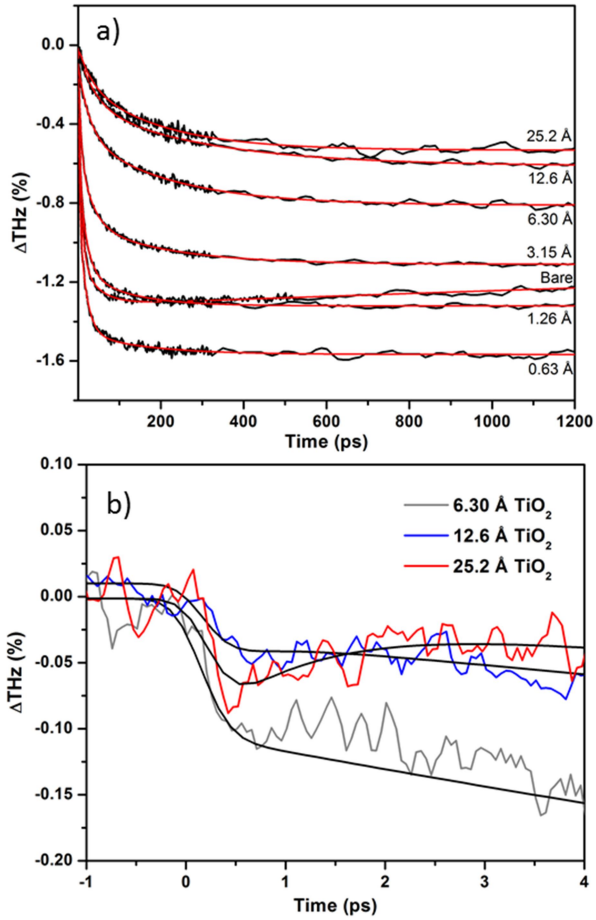

Figure 4.2. (a) Long timescale time-resolved THz spectroscopy (TRTS) traces for SnO_2/TiO_2 electrodes with varying shell thicknesses. (b) Short timescale plot of the TRTS traces of thicker shell samples from (a) in order to show the evolution of the initial injection into the TiO_2 shell with increasing thickness. TRTS scans collected in a 0.1 M pH 1 $HClO_4$ aqueous solution.

Figure 4.3 shows the scaling factor and electron transfer rate, $1/\langle\tau_w\rangle$, where τ_w is a weighted average of the injection lifetimes, as a function of shell thickness (Table C.1). The scaling factor is directly proportion to the number of mobile electrons and thus by extension to the injection amplitude. Interestingly, we find that the rate of electron transfer becomes largely constant after approximately 5 Å of TiO_2, which is consistent with steady state emission data for sensitized TiO_2/ZrO_2. This suggests that after 5 Å the excited state of the dye "senses" only the TiO_2 shell. It is surprising then that we do not also see a leveling of the scaling factor. One likely explanation is that as the TiO_2 shell

increases in thickness more electrons are injected into non-mobile sites. The increase in trapping within the shell with increasing shell thickness observed in Figure 4.2b supports that hypothesis. This is also consistent with work by Knauf et al. who directly observed the recombination rate of electrons with oxidized Ru(II)phos in SnO_2/TiO_2 structures and found that beyond a few nanometers, recombination occurs entirely from the TiO_2 shell.[80]

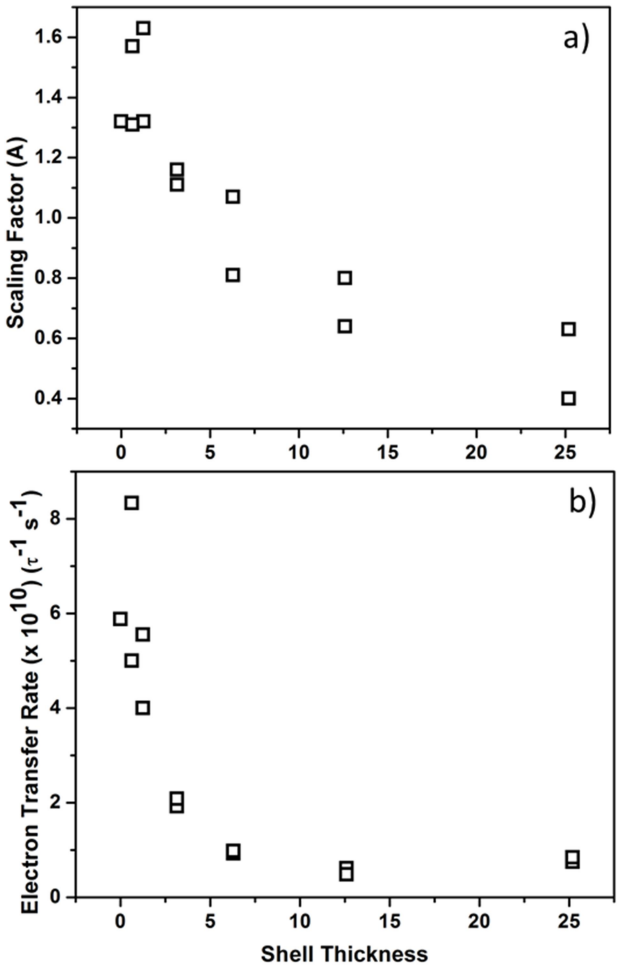

Figure 4.3. (a) Scaling factor and (b) weighted rate of electron transfer from fits to TRTS traces in Figure 4.2 for varying shell thicknesses.

While TRTS has been used to probe core/shell nanostructures,[184,185] this and our previous study[21] are the first to explicitly follow the movement of an electron through the shell and into the core, demonstrating the power of TRTS for these types of architectures. By varying the thickness of the TiO_2 shell, we were able to demonstrate that electron

injection proceeds directly into the SnO_2 core when the TiO_2 shell is less than 5 Å, but when the thickness is greater than 5 Å, it is injected first into the TiO_2 shell and then moves to the SnO_2 core. Furthermore, we were able to demonstrate that trapping of carriers into non-mobile sites occurs specifically within the TiO_2 shell. The degree of trapping in this shell increases with increasing shell thickness, further demonstrating the need to balance injection and recombination dynamics through an optimal shell thickness.

Chapter 5

Electron Injection Through Insulating SnO_2/ZrO_2 Core/Shell Electrodes for Water-Splitting Dye-Sensitized Photoelectrochemical Cells

Nicholas S. McCool,[1] John R. Swierk,[2] Svante Hedström,[2] Coleen T. Nemes,[2] Victor S. Batista,[2] Charles A. Schmuttenmaer,[2] Thomas E. Mallouk[1,3,4]

[1]Department of Chemistry, [3]Department of Biochemistry and Molecular Biology, and [4]Department of Physics, The Pennsylvania State University, University Park, Pennsylvania 16802 United States

[2]Department of Chemistry and Energy Sciences Institute, Yale University, 225 Prospect Street, P.O. Box 208107, New Haven, Connecticut, 06520-8107, United States

5.1 Introduction

In natural photosynthesis, water is split into molecular oxygen and reducing equivalents. The photosynthetic process derives its success from designing a charge separated state through a series of energy-cascade electron transfers which eventually are used to reduce CO_2 into usable products. Artificial photosynthesis aims to produce efficient photosystems that split water or reduce CO_2 to fuels using nature as a blueprint. Water-splitting dye-sensitized photoelectrochemical cells (WS-DSPECs) are devices designed after the Gratzel dye sensitized solar cell (DSSC) that use visible light to split water into oxygen and hydrogen gas.[3] A porous metal oxide electrode film sensitized with a molecular absorber absorbs light and from its excited state injects an electron into the conduction band of the metal oxide. Electrons percholate through the metal oxide, through an external circuit to a dark cathode where they are used to reduced protons to hydrogen. The resulting holes on dye molecules diffuse to catalytic sites to oxidize water and replenish electrons in the system. The tunable nature of WS-DSPECs offers an opportunity to design a system that also relies on specific electron transfer processes that facilitates a long-lived charge-separated state.

Despite the promise of WS-DSPECs, overall efficiencies remain low. Because water oxidation serves as the electron source in WS-DSPECs, regeneration of the oxidized dye by hole-transfer to the catalyst is a critical step, and is slow relative to back electron transfer.[122] As a result, recombination between the injected electron and the oxidized dye is the dominant mechanism for efficiency loss in these devices, with up to 98% of injected electrons undergoing fast recobmination.[45] In an attempt to improve these losses, recent research on WS-DSPECs has moved to SnO_2, which has a CBM several hundred millivolts positive of TiO_2[21,64,65] and higher mobility than this standard oxide support.[61,64] This is expected to lead to better injection yields[21] and to reduce the driving force for recombination. Interestingly however, the rate of recombination has been found to be much faster for SnO_2 than for TiO_2.[64,71]

Core/shell architectures represent one method for controlling charge transfer processes at the WS-DSPEC anode. The structure of the core/shell electrode generally adopts one of two designs: cascade or tunneling. The most common design, shown in

Scheme 5.1, uses a wide bandgap semiconductor interlayer that forces both the injection and recombination pathways to overcome a tunneling barrier.[72,73,77,186,187] This design exploits the kinetic redundancy of these systems, i.e. injection is several orders of magnitude faster than relaxation of the dye so that backward electron transfer can be significantly slowed while maintaining a high quantum efficiency for charge injection.[20]

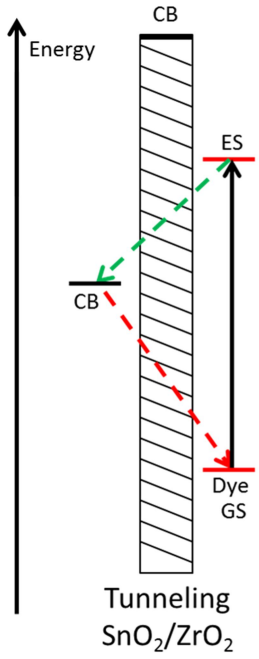

Scheme 5.1. Energy diagram for the tunneling electron transfer design. Favorable electron transfers are shown in green while recombination pathways are shown in red. Both injection and recombination face a tunneling barrier for electron transfer.

In order to gain a better understanding of the distance dependence of electron transfer within the context of WS-DSPECs, we present here a systematic study of the tunneling core/shell architecture. We characterize the ultrafast electron transfer from the excited state of the dye into the SnO_2 core as a function of the thickness of the insulating shell. We demonstrate that, contrary to expectations, ultrafast transport through the ZrO_2 is allowed in acidic solutions. The conduction band of ZrO_2 is too high in energy to accept an electron from the photoexcited dye, and time-resolved terahertz measurements do not resolve any feature that can be assigned to mobile electrons in the ZrO_2. Direct tunneling

through the shell is also slow relative to relaxation of the dye excited state for thicknesses greater than 0.5 nm. We suggest that the conduction observed in protonated ZrO_2 is related to trap assisted tunneling, a novel charge transport mechanism in dye sensitized systems.

5.2 Experimental

Bis(2,2′-bipyridine)(4,4′-diphosphonato-2,2′-bipyridine)ruthenium(II) bromide (Ru(II)phos) was prepared as previously described.[94]

5.2.1 Sample Preparation. SnO_2 pastes were prepared following the method of Ito et al.[136] Briefly, SnO_2 (Aldrich, 20-40 nm) was successively ground with acetic acid, water, and ethanol to give a suspension, which was ultrasonicated for 15 min. The suspension was allowed to sit for three hours to allow large aggregates to settle. After settling, α-terpineol was added with stirring, followed by an additional 10 min of ultrasonication. Finally, a 10 wt% solution of ethyl cellulose in ethanol was added with stirring, again followed by ultrasonication for 10 min. The ethanol was subsequently removed via rotary evaporation to give a paste.

Films were prepared doctor-blading on fused quartz substrates using Scotch Magic tape as a spacer layer. After each layer of paste was applied, the film was cured at 80 °C for 10 min before the next layer was applied. A total of three layers of paste were used for all samples, giving a final film thickness of 6 μm for SnO_2 and 5.4 μm for ZrO_2 after sintering. The films were sintered using the following program: 3 °C/min to 370 °C, hold for 10 min, 3 °C/min to 470 °C, hold for 30 min, cool to room temperature.

Core/Shell structures were fabricated using a Cambridge Savannah 200 atomic layer deposition (ALD) system. Samples were loaded into the deposition chamber and the chamber temperature was increased to the required temperature for the different materials followed by alternating pulses of water vapor and the respective metal oxide precursor. Due to the high surface area of the films, vapor pulses were held in the reaction chamber for 3 minutes followed by opening the valve and purging with N_2 for 25 seconds before the next pulse. Tetrakis(dimethylamido)zirconium was used as a precursor with a

deposition temperature of 200 °C and a precursor temperature of 75 °C. The pulse durations for this material were 0.015 s and 0.25 s for the water vapor and ZrO_2 precursor, respectively. These cycles were repeated for 1, 2, 5, 10, 20, and 40 iterations to make core/shell structures with varying thicknesses of shell material. Following shell deposition, all electrodes (including bare electrodes for comparability) were sintered a second time at 450 °C for 30 min before they were sensitized with dye. All films were sensitized in the dark from a 100 μM solution of Ru(II)phos in anhydrous ethanol for 16 hours, rinsed with ethanol, and dried under a stream of nitrogen.

Samples for TRTS spectroscopy were sealed using a second piece of fused quartz, with a 1 mm hole previously drilled into it, with a 60 μm Surlyn (Solaronix) spacer between the two pieces of quartz. The pieces of quartz were hot pressed to bond to the Surlyn and 0.1 M $HClO_4$ introduced via vacuum backfilling. Finally, the filling hole was covered with a small square of Surlyn, covered with a 1 cm^2 glass coverslip, and heat sealed using a soldering iron.

5.2.2 Instrumentation. Fluorescence spectroscopy was done on a SPEX Fluorolog 2 double grating fluorometer with at 450 W Xenon lamp. Electrodes for fluorescence were fabricated as above with varying thicknesses of the ZrO_2 shell on the mesoporous film of SnO_2. The instrument was operated in front facing mode with the metal oxide film tilted 45° from the excitation beam and facing nearly directly at the fluorescence detector. Emission was detected through a 1.5 mm slit width at a photomultiplier tube that had been normalized to the response sensitivity of the detector across the various wavelengths collected. Fluorescence was carried out in a N_2 degassed pH 1, 0.1 M $HClO_4$ aqueous solution. The electrodes were all excited at 460 nm and emission was collected from 510 – 800 nm with a step size of 1 nm and integration time of 1 s at each step. Experimental conditions were identical between samples in order to make emission intensity comparable across all measured electrodes.

Scanning/transmission electron microscopy (S/TEM) and energy dispersive X-ray spectroscopy (EDS) were carried out on an FEI Talos F200X S/TEM instrument.

X-ray photoelectron spectroscopy (XPS) was carried out on a PHI *VersaProbe* II Scanning XPS Microprobe.

Specific details for time-resolved terahertz spectroscopy (TRTS) are described in detail elsewhere.[21,135,137,138,140] In sum, the 35 fs pulse of an amplified Ti:sapphire laser (Spectra Physics, 800 nm, 1kHz repition) is split into three beams: pump, generation, and detection. The generation beam is used to generate THz radiation by frequency doubling to 400 nm, with both the fundamental and second harmonic focused in air to generate a plasma.[141,142] The forward propagating THz radiation generated by the plasma is collected and focused using off-axis paraboloidal mirrors, which is detected using free-space electro-optic sampling with a ZnTe(110) crystal.[143] Finally, the pump beam is frequency doubled to 400 nm and a variable neutral density filter used to adjust the power to 100 mW/cm^2 (6 mm diameter spot).

The TRTS scans were fit to the following function:

$$\Delta THz = \left\{ \Delta THz_0 + \sum_{i=1}^{n} A_i \left[\exp\left(-\frac{t - t_0}{\tau_i} \right) - 1 \right] \right\} \otimes G\left(FWHM \right) \tag{5.1}$$

where ΔTHz_o is the baseline before t=0, n is the number of exponentials included in the fit, t_0 corresponds to the injection time (i.e., t=0), A_i is the amplitude of a given component, τ_i is the lifetime of a given component, G(FWHM) is a Gaussian instrument response function (determined to be 0.5 ps) and $\otimes$ represents a convolution.

UV/Vis spectra were collected on a Cary 6000i UV-Vis-NIR spectrometer on dry films. The instrument was blanked to air and a zero light baseline was collected by blocking the beam. Spectra were collected from 800 to 200 nm, scanning at 10 nm/s with an interval of 1 nm.

5.2.3 Quantum Chemistry Calculations. The Ru(II)phos dye was investigated computationally with density functional theory (DFT), using the Gaussian09 package.[188] All calculations were performed with the B3LYP[189] density functional in presence of an SMD model polarizable continuum water solvent,[190] except where otherwise noted. The ground state S_0, singly oxidized state, and first triplet excited state T_1, were optimized with unrestricted DFT (uDFT) with the Def2SVP[191] basis set which employs an effective core potential for the ruthenium core electrons. The first excited singlet state S_1 was

optimized with linear-response time-dependent (TD) DFT with the Def2SVP basis set. At each of the four resulting geometries (optimized S_0, S_1, T_1, and Ox. geometries), single point energy calculations were performed for all electronic configurations, yielding 16 points on a potential energy surface (PES). The single point calculations were done with the Def2TZVP basis set except for S_1 where Def2SVP was used. The experimental oxidation potential was obtained from voltammetry measurements with the esterified form of Ru(II)phos in a CH_3CN solvent, so corresponding calculations in that solvent of the esterified form were performed on the Ru(II) and oxidized states, at the same level of theory. Calculated potentials vs NHE were obtained by assuming an NHE potential of 4.44 V vs vacuum.[192]

Electron injection from excited dye, through the ZrO_2 layer, into the SnO_2 was modelled in two ways: first as a tunneling process with the transmission coefficient T(E) calculated with the WKB approximation, where the ZrO_2 layer acts as a potential barrier with a given width d and constant height $|E-\xi|$:

$$T(E) = e^{-2\int_0^d \sqrt{2m|E-\xi(x)|/\hbar^2}dx} = e^{-2d\sqrt{2m|E-\xi|/\hbar^2}} \tag{5.2}$$

Here, m is the electron mass, and E and ξ are taken as the experimental CBM of ZrO_2 and the calculated T_1 state potential respectively.

The second injection mechanism considered is as a Marcus type electron transfer:

$$k_{ET} = \frac{2\pi|H_{AD}|^2}{\hbar\sqrt{4\pi\lambda_S k_b T}} \exp\left(-\frac{(\Delta G^0 + \lambda_S)^2}{4\lambda_S k_b T}\right) \tag{5.3}$$

Here H_{AD} is the electronic coupling matrix element between electron donor and acceptor, λ_S is the outer shell (solvent) reorganization energy, and ΔG^0 is the standard free energy change of the reaction. The standard free energy change is estimated from the calculated oxidation potential, the potential of the T_1 (or S_1) state and the experimental SnO_2 CBM edge:

$$\Delta G^0 = \mathrm{E_{ox}} - \mathrm{E}_{T_1} + \mathrm{E}_{CBM(\mathrm{Sn}_2)} \tag{5.4}$$

The outer shell reorganization energy λ_S is obtained as the difference between the total reorganization energy λ_T and the internal reorganization λ_V:

$$\lambda_{S,\mathrm{Hush}} = \lambda_{T,\mathrm{Hush}} - \lambda_V \tag{5.5}$$

The internal reorganization λ_V is the energy difference between the oxidized form in the T_1 (or S_1) geometry and the optimized oxidized geometry:

$$\lambda_V = E_{\mathrm{ox}}(\mathrm{opt}) - E_{\mathrm{ox}}(T_1\mathrm{geom}) \tag{5.6}$$

The total reorganization energy $\lambda_{T,\mathrm{Hush}}$ is also calculated using Equation 5.6, but instead of equilibrium solvation, the solvent shell from T_1 (or S_1) is used in the calculation of the second term in Equation 5.6. While $\lambda_{S,\mathrm{Hush}}$ assumes infinite separation between donor and acceptor so that both are fully surrounded by solvent molecules,[193] we made the approximation that due to surface binding, only half of the solute cavity is in contact with the solvent:

$$\lambda_S = \frac{\lambda_{S,\mathrm{Hush}}}{2} \tag{5.7}$$

5.3 Results and Discussion

5.3.1 Interfacial Electron Transfer with a ZrO_2 Shell. The ALD deposition of ZrO_2 was varied from 0 to 40 pulse cycles. The deposition rate for this precursor is commercially reported to be 1.02 Å per cycle at 200 °C on a Si wafer, which agrees well with our ellipsometric measurements on a wafer. A representative EDS map is shown in Figure 5.1 for a SnO_2/40pulse ZrO_2 sample, confirming the presence of a ZrO_2 shell on the nanoparticles. High-resolution TEM (Figure D.1) also confirms a nominal thickness of 40 Å of ZrO_2 with 40 pulses.

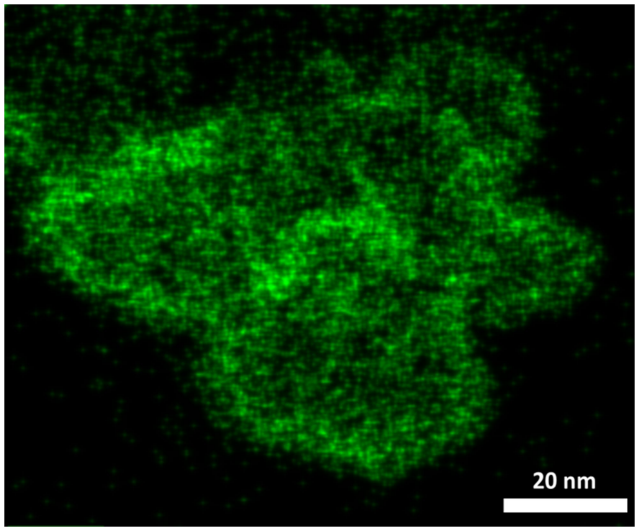

Figure 5.1. Representative EDS map image of 40 pulse cycles (~40 Å) of ZrO_2 coated on SnO_2 particles (collected after TRTS measurements). The green shell is surrounding SnO_2 particles in the image, exhibiting a uniform coating.

The peak emission for ZrO_2-coated SnO_2 is shown in Figure 5.2. Up to approximately 5 Å of ZrO_2, the emission is completely quenched, indicating efficient injection of the photoexcited electron. Once the shell thickness approaches 10-20 Å (10-20 pulse cycles), we begin to see an increase in the peak emission intensity. Surprisingly there still appears to be significant quenching of the excited state at 10 Å of ZrO_2 and even with 20 Å of ZrO_2 the emission is still below that observed at 40 Å. As we describe below, direct tunneling through even 5 Å of ZrO_2 would be too slow to compete with excited state decay due to the high-lying CBM. This suggests the existence of an unexpected additional pathway for electron injection through the ZrO_2 shell into the SnO_2.

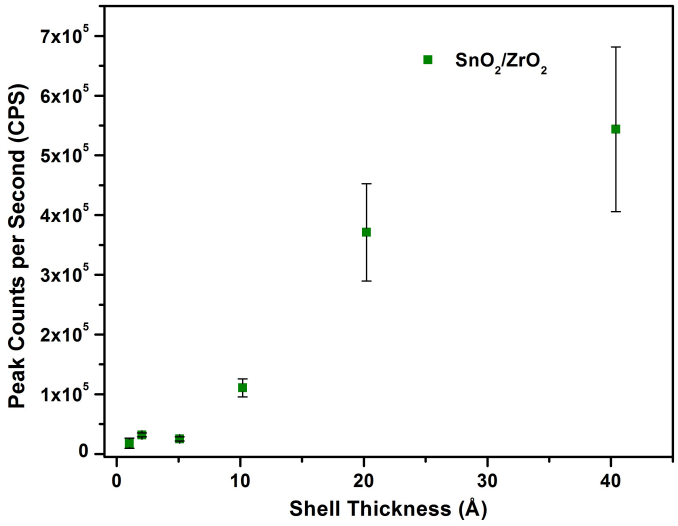

Figure 5.2. Peak emission measured between 510 and 800 nm from Ru(II)phos-sensitized core/shell films with varying thicknesses of the ZrO_2-shell on SnO_2. Emission was measured in N_2-purged, 0.1 M $HClO_4$ (pH 1) aqueous solution.

Because the CBM of ZrO_2 lies above the excited state of Ru(II)phos, tunneling through a thin shell should allow for electron injection while forcing the recombination to traverse a steep tunneling barrier. Figure 5.3 shows the TRTS traces (black) for sensitized SnO_2/ZrO_2, at different shell thicknesses. The injection components for all samples were fit using three exponential decays, overlaid in red in Figure 5.3, and fitting parameters are summarized in Table D.1. Similarly to the SnO_2/TiO_2 samples (Chapter 4), the 1-2 Å samples show an increase in injection amplitude relative to bare SnO_2, likely related to passivation of surface states, with injection decreasing from there with increasing shell thickness. Additionally, introduction of ZrO_2 suppresses long timescale trapping dynamics in the ALD-coated electrodes.

Unexpectedly, we observe significant injection amplitude even at 40 Å of ZrO_2. As we show below, this cannot be explained by electron tunneling. Even more strangely, in all cases the fast (~2 ps) and intermediate (15-20 ps) injection components remain nearly unaffected by film thicknesses. The ZrO_2 shell seems to mostly impact the slowest component, increasing the lifetime of that component by about a factor of 2. Commonly the short injection component in ruthenium-sensitized systems is attributed to injection from the singlet state of the dye and the longer components from the triplet state.[10,14,21,69]

This suggests that, whatever transport mechanism allows transfer through the ZrO_2 shell, the lower energy triplet state is more affected by the blocking layer.

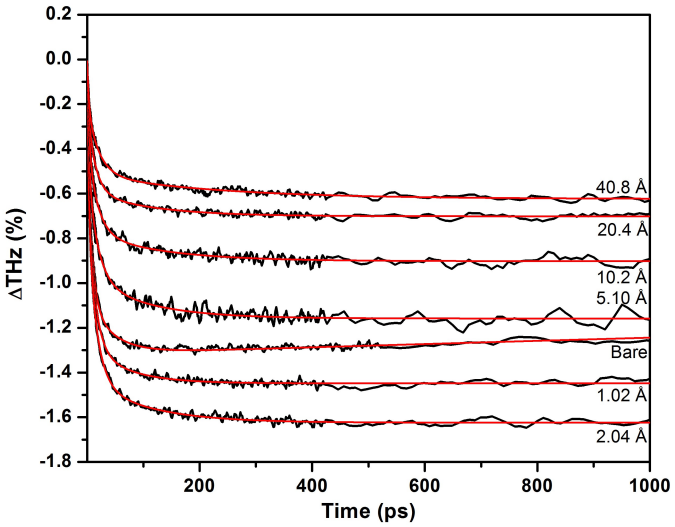

Figure 5.3. Time-resolved THz spectroscopy (TRTS) scans for SnO_2/ZrO_2 core/shell structures with increasing ZrO_2 shell thickness. TRTS scans were collected in a 0.1 M pH 1 $HClO_4$ aqueous solution.

Based on the estimated position of the pH 1 ZrO_2 CBM (~−1.35 V v. NHE, discussed below),[194,195] neither the singlet or triplet state is energetic enough to inject into its conduction band. We do not observe dye desorption and Figure 5.1 and Figure D.1 (Appendix D) clearly show that the ZrO_2 shell is intact and approximately 40 Å thick after the TRTS measurements, which eliminates the possibility of ZrO_2 dissolution and dye redeposition. ALD is well established as a conformal technique and at 40 pulses of Zr, pinholes are not expected and highly unlikely to be able to account for the significant injection amplitude.

5.3.2 XPS Characterization of SnO_2/ZrO_2 Films. In an effort to gain a better understanding of how the electron is moving through the ZrO_2 efficiently, XPS was carried out on SnO_2 samples coated with a 40 Å shell of ZrO_2. To identify what, if any, factor was affecting the ZrO_2 shell we looked at an as-prepared SnO_2/ZrO_2 film, a SnO_2/ZrO_2 film soaked overnight in anhydrous ethanol, and a SnO_2/ZrO_2 film soaked

overnight in 0.1 M $HClO_4$. We also looked at an uncoated, sintered SnO_2 film to help identify any changes in the SnO_2. Finally, as reference materials, we characterized the same commercial ZrO_2 and SnO_2 nanopowders used to prepare pastes. Survey scans showed the presence of C, O, Sn, and/or Zr. Importantly, no nitrogen was observed in the survey scans and this finding was confirmed with high-resolution scans of the N 1s region. This confirms that there is no nitrogen-doping of the ZrO_2 from the ALD precursor.

Figure 5.4 shows a high resolution scan of the Zr 3d region, while Figure D.2 includes high resolution scans of the C 1s (Figure D.2a), O 1s (Figure D.2b), and Sn 3d (Figure D.2c) regions. All of the XPS peaks were referenced to adventitious carbon at 284.4 eV (Figure D.2a). For the SnO_2 and ZrO_2 reference samples we observed only two peaks in the C 1s region related to adventitious carbon, while the four samples prepared from doctor-bladed pastes manifested an additional peak at 288.4 to 288.6 eV, suggesting that the sintering process fails to remove all the carbon from these films. Importantly, we do not observe any additional C 1s peaks for the SnO_2/ZrO_2 samples, which argues against any carbon-doping of the ZrO_2.

In the Zr 3d region (Figure 5.4), as expected we do not see any evidence of Zr in the SnO_2 reference and sintered SnO_2 samples. For the other samples, we clearly see the Zr $3d_{3/2}$ and Zr $3d_{5/2}$ peaks and in the ZrO_2 reference sample we see an additional feature at 186.9 eV. The feature at 186.9 eV is most probably related to surface suboxide species,[196] while on the basis of the 2.4 eV peak separation, the Zr $3d_{3/2}$ peaks at 184.1-184.5 and Zr $3d_{5/2}$ peaks at 181.6-182.1 relate to crystalline ZrO_2 species.[197] Figure D.3 demonstrates that the ZrO_2 reference sample is in the monoclinic phase, which is the most stable polymorph at room temperature.[198] It is clear from Figure 5.4 that the Zr 3d peaks for the ZrO_2 reference, as-prepared and ethanol treated SnO_2/ZrO_2 samples line up well at 184.4 and 182.0 eV, suggesting that the as-prepared ZrO_2 is monoclinic. From Figure 5.4 it is apparent that the Zr peaks in the $HClO_4$-treated sample are shifted to higher binding energies, 184.5 and 182.1 eV. It is unlikely that a phase change to cubic or tetragonal ZrO_2 has occurred as it has been observed that in the presence of strong acid and/or strain the tetragonal phase of ZrO_2 undergoes a spontaneous phase transformation to the monoclinic phase at room temperature.[199,200] Instead we assign this shift to the

incorporation of protons into the ZrO_2 shell. Chen et al.[201] observed a shift in the Nb 3d spectrum to higher binding energies upon hydrogen incorporation into Nb_2O_5, while electrochromic Nb_2O_5 films charged with Li^+ exhibit a shift to higher binding energies in the N 3d spectrum.[202] Bae et al.[203] have found that hydrogen impurities introduced during the ALD deposition of yttria-stablized zirconia results in a shift of the Y 3d peaks. This assignment is further supported by the O 1s spectra (Figure D.2b). The O 1s XPS spectrum for monoclinic ZrO_2 is composed to two components, bridging oxygen (530.1 eV) and -OH groups (~532 eV).[204] For the as-prepared and ethanol-treated SnO_2/ZrO_2 samples we find that the ratio –OH groups to bridging oxygen is about 0.52, while in the $HClO_4$-treated sample the ratio is 0.7. Introduction of protons into ZrO_2 is thought to induce the breaking of bridging oxygen to form ZrOH,[205] which is consistent with our results.

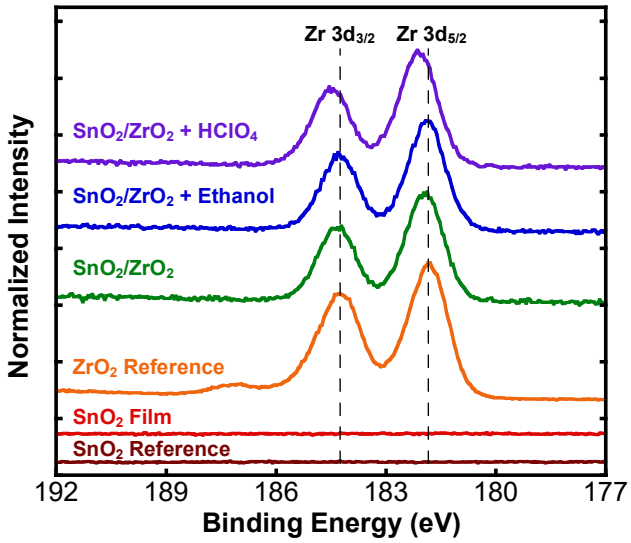

Figure 5.4. XPS spectra for commercial SnO_2 and ZrO_2 powders, an SnO_2 film made from the commercial powder, as prepared SnO_2/ZrO_2 (40 Å) film, and SnO_2/ZrO_2 (40 Å) films that had been exposed to either ethanol or 0.1 M $HClO_4$ overnight. All film samples were mechanically scraped up into a powder for analysis.

5.3.3 Mechanism of Charge Transport in ZrO2 Shells. The simplest model for the injection process from excited dye through the ZrO_2 shell to the TiO_2 core is a tunneling process. The efficiency of tunneling is described by the WKB approximation, Equation

5.2, depending only on the height and width of the potential barrier. The height can be estimated as the difference between the excited state (T_1 or S_1) potential of the dye and the ZrO_2 CBM. Although there is no general agreement on the bandgap and band potentials of ZrO_2, we take the bandgap of monoclinic ZrO_2 to be 5.4 eV.[206] Lyons et al.[194] calculate a valence band offset between monoclinic ZrO_2 and silicon of 3.5 eV. If we assume a valence band potential of 0.6 V v. NHE for silicon[195] then we infer that the CBM for monoclinic ZrO_2 lies at -1.35 V v. NHE at pH 1. The calculated, structurally relaxed T_1 and S_1 (HOMO-1, HOMO, LUMO, and LUMO+1 structures shown in Figure D.4) potentials are 1.71 and 2.10 eV above the ground state respectively, while without structural relaxation, the potentials are 1.88 and 2.25 eV respectively. The calculated ground state oxidation potential is 1.45 V vs NHE, as calculated in CH_3CN (the experimentally measured potential is 1.33 V v. NHE[1]). All these values differ from experiments by less than about 0.15 eV, although it is difficult to differentiate between the S_1 and T_1 experimentally. Based on these potentials, the barrier for tunneling through ZrO_2 can vary between 1.08 eV for the structurally relaxed T_1 and 0.55 for the non-relaxed S_1. As per Equation 5.2, this yields tunneling transmission probabilities vs ZrO_2 thickness as presented in Figure 5.5. This figure also includes the transmission for the experimental estimate of the barrier, as well as for a very small hypothetical barrier that would correspond to the high injection rate actually observed. This clearly demonstrates that for the potential energies observed, tunneling does not contribute significantly in any case except for the two thinnest ZrO_2 layers of < 2.04 Å.

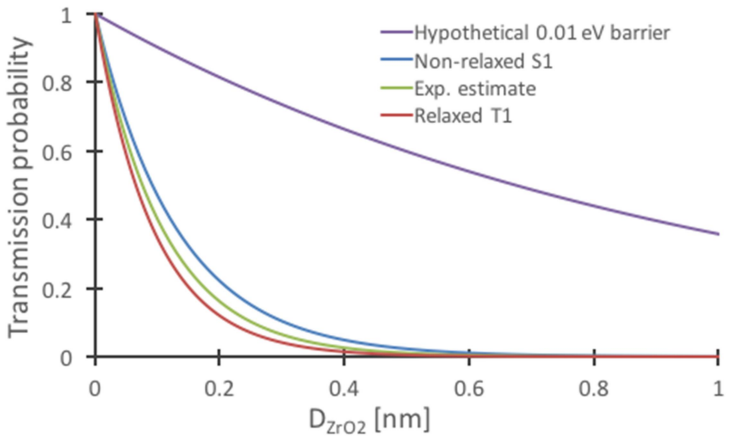

Figure 5.5. Tunneling probability according to the WKB approximation Equation 5.2, using a barrier height corresponding to the difference between the ZrO_2 CBM and the excited state potential. Also included is the largest hypothetical barrier that could account for the large injection observed through the ZrO_2.

The semiclassical Marcus theory of electron transfer (Equation 5.3) is commonly used to calculate transfer rates for weakly coupled electron donors and acceptors. Within this framework, electron transfer is a thermally activated process, where the surrounding solvent molecules must reorganize to accommodate the solute's change from reactant to product state. The free energy change ΔG^0 for the transfer from excited dye into SnO_2, estimated with Equation 5.4, ranges between -0.72 eV for the structurally relaxed T_1 and −1.26 eV for the non-relaxed S_1 state, based on an estimated SnO_2 CBM of 0.44 V vs NHE.[65] The outer-shell reorganization energy λ_S calculated with equations 5.5–7 amounts to 0.40 eV for the T_1 and 0.43 eV for the S_1 state. The fact that λ_S is smaller than $-\Delta G^0$ places the transfer reaction in the Marcus inverted region, where a larger driving force yields lower transfer rates.

The electronic coupling energy H_{AD} is not calculated quantum chemically, but can be estimated by inserting the rates from Figure 5.7 into the Marcus Equation 5.3. Without the ZrO_2 layer the rate is 6.0×10^{10} s^{-1} which results in an estimated coupling of 0.0036 eV for the T_1 state. The coupling is generally modeled as exponentially decaying with distance:[207–209]

$$H_{AD}^2 \propto e^{-\beta r} \qquad (5.8)$$

By fitting the distance-dependent rates of Figure 5.7 to Equation 5.8, we obtain a β of 0.026 $Å^{-1}$ for our injection process. We can also extract β by fitting $\ln[1/\langle\tau_w\rangle]$ versus shell thickness (Figure 5.6) and obtain an experimental value of 0.024 $Å^{-1}$. The barrier to tunneling (ΔE_{con}) can be estimated[210] from:

$$\beta = \frac{\sqrt{2m_e^*\Delta E_{con}}}{\hbar} \qquad (5.9)$$

where m_e* is the reduced mass of an electron in the conduction band. Taking m_e* as 0.3 then ΔE_{con} = 13 meV,[211] which is excellent agreement with the calculated tunneling barrier for the experimentally observed transmission. In comparison, the decay parameter β is around 1.0 $Å^{-1}$ for saturated hydrocarbons[212] and 0.6 $Å^{-1}$ for SnO_2/ZrO_2 in non-aqueous solvents.[76] A value of 0.024 $Å^{-1}$ represents a very slowly decaying coupling, even slower than the 0.04 $Å^{-1}$ typically seen for perfectly conjugated hydrocarbon chains.[212] The value of 0.024 $Å^{-1}$ represents very high conduction (β=0 for a metal) and similar to decay parameters observed for highly-doped semiconductors.[210] This remarkably low value for β suggests we either have a nearly metallic conducting shell or a mechanism other than direct tunneling exists. We discuss a suggested mechanism in more detail below. This result merits further experiments to verify its validity and conductivity measurements are underway to directly quantify the conduction through these Zr shells.

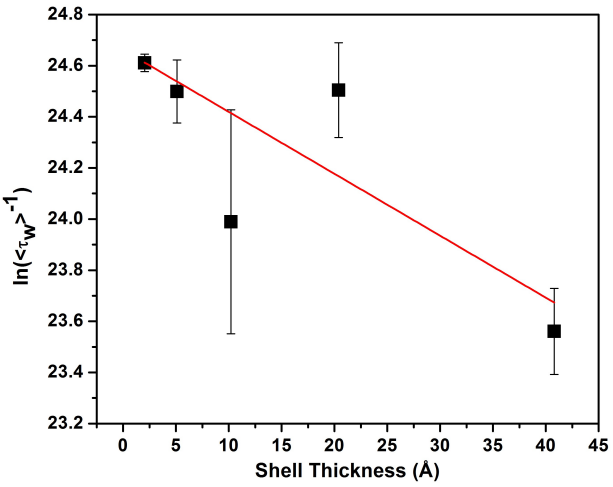

Figure 5.6. Plot of the natural log of the inverse of weighted electron injection time ($<\tau_w>$) versus ZrO_2 shell thickness. β is indicated by the slope of the line. $R^2 = 0.84$ for the fit.

Figure 5.7 summarizes the extracted weighted rate of electron transfer ($1/\tau_w$, Table D.1) and the scaling factor (listed in Table D.1) for each thickness of TiO_2 and ZrO_2. In order to facilitate simple comparison between traces, we use a weighted charge transfer rate that is a sum of each weight-adjusted lifetime component from the fits. The scaling factor is directly proportional to the number of injected electrons and thus is a measure of the injection efficiency. In the regime where tunneling is expected to be able to occur (1-2 Å), the rate of electron transfer decays rapidly with increasing thickness. As the shell thickness increases, we being see a leveling of the rate of injection, with rates remaining much faster for a ZrO_2 shell than similar TiO_2/SnO_2 systems that we have studied previously[21] and in Chapter 4. Interestingly, the scaling factor still shows strong dependence of shell thickness. Once tunneling becomes unlikely, the injection efficiency will depend on the difference in potential between the excited state of the dye and the acceptor state in the oxide shell. The similarity in the scaling factor between TiO_2 (ref 21 and Chapter 4) and ZrO_2 coated samples suggests that the important acceptor states in the respective shells lay at about the same potential, approximately -0.23 V v. NHE (the potential of the TiO_2 conduction band at pH 1). Despite the similarity in acceptor potential, the marked difference in the rate of injection clearly demonstrates that trap

assisted tunneling occurs more rapidly than the electron transfer cascade observed with SnO_2/TiO_2.

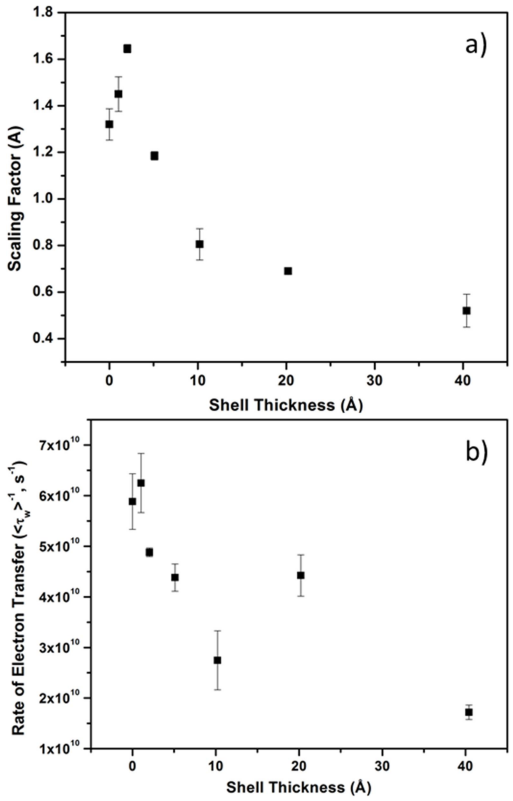

Figure 5.7. (a) Scaling factor and (b) weighted rate of electron transfer from fits to TRTS trace in Figure 5.3 for varying shell thicknesses.

Regardless of the mechanism of injection, the efficiency is expected to be exponentially decaying over distance. An important observation from Figure 5.7 can thus be made: neither the scaling factor nor the weighted electron transfer rate are well fitted to a single decaying exponential function, indicating that depending on the thickness, different processes are likely to be responsible for the injection dynamics observed. Förster resonance energy transfer is excluded as the dominant transfer mechanism through ZrO_2 due to the lack of spectral overlap between the emission of Ru(II)phos and absorption of SnO_2, as well as its very sharp r^{-6} decay with distance. The greater than 0.5 eV energy potential barrier prevents Ru(II)phos from injecting into the conduction band of monoclinic ZrO_2. Furthermore, as we demonstrated above, tunneling through the ZrO_2

is exceedingly unlikely. However, injection into surface states of bulk ZrO_2 has been observed in the literature. Verma et al.[103] and others[102,213–215] have shown that surface states in the ZrO_2 electrodes can act as acceptor states for excited dyes on the surface, effectively quenching the fluorescence yield. Verma et al. compared the emission of Os(bpy) complexes on colloidal TiO_2 and ZrO_2 and demonstrated that the emission of the dye on ZrO_2 was nearly 5 times less than in solution.[103]

Based on the XPS data and slowly decaying tunneling parameter, we suggest that charge transport is occurring via trap assisted tunneling, which to the best of our knowledge is the first demonstration of this mechanism in a dye-sensitized system and the first direct observation of electron transfer by this mechanism. Trap assisted tunneling has been observed in gate dielectrics and memory application, where high electric field strain introduces trap states in wide bandgap materials such as HfO_2 that facilitate electron transfer.[216–218] More specifically leakage currents in ZrO_2 in the low-electric field region (most analogous to our case) are attributed at least in part to trap assisted tunneling,[211] with traps in ZrO_2 thin films attributed to H^+.[205,219] In the case of sensitized SnO_2/ZrO_2, charge transport through the ZrO_2 must be occurring through non-mobile states as we do not observe any additional injection components, as we have for injection into TiO_2 shells (ref 21 and Chapters 2 and 4). This would be consistent with injection into localized trap states. Because we believe injection is occurring via trap state tunneling, the simple linear fit shown Figure 5.6 is insufficient to accurately describe the process and a more detailed discussion is underway.

To probe the importance of protons in promoting through-shell conduction, we examined the TRTS of a pair of Ru(II)phos-sensitized SnO_2/ZrO_2(40 Å) samples in 0.1 M $LiClO_4$ in acetonitrile. One sample was treated in 0.1 M $HClO_4$ (aq) overnight, while the other was left as-prepared. Figure 5.8 clearly demonstrates that the sample that was treated with acid shows significantly more injection amplitude than the as-prepared sample. The TRTS response for both samples was best described by a biexponential fit, with $<\tau>$ of 25.3 ps for the acid treated sample and 57.2 ps for the as-prepared sample. This largely explains the discrepancy between the results in this study and other examples of oxide core/ZrO_2 shell[73,76,77,220] structures. Significant conduction through a thick ZrO_2 is only allowed in the presence of protons. This is consistent with the results of those

studies, which showed that beyond a few angstroms of ZrO_2, charge injection was not observed, or was at least substantially decreased.

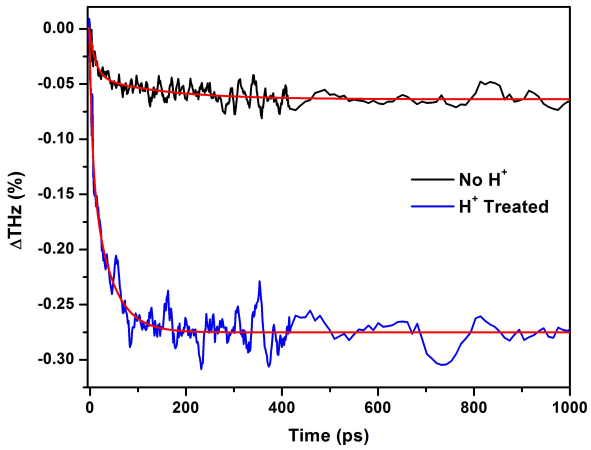

Figure 5.8. TRTS in 0.1 M $LiClO_4$ of Ru(II)phos-sensitized SnO_2/ZrO_2 (40 Å) treated with (H^+ treated) and without (No H^+) 0.1 M $HClO_4$. Red line shows a biexponential fit to equation 5.1.

5.4 Conclusions

Core/shell structures are used in WS-DSPECs in order to help maintain the charge-separated state by reducing recombination between the metal oxide support and oxidized dye on the surface. Using an insulating tunneling core/shell electrode design, we demonstrate that with very thin shells (<1-2 Å), we observe injection dynamics consistent with a tunneling barrier due to either the films being too thin to develop a full band structure or quantum confinement pushing the CBM higher in energy.

At insulating films sufficiently thick enough to completely block charge transfer in these systems, we observe injection kinetics and yields that dramatically conflict with theoretical tunneling calculations. Despite observing electrons within the SnO_2, there are no obvious signals for electrons within the ZrO_2 at any time. As a result, we believe that injection is occurring via trap-assisted tunneling whereby trap states are serving to transport electrons to the SnO_2 core. The formation of these trap states is likely a result of protonation during exposure to the experimental conditions. To the best of our knowledge, this is the first demonstration of trap assisted tunneling within the context of

WS-DSPECs. This should have a profound impact on future developments in utilizing structures that could rapidly facilitate charge injection while acting as a significant blocking layer for recombination.

Chapter 6

Monomeric Iridum Complex as a Precursor for an Active Water Splitting Catalyst and Adventitious Catalysis

Nicholas S. McCool,[1] Jacob A. Spies,[1] Geno Leone,[1] Thomas E. Mallouk[1-3]

[1]Department of Chemistry, [2]Department of Biology and Molecular Biology, and [3]Department of Physics, The Pennsylvania State University, University Park, PA 16802, United States

6.1 Introduction

Artificial photosynthesis aims to use water as a renewable feedstock of electrons and protons to make high purity hydrogen. Though interest in developing a photocathode has been growing, a great wealth of research has been done on the photoanode. Modeled after the conventional DSSC, WS-DSPECs utilize a metal oxide support sensitized with a molecular dye and water oxidation catalyst. Despite a modest thermodynamic barrier (1.23 V vs NHE at pH 0), the multi-atom, 4-electron water oxidation half reaction suffers from a steep kinetic barrier. As a result, developing an excellent catalyst has been the focus of a great deal of research in order to reduce the overpotential required to harvest protons and electrons from water.

In order for the catalyst to be active towards water splitting, a few criteria need to be met. The catalyst must be stable in water, in the specific operating pH of the device. Historically, this has resulted in systems being largely limited to basic medium or noble metals for catalysis.[221] The catalyst must also be stable to electrochemical cycling. This is typically accomplished by spreading the oxidation equivalents out across multiple atoms, whether through molecular species with multiple metal centers or strongly influencing ligands,[4,6,180] or by using bulk nanoparticles.[8,221] Though the molecular species yield more control over redox potentials, this generally comes at the cost of synthetic complexity. Though generally simple to synthesize and functionalize the surface, nanoparticles generally have a more fixed potential and suffer from inactive atoms within the core of the particle, limited by the surface area of the nanoparticle.

Recent work by Ahn et al. developed a monomeric Co catalyst that outperformed the bulk counterpart by roughly an order of magnitude.[222] They were also able to observe the way the catalytically active species evolved as a function of deposition conditions and found clearly distinct regions where different species persisted on the surface of the electrode. Work from our group has identified a monomeric Ir species that acts as a capping agent on iridium oxide ($IrOx \cdot nH_2O$ [IrOx]) nanoparticles and serves to stabilize the nanoparticle on the surface of an electrode.[223] We demonstrated that this monomeric species, likely a mixed Ir species of $[Ir(OH)_5(H_2O)]^{-2}$ and $[Ir(OH)_6]^{-2}$, was responsible, at these elevated concentrations, for the recombination pathway that effectively short

circuited these devices. We have also previously shown that the IrOx catalyst can act as a recombination pathway, scavenging electrons from the metal oxide support.[123] This is not entirely unexpected; a catalyst must be very strongly oxidizing in order to drive the water oxidation reaction and may be expected to indiscriminately take electrons from elsewhere (e.g. the metal oxide support).

As a result of our understanding the importance on concentration control in minimizing electron scavenging by the catalytically active species, herein we investigate the monomeric Ir species at low concentrations for water oxidation catalysis. Additionally, we discuss issues relating to adventitious catalysis and possible identities and their sources of the active species.

6.2 Experimental

6.2.1 WS-DSPEC Preparation. Bis(2,2'-bipyridine)(4,4'-diphosphonato-2,2'-bipyridine)-ruthenium bromide, [Ru(II)phos], was synthesized as previously reported.[94] TiO_2 paste was prepared via a modified procedure.[164] Briefly, glacial acetic acid (12g) was added to 58.6 g of rapidly stirring titanium isopropoxide (>97.0%, Sigma). The solution was allowed to stir for 15 min before being added all at once to 290 mL of water (18.2 MΩ). After 1 hour of stirring, nitric acid (4 mL) was added to the reaction mixture, which was then allowed to reflux for 75 min at 80 °C. The resulting solution was distributed in to 4x125 mL Parr bomb reactors (80 mL to each liner) and heated in Parr bomb reactions to 250 °C for 12 hours and allowed to cool to room temperature naturally. The resulting particles were sonicated using a horn sonicator and then the suspension was washed three times with ethanol to remove residual water. After the final wash step, the particles were then resuspended in a solution of 6 g ethyl cellulose (Sigma, 48-49.5% w/w ethoxyl basis) and 56 g terpineol (Sigma, 65% α-, 10% β-, 20% γ-mixture) in 300 mL of anhydrous ethanol and sonicated again. The suspension was allowed to settle for 1 hour to remove large aggregates. The ethanol was then stripped via rotary evaporation to leave the final translucent paste. The TiO_2 mesoporous films were prepared using the doctor blade method on fluorine-doped tin oxide (FTO)[123] with a microscope slide as the

straightedge and a single Scotch Magic tape spacer, films were cured at 120 °C for 5 min and then baked at 300 °C for 20 min, 350 °C for 10 min, and 500 °C for 30 min.

The Ir monomer was synthesized as previously reported.[223] Briefly, 4.8 mg (10 μmol) of K_2IrCl_6 (Sigma) was added to 100 mL of standardized 0.1 M NaOH (standardized by titrating with dry potassium hydrogen phthalate). The solution was placed in a water bath at 75 °C and allowed to heat to approximately 70 °C. The reaction was followed by UV/Vis (HP 8452A diode array spectrophotometer) to monitor the loss of the starting material and formation of the monomer. Once the solution reached 70 °C, the reaction was complete; the solution was immediately quenched in an ice bath and stored at 2 °C until used. Monomer was deposited on as-prepared TiO_2 films by submerging in various concentrations of monomer (diluted with 0.1 M NaOH) for 18 hours. Films were then sintered at 450 C for 3 hours, as done previously with citrate-capped IrOx nanoparticles, to anchor the monomer to the TiO_2 surface.

After monomer deposition, electrochemical contact to the FTO was accomplished using 28-gauge wires attached using silver paste. The silver contacts were covered with white epoxy for electrochemical and mechanical stability. These electrodes were sensitized by submerging in 100 uM Ru(II)phos in anhydrous ethanol for 16 hours. Samples were removed from dye solution, rinsed with ethanol, dried under a stream of N_2 and stored in the dark until use.

6.2.2 Chronoamperometry and ICP-MS Analysis. The buffer for photoelectrochemical testing was prepared using sodium phosphate monobasic (Sigma, ReagentPlus ≥99.0%) and dibasic (Sigma, ReagentPlus ≥99.0%). The 100 mM buffer was titrated to a final pH of 6.8 and used as needed. Chronoamperometry was carried out on an EZ-Stat potentiostat using a 300 W Xenon lamp passed through an AM1.5 filter, yielding an illumination intensity of 100 mW/cm^2. The light was also passed through a 410 nm long-pass filter to eliminate direct band-gap excitation of the TiO_2. Chronoamerometric experiments were carried out in a custom made H-cell configuration, where the cathode compartment (containing a Pt mesh) was separated from the anode compartment (containing the photoanode and a Ag/AgCl reference electrode) with a glass frit. Electrodes were biased at 100 mV vs. Ag/AgCl for measurements.

Samples for inductively coupled plasma mass spectroscopy (ICP-MS) were prepared as described above. TiO_2 films were exposed to varying steps in the fabrication and testing progress for testing; fresh as-prepared films, films that had contacts attached and films that had been used for water splitting experiments were all tested. The films were mechanically scraped up after exposure to varying steps along the fabrication process and digested overnight in a 12.5:1 v/v solution of concentrated nitric acid (Sigma, traceSELECT) and 40% hydrofluoric acid (Sigma, traceSELECT). Following digestion, an aliquot of the solutions were diluted to a final concentration of 2% HNO_3 using water (Sigma, traceSELECT). These final solutions were submitted for ICP-MS analysis at the Laboratory for Isotopes and Metals in the Environment at Penn State University using a Thermo Fisher Scientific X Series 2 ICP-MS instrument.

6.3 Results and Discussion

6.3.1 Photoelectrochemical Water Oxidation. Despite having a moderate thermodynamic redox potential, water oxidation requires the coordination of a 4-electron, many atom reaction which drives the kinetic requirements very high. As a result, the water oxidation catalyst must be electrochemically stable and be able to facilitate the mechanism of the reaction. This process has been demonstrated using IrOx nanoparticles to a great extent.[123,224–226] However, this also limits the available surface for catalysis. For a 2 nm particle, there are roughly 90 Ir atoms, most of which will be inactive within the core of the nanoparticle. By using a monomeric species, we will be able to expose all atoms to the reaction conditions.

In order to gain a better control over the synthesis of the monomer species, the reaction progress was followed by UV/Vis taken during the heating step and while maintaining the elevated temperature. Figure 6.1 shows the time-based UV/vis while tracking the synthesis as the solution is heated. The blue trace represents the starting material, K_2IrCl_6 in 0.1 M NaOH and the red trace is the final product once cooled. The loss of the starting material (400-500 nm) followed by a growth of an absorbance near 320 nm. The reaction was assumed to be completed when there was minimal growth in the peak near 320 with increasing duration. Allowing the reaction to proceed for too long

resulted in the formation of nanoparticles in solution, observed directly by the formation of a blue color.

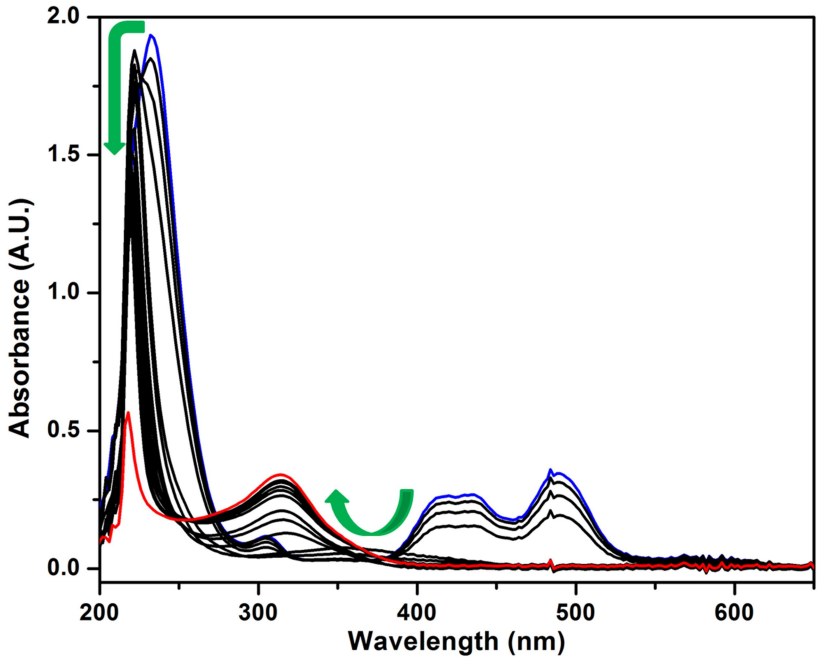

Figure 6.1. Time-based UV/Vis showing the evolution of monomer species by loss of starting material (400-500 nm region) and growth of peak indicative of the monomer (320 nm). Blue trace is the starting material (K_2IrCl_6 in 0.1 M NaOH) and red is the final product after cooling.

Once the monomer was synthesized, it was tested for its activity toward water oxidation. Figure 6.2 shows the peak catalytic activity of the monomer when measured in the photoanode device in 100 mM sodium phosphate buffer at pH 6.8 with a 100 mV vs. Ag/AgCl applied bias. At the lowest deposition solution concentrations of monomer examined, 50 nM, a local photocurrent maximum is observed. Upon depositing monomer from higher concentration solutions, the peak photocurrent drops before spiking back up again, and eventually does not spike upwards again. This trend is similar to that observed by Ahn et al,[222] where at very low concentrations of monomer at the surface, increasing the loading increased the surface coverage until a transition occurred in the active species, indicated by a sharp drop it activity. Further increase in deposited material saw increased photocurrent as a result, again, of increased surface coverage until reaching another sharp drop. Beyond a certain concentration, we anticipate seeing an overall drop

due to the catalyst scavenging electrons from the TiO_2, as we've observed in previous work.[123]

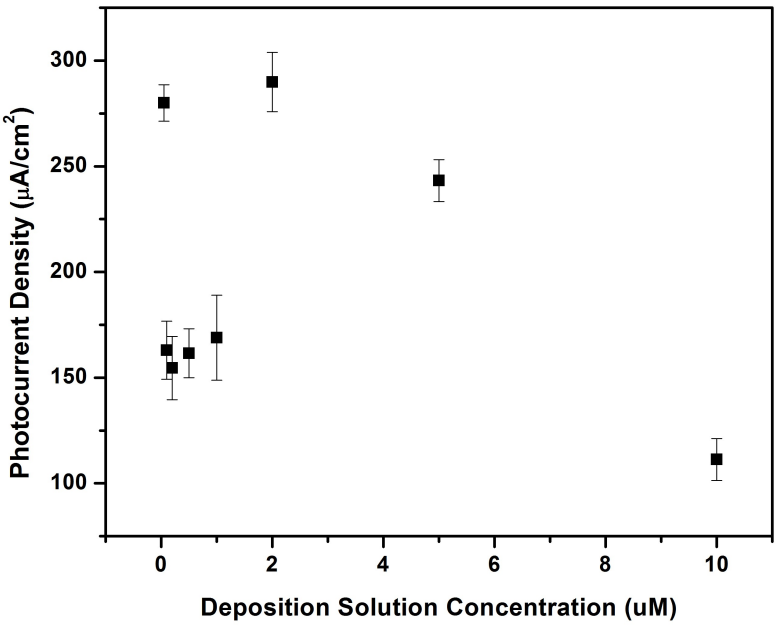

Figure 6.2. Peak photocurrent values for water oxidation experiments carried out in 100 mM pH 6.8 sodium phosphate buffer with an external bias of 100 mV vs. Ag/AgCl with varying concentrations of monomer deposited.

Unfortunately, at the same time as the work discussed above, we discovered that these electrodes were splitting water remarkably well without the intentional addition of a catalyst. (See Chapter 3 and Appendix B for demonstration of activity). The activity of this adventitious water splitting catalyst rivals that of IrOx and is likely responsible for a fraction of the current observed in the monomer experiments discussed above. Despite meeting the thermodynamic potential for water oxidation, Ru(II)phos does not possess the ability to oxidize water due to the kinetic limitations. We therefore anticipate that the source of the catalytic activity is an impurity from a step in the paste synthesis, device fabrication, or testing process.

6.3.2 Adventitious Catalysis. Recent work by Fielden et al. has shown a similar phenomenon, whereby the addition of a catalyst improves the photocurrent in the system but they still observe a large background current without the intentional addition of a

catalyst.[132] The activity of the catalyst-free electrodes is demonstrated using similar Clark-type measurements as those discussed in Appendix B to quantify the oxygen produced at the electrode surface. Several other groups have additionally observed adventitious electrocatalysis of water due to Ni impurities in reagents[165] or trace Fe leeched from glassware.[166] In fact, Roger et al. showed that Ni, in concentrations as low as 17 nM, could act as a water oxidation catalyst. The efficiency of Ni in solution to leech Fe from glassware, making a stable and very active nickel iron oxyhydroxide catalyst *in situ*, is so high that the authors even use $Ni(OH)_2$ to absorb Fe impurities as an initial cleaning step for their glassware.[166]

In order to determine the identity of the adventitious catalyst in our system, we utilized ICP-MS and, in an attempt to identify the source, we analyzed films at different points along the fabrication and testing process. Table 6.1 shows the different elements that we tested the films for, selecting several different metals commonly used for water oxidation as well as possible contaminants from glassware or reagents. For most elements sought, the samples containing digested TiO_2 films were not dramatically different from the blank digestion solution that contained no film. Interestingly, however, the sample that contained TiO_2 that had been exposed to water oxidation experimental conditions showed nearly ten times the amount of Ni present. Additionally, a decrease in Fe present might suggest a dissolution of Fe contained in the film with some redepositing as a NiFe catalyst. Unfortunately, some issues with the blank values for Fe suggest that the experiment should be reproduced with more care taken in digesting the samples and ensuring the vessels that the samples are digested and stored in are appropriately cleaned with the traceSELECT solvents.

Table 6.1. Summary of ICP-MS analysis on digested TiO_2 electrodes exposed to different steps in the device fabrication and testing process.

Element	**Mn**	**Fe**	**Co**	**Ni**	**Cu**	**Mo**	**Ru**	**Rh**	**Sn**	**Ir**	**Pb**
units	ppb	ppb	ppb	ppb	ppb	ppb	ppb	ppb	ppb	ppb	ppb
Blank	0.024	1.79	0.008	0.026	0.08	1.34	0.013	0.008	3.41	0.017	0.024
TiO_2 No Wires	n/d	1.28	0.012	0.044	0.20	1.23	n/d	0.008	2.11	0.014	0.014
TiO_2 w/ Wires	n/d	0.62	n/d	0.034	0.16	n/d	n/d	0.006	2.31	0.012	0.010
TiO_2 Photolysis	n/d	0.45	0.008	0.248	0.15	n/d	0.014	0.004	1.78	0.012	0.012

The difficulty with these impurities is that catalysis requires very little of the material to be effective. Our recently reported work using a citrate-capped IrOx catalyst used nuclear absorption activation to quantify the amount of Ir present on the electrodes.[123] We found that we were depositing single picomoles per square centimeter of surface area. As a result, this work in particular stresses the importance of control samples and the sensitivity of this field to ultra-trace levels of contamination.

6.4 Conclusions and Future Outlook

Despite the presence of a catalytically active impurity, the Ir monomer shows some effect on the performance of these WS-DSPECs. The chronoamperometric work also suggests that probing both lower and higher concentrations of monomer should help extend the picture of what active species exists on the electrode surface.

Further work can be done on understanding the source and identity of the catalyst, and is under way in our lab. If reagents are the source of the impurity, traceSELECT reagents should be used in order to minimize the impurity and glassware may need to be cleaned using a particular process in order to eliminate the source of contamination. Because it is a surface-sensitive technique, XPS may yield information about the active species. EDS may also be useful in identifying the catalyst if the loading is high. Although the species in unknown, this work demonstrates the fragility of the field and the importance of periodically checking blanks to ensure that they are behaving expectedly.

Chapter 7

Conclusions and Future Work

WS-DSPECs offer a promising opportunity to generate pure hydrogen and oxygen from solar radiation. The modular nature of the system can allow for individualized optimization and tuning and can be operated with a wealth of different components. The growing availability of stable catalysts dye molecules that are either metal-free or derived from earth abundant metals continues to drive down the costs of these devices while increasing their flexibility. Additionally, high tunability of the dye offers the capability to target specific wavelength ranges for absorption to drive either half reaction. However, despite a growing field of research, power conversion for these devices remains low due, in particular, to a very high recombination between photogenerated electrons in the metal oxide support and holes on the dye molecules.

In Chapter 1, we laid the groundwork for understanding the relationship between the various electron transfer pathways and discuss their strong dependence on each other. By drawing connections between charge mobility and recombination, we follow research in developing core/shell structures designed specifically to target recombination and find that energy-cascade architectures offer the capability to drive directional electron injection based on the shell thickness. The flaw, however, in these structures is that they rely on core oxides with an insufficiently energetic CBM to drive water reduction. As a result, these architectures remain tailored toward the eventual design of the 2-photon-1-electron "Z-scheme" process used in nature whereby two photons drive the overall water splitting reaction, one at each electrode driving that specific half reaction. In addition, we discuss the pivotal role the dye anchoring group plays in not only dye stability, but in facilitating directional charge injection without also increasing the rate of recombination.

In moving toward a core/shell structure, Chapter 2 focused on understanding the effect of the shell on injection dynamics. A great deal of research has been done on core/shell structures in the context of DSSCs, but for WS-DSPECs this is a rapidly developing field. We studied four of the most common electrode designs, namely bare TiO_2 and SnO_2, as well as TiO_2/Al_2O_3 and SnO_2/TiO_2 core/shell structures. Interestingly, we found that in general, the arrival of an electron in the CB of a material was slower than comparable transient absorbance measurements studying the oxidation of the dye upon electron injection. This suggests that electrons are injected in to non-mobile surface states before release in to the conduction band and indicates the importance of surface

structure for these electrodes. Additionally, we observe injection into the shell material, followed by trapping within the shell before eventual release into the core oxide.

By nature of working in protic solvents, understanding the role of protons on device performance is very important. In Chapter 3, we revisited earlier work[38] that studied the effect of dye deposition solvent in order to identify the role of protons in causing poor device performance. We found that protons likely cause both surface and bulk trap states in the TiO_2 electrode. The surface states can act as acceptor states for charge injection or can act as bulk trapping sites. The electrostatic nature of these trap states result in very long-lived trapping events (up to tens of milliseconds) which we show increases the rate of trapping and recombination when compared to electrodes not exposed to perchloric acid. Though the nature of the trap states is not entirely clear, we hypothesize that it may be related to structural distortion at the surface, stabilized by protons saturating dangling bonds.

In Chapter 4 we revisited the SnO_2/TiO_2 energy-cascade core/shell structure studied in Chapter 2 in an effort to develop a more clear understanding of the injection pathway in these structures. By varying the shell thickness, we observe two distinct injection pathways. Initially (<5 Å), charge injection occurs via tunneling through the shell, likely either a result of a poorly developed band structure or quantum confinement effects pushing the CBM of TiO_2 too negative in energy to efficiently quench the excited state of the dye. Beyond this thickness, we see an evolving injection feature consistent with growing injection directly in to the shell, followed by trapping within the shell before eventual release into the core oxide. Additionally, the degree of trapping in the shell increases with shell thickness, stressing the need to optimize the shell to control recombination without hindering charge diffusion.

Chapter 5 continued to expand on the core/shell work by studying injection through an insulating, wide band gap semiconductor. SnO_2/ZrO_2 core shell structures should result in a tunneling barrier than hinders both charge injection and recombination. Emission studies support this hypothesis. However, TRTS clearly shows injection yields and rates that dramatically clash with theoretical calculations assuming a tunneling barrier. We find that exposure of these core/shell electrodes to acid induces the observed injection pathway. We hypothesize that the protons are inducing trap states that are

facilitating injection through the shell via the first demonstrated trap-assisted tunneling observed in dye cell literature. By comparing the injection rates and yields to that of the SnO_2/TiO_2 structure discussed in Chapters 2 and 4, we believe that the trap states are similar in energy to the mobile TiO_2 states (the CBM) which is likely why this has never been observed in TiO_2/ZrO_2 structures which may simply lack the driving force for charge transfer. This work can have profound effects in multiple areas of research beyond simply WS-DSPECs and further demonstrates the importance of proton control expressed in Chapter 3.

Finally, Chapter 6 discussed the attempt at designing a novel water-splitting catalyst. Catalysts are generally limited by their surface area, representing the active area in which catalysis can occur. By developing a single site catalyst, we should be able to make use of all the atoms rather than just surface atoms in the catalytic nanoparticle. However, this work was limited by the discovery of an advantageous catalyst. Without the intentional addition of a catalyst, we still observed very high catalytic activity. We are currently in the process of trying to identify the impurity and believe it might be similar to other reports in literature on adventitious nickel and iron coming from reagent impurities and glassware, respectively.

In this dissertation, we studied electron injection rates in model systems as well as systems derived to control the back electron transfer pathway. Similarly, we focused on recombination from a stand point of the metal oxide, working to understand the role of trapping and protons in both the injection and recombination rates, as well as their effect on overall device performance. Developing a detailed picture of how each of these components dictate performance is critical in designing future device architectures and this work has contributed fundamental knowledge in describing this picture.

Because this dissertation has largely focused on the mechanisms that negatively impact WS-DSPECs, it inevitably brings to light new questions, but ultimately opens various possibilities for improving the device performance. One clear discrepancy observed in this work relates the trapping dynamics observed in the SnO_2/TiO_2 core/shell structures compared to the bare TiO_2 structures. With the bare structure, we do not observe any trapping within the timescales measured in this dissertation (~1 ns) unless exposed to protic solvents. However, in the core/shell structure, ultrafast trapping occurs

within 1-2 ps. Because the energetics are sensitive to the crystal structure, demonstrated by the difference in band structures for rutile and anatase TiO_2, and trap states are commonly related to open coordination sites on the metal center, it is likely that the band structure and trapping dynamics in amorphous TiO_2 will be dramatically different than those observed for bulk nanoparticles. Recent work by Xu et al. in our group studied the band structure for monolayer sheets.[227] A similar set of experiments could be done on ultrathin TiO_2 films deposited on planar electrodes to observe how the band structure and flat-band potential change with increasing thickness towards a crystalline film.

Another interesting, and possibly conflicting, result in this work revolves around the nature of these proton-induced trap states. In Chapter 3, we argue that the electrostatic nature of these trap states results in a dramatically increased trapping time, from 1-10 ns for intrinsic trap states in the film compared to 1-10 ms for proton-induced trap states. Despite this, we observe electrons moving through the ZrO_2 shell in Chapter 5 as a result of exposure to acid. As a result, it is not completely clear yet what role the protons are playing in allowing electrons to drive through what should be a tunneling barrier. One possibility is that the protons interact with ZrO_2 differently than TiO_2 because of either intrinsic differences in the oxide or related to the crystalline nature of the TiO_2 compared to the ZrO_2 shell. This is not entirely unexpected as the protons have been shown to stabilize the distorted lattice and might be expected to interact differently based on crystal structure. This observation could also be suggesting a difference between the surface and bulk trap states.

An interesting possibility to probe these trap states might be to systematically study the exposure to protic solvents. Though intercalation has been observed in TiO_2 with very low proton concentration as discussed in Chapter 3, controlling both exposure time and concentration of protons should be expected to reach a trap threshold where transport can occur; below this thickness the trap states will be too far apart to facilitate charge transfer. This would more definitively show that these trap states are responsible for conduction through the insulating shell.

Because we have not gotten to a region of Zr shell thickness where the rate of electron transfer has leveled off, developing a support structure that would allow the analysis of thicker Zr shells would likely yield more information about the nature of these

proton states and how they are carrying electrons through the shell. As the shell gets too thick, it is possible that the protons are not able to sufficiently form bulk trap states to drive the charge transport, but below that thickness, varying shell thickness at thicker films should yield more dramatic effects in controlling the exposure to protons discussed above.

Ultimately, the final goal is clearly to make a long-term functioning device. Devices utilizing any of the discussed core/shell structures in this dissertation should yield valuable information in relating the parameters discussed here, such as injection, trapping and recombination dynamics, to the overall device performance. As discussed in Chapters 2 and 4, SnO_2/TiO_2 structures have been used to fabricate devices, however this work and others have shown the importance of fine control over the shell thickness. Coupling the clear importance of thickness on trapping dynamics in the shell to device performance will strengthen the argument of an optimal thickness to maximize the efficiency of charge separation.

A great deal of work has been done in DSSC literature on TiO_2/ZrO_2 structures, however little work in either DSSCs or WS-DSPECs has been done on SnO_2/ZrO_2 architectures. Additionally, the work in Chapter 5 demonstrates that there are unique opportunities within the context of the WS-DSPEC to utilize ZrO_2 shells. Two of the most obvious issues with these devices is dye stability on the surface of the metal oxide and recombination. The ZrO_2 shell can help address both of these concerns. Phosphonate group binding more strongly to the ZrO_2 surface compared to TiO_2, as discussed in Chapter 1. Most interestingly, however, is the possibility of the ZrO_2 shell to act as a rectifier. It is highly likely that the trap states facilitating charge transport through the insulating shell lie sufficiently above the SnO_2 CBM to maintain the driving force to move electrons. As a result, the recombination pathway should still face a very steep tunneling barrier and should substantially increase the lifetime of electrons within the core which should have a marked effect on device performance.

One complication of building devices using these core/shell structures however will be the adventitious catalyst. If the source of the catalyst is from the TiO_2 paste itself, then the shell structure might block the active catalyst and limit the comparability between uncoated and coated devices on their ability to oxidize water. Even if the source is the

external system (buffer, water, glassware, etc.), the catalyst may interact differently with the different oxide surfaces which may make comparability difficult. Since these core/shell structures will represent a large part of driving this project forward, it seems that the most important aspect to focus on initially is this adventitious catalyst. However, at least initially, eliminating this catalyst will be more important than necessarily identifying it in order to allow for the WS-DSPEC project to proceed in making devices using the core/shell structure. As discussed briefly in Chapter 3 and in more detail in the references within, the source of the catalyst is likely either an impurity in reagents or coming from the glassware. As a result, the first step in moving forward will be to eliminate all glass and metal in synthesis and device fabrication, including moving towards a plastic or Teflon H-cell design. Removing the adventitious catalyst and returning to the directly sintered cit-capped IrOx in core/shell SnO_2/ZrO_2 will likely be the most fruitful direction for the WS-DSPEC.

These core/shell structures (coupled with possible work on dye binding group discussed in Chapter 1) may allow the devices to operate in more basic solutions. Earlier work by this group suggests that using a pH gradient, with the anode in basic solution and cathode in acid, would likely be the best way to operate these devices to avoid the pH gradient losses formed when operated in buffered solution at neutral pH.[228] The CBM of TiO_2 however is too negative to quench the excited state of the dye in even mildly basic solution; even at neutral pH the injection yield drops to 20% compared to unity at pH 1. Because the CBM of SnO_2 is several hundred mV below TiO_2, the dye can still inject into the oxide in basic solution. Dye stability however will still be an issue as the phosphonate group is not stable on the surface in base. The alumina mummy strategy discussed in Chapter 3 showed marked improvement in stability of the dye on the oxide surface; it is possible therefore that a mummy strategy will allow for these devices to operate in base. An added benefit of working in base is that the water oxidation half reaction requires a much lower oxidative potential, which would allow for redder dyes to be used to take advantage of a wider region of the solar spectrum.

Though most of this dissertation focused on the interaction between the dye and the oxide support, previous work on the monomer discussed in Chapter 6 suggested that an underlayer serves the purpose of blocking the monomer from short circuiting the device

at the FTO/TiO_2/solution interface. Generally, this underlayer is a dense 80-100 nm TiO_2 film that protects the FTO substrate from I_3^- in solution which can scavenge electrons from the FTO. However, in the case of the monomer, it is expected that the monomer should bind very strongly to the TiO_2 and it is unlikely that a large quantity is interacting with the FTO as might be expected if the species is dissolved in solution as it is in DSSC literature. We therefore believe that the underlayer does not necessarily only serve to protect the FTO but also improves efficient charge transfer from the TiO_2 to the FTO. Directly quantifying this process should be possible through impedance or intensity modulated photocurrent spectroscopy. This could dramatically increase the understanding in how these materials improve device performance and drive other research in these and similar devices forward.

Appendix A

Supporting Information for Chapter 2

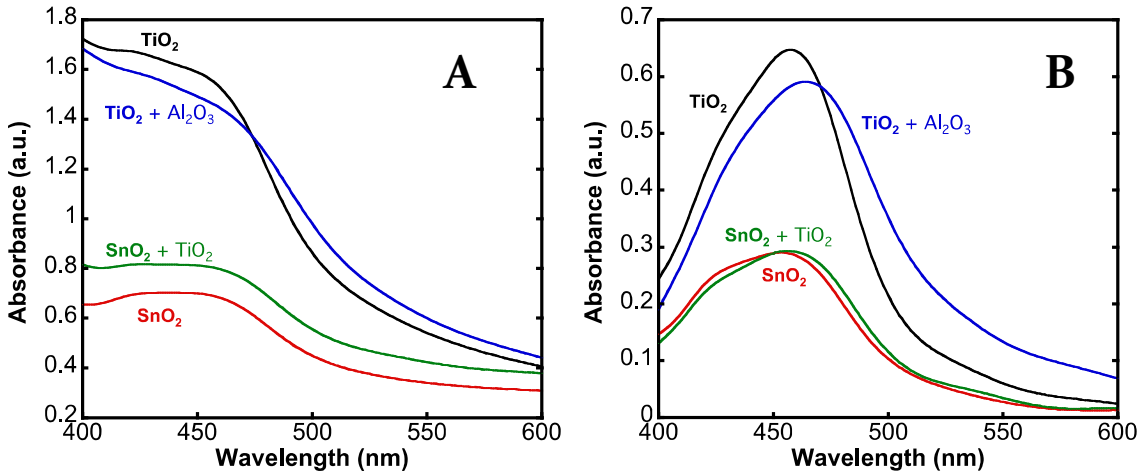

Figure A.1. Raw (A) and scatter-corrected (B) steady-state UV-Vis spectra of sensitized films: TiO_2 [Ru(II)phos-TiO_2], TiO_2 + Al_2O_3 [Al_2O_3-Ru(II)phos-TiO_2], SnO_2 [Ru(II)phos-SnO_2], and SnO_2 + TiO_2 [Ru(II)phos-SnO_2/TiO_2]. Spectra corrected for scattering by subtracting the spectra of the unsensitized films.

Appendix B

Supporting Information for Chapter 3

Electrochemical detection of oxygen. Photoelectrochemical water-splitting has been demonstrated in dye-sensitized cells using a variety of colloidal and molecular water oxidation catalysts. Interestingly, Fielden et al. have recently observed water-splitting in a similar system without the deliberate addition of a catalyst.[132] Herein, we also verify oxygen evolution without a deliberately added catalyst by using a Clark-type electrode configuration.[3,26,122,132] Amperometric detection of oxygen was carried out using a Pine Instruments bipotentiostat (Model AFCBP1). Pt electrodes were made by sputtering 10 nm of Ti on FTO glass (Hartford Glass) followed by 200 nm of Pt. Electrical contact was made to the Pt electrodes using a copper wire and silver paste which was then protected using (Loctite Hysol 1C) white epoxy. Approximately 1 μm of additional Pt was electrochemically plated onto the electrodes at 2.5 mA/cm^2 for 20 minutes. Prior to each experiment, the Pt electrodes were electrochemically polished to ensure a clean working surface and the collection efficiency was recalibrated. To calibrate the system, a Pt working electrode was masked to 1 cm^2 using Kapton tape to match the working area of a typical photoanode. A second Pt electrode was sandwiched with the first using a 1 mm thick microscope slide as a spacer and held together using Parafilm. The electrodes were placed in the anode compartment of an H-cell filled with 0.1 M phosphate buffer at pH 6.8 and purged with nitrogen. Using the bipotentiostat, the collector electrode was biased at -640 mV vs. Ag/AgCl and allowed to reach baseline. Once stabilized, the generator was biased at 1200 mV vs Ag/AgCl to oxidize water while the collector reduced locally generated oxygen. After several minutes, the generator electrode was disconnected and the collector returned to baseline. A linear fit between before and after electrolysis was used to approximate the baseline at a given time point for the collector current. When baseline-corrected, the ratio of collected current to generator current yielded the collection efficiency for this configuration. The two electrodes were separated and the Pt generator was replaced with a photoanode. The photoanode was biased at 100 mV vs Ag/AgCl and both electrodes were allowed to stabilize before being illuminated. The

collection efficiency for the experiment was then obtained from the ratio of generator and collector currents using the calibrated collection efficiency.

Two Pt electrodes were used before each collector experiment to calibrate the collection efficiency of the system. The top panel in Figure B.1 shows a collection calibration in which the generator electrode was connected at a 1200 mV vs Ag/AgCl bias at 0 s. The calibration was taken at 60 s in order to ensure that there was no non-Faradaic or other transient contribution to the current. These measurements typically resulted in a collection efficiency between 75 and 85%. The Pt electrode was replaced with a standard photoanode, Ru-EtOH, in order to determine the faradaic efficiency for the production of oxygen by water oxidation. The bottom panel in Figure B.1 shows a collector experiment using either a Pt or an FTO collector electrode. When corrected for the background current at the collector, we found that the electrodes produced oxygen with a 97.8 ± 4.7% (n = 3 samples) faradaic efficiency. The efficiency remains constant within experimental error when other time points along the photoelectrolysis trace were used. An FTO electrode is included in order to rule out the production of hydrogen peroxide. At the cathodic potentials used, Pt should reduce both oxygen and hydrogen peroxide, but the FTO electrode is only sensitive to hydrogen peroxide. The lack of a current response at the FTO collector demonstrates that the photoanodes generate oxygen at unit current efficiency despite the lack of a deliberately added catalyst.

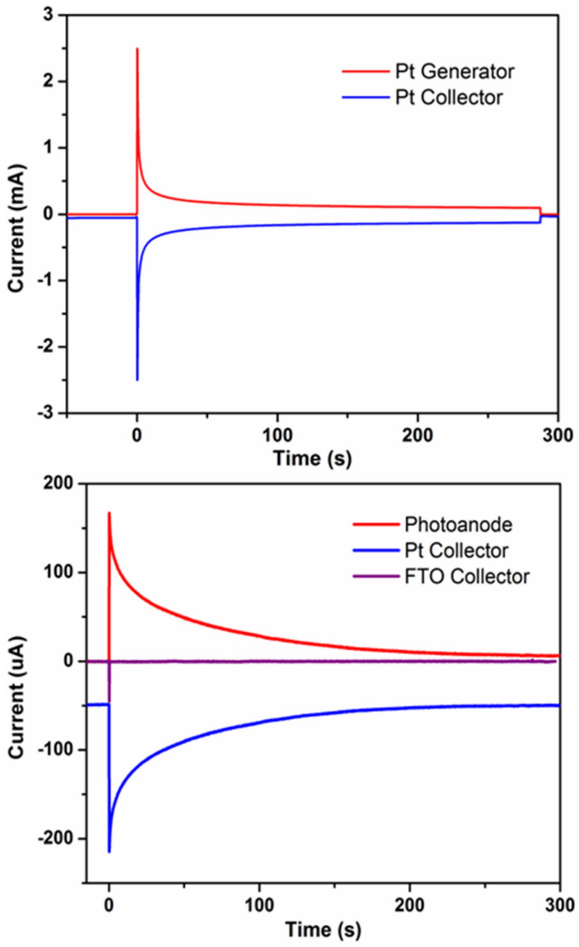

Figure B.1. Clark-type measurement for photoanodes prepared with dye from ethanol in pH 6.8 0.1 M sodium phosphate buffer. (Top) Calibration using two Pt electrodes biased at 1200 mV and -640 mV vs. Ag/AgCl as the generator and collector, respectively. The generator electrode was connected at 0 s. (Bottom) Collection experiment using a Ru-EtOH photoanode biased at 100 mV vs Ag/AgCl and a Pt collector or bare FTO electrode collector biased at -640 mV vs. Ag/AgCl, with light on at 0s.

Table B.1. Fitting parameters for TRTS traces in Figure 3.4

	A_1[a]	τ_1 (ps)	A_2[a]	τ_2 (ps)	A_3[a]	τ_3 (ps)	A_4[a]	τ_4 (ps)
Ru-EtOH	0.46	<0.5	0.33	19.1	0.21	231.1		
Ru-$HClO_4$	0.20	0.8	0.80	460.1	-1.13	2348		
Ru-$HClO_4$-HV	0.19	<0.5	0.19	16.5	0.62	402.3	-0.94	1960.6

[a] A_1, A_2, A_3, and A_4 are normalized amplitudes

Appendix C
Supporting Information for Chapter 4

Experimental

Bis(2,2′-bipyridine)(4,4′-diphosphonato-2,2′-bipyridine)ruthenium(II) bromide (Ru(II)phos) was prepared as previously described.[94]

Sample Preparation. SnO_2 pastes were prepared following the method of Ito et al.[136] Briefly, SnO_2 (Aldrich, 20-40 nm) was successively ground with acetic acid, water, and ethanol to give a suspension, which was ultrasonicated for 15 min. The suspension was allowed to sit for three hours to allow large aggregates to settle. After settling, α-terpineol was added with stirring, followed by an additional 10 min of ultrasonication. Finally, a 10 wt% solution of ethyl cellulose in ethanol was added with stirring, again followed by ultrasonication for 10 min. The ethanol was subsequently removed via rotary evaporation to give a paste.

Films were prepared doctor-blading on fused quartz substrates (GM Associates, Inc.) using Scotch Magic tape as a spacer layer. After each layer of paste was applied, the film was cured at 80 °C for 10 min before the next layer was applied. A total of three layers of paste were used for all samples, giving a final film thickness of 6 μm after sintering. The films were sintered using the following program: 3 °C/min to 370 °C, hold for 10 min, 3 °C/min to 470 °C, hold for 30 min, cool to room temperature.

Core/Shell structures were fabricated using a Cambridge Savannah 200 atomic layer deposition (ALD) system. Samples were loaded in to the deposition chamber and the chamber temperature was increased to the required temperature for the different materials followed by alternating pulses of water vapor and the respective metal oxide precursor. Due to the high surface area of the films, vapor pulses were held in the reaction chamber for 3 minutes followed by opening the valve and purging with N_2 for 25 seconds before the next pulse. TiO_2 was deposited as previously reported,[21] utilizing tetrakis(dimethylamido)titanium as the precursor and a deposition temperature of 150 °C and a precursor temperature of 75 °C. The pulse durations were 0.03 s and 0.25 s for the

water vapor and TiO_2 precursor, respectively. These cycles were repeated for 1, 2, 5, 10, 20, and 40 iterations to make core/shell structures with varying thicknesses of shell material. Following shell deposition, all electrodes (including bare electrodes for comparability) were sintered a second time at 450 °C for 30 min before they were sensitized with dye. All films were sensitized in the dark from a 100 μM solution of Ru(II)phos in anhydrous ethanol for 16 hours, rinsed with ethanol, and dried under a stream of nitrogen.

Samples for TRTS spectroscopy were sealed using a second piece of fused quartz, with a 1 mm hole previously drilled into it, with a 60 μm Surlyn (Solaronix) spacer between the two pieces of quartz. The pieces of quartz were hot pressed to bond to the Surlyn and 0.1 M $HClO_4$ introduced via vacuum backfilling. Finally, the hole filling hole was covered with a small square of Surlyn, covered with a 1 cm^2 glass coverslip, and heat sealed using a soldering iron.

Characterization. Fluorescence spectroscopy was done on a SPEX Fluorolog 2 double grating fluorometer with at 450 W Xenon lamp. Electrodes for fluorescence were fabricated as above with varying thicknesses of a TiO_2 a mesoporous film of SnO_2 or ZrO_2. The instrument was operated in front facing mode with the metal oxide film tilted 45° from the excitation beam and facing nearly directly at the fluorescence detector. Emission was detected through a 1.5 mm slit width at a photomultiplier tube that had been normalized to the response sensitivity of the detector across the various wavelengths collected. Fluorescence was carried out in a N_2 degassed pH 1, 0.1 M $HClO_4$ aqueous solution. The electrodes were all excited at 460 nm and emission was collected from 510 – 800 nm with a step size of 1 nm and integration time of 1 s at each step. Experimental conditions were identical between samples in order to make emission intensity comparable across all measured electrodes.

Scanning/transmission electron microscopy (S/TEM) and energy dispersive X-ray spectroscopy (EDS) was carried out on an FEI Talos F200X S/TEM instrument.

X-ray photoelectron spectroscopy (XPS) was carried out on a PHI *VersaProbe* II Scanning XPS Microprobe.

UV/Vis spectra were collected on a Cary 6000i UV-Vis-NIR spectrometer on dry films. The instrument was blanked to air and a zero light baseline was collected by blocking the beam. Spectra were collected from 800 to 200 nm, scanning at 10 nm/s with an interval of 1 nm. Surface coverage for Ru(II)phos was calculated using the same method as Hanson et al. at 453 nm, the peak absorption of this dye:[1]

$$\Gamma = \frac{A(\lambda)}{1000 * \varepsilon(\lambda) * t}$$

where A(λ) is the baseline corrected absorbance at 453 nm, ε(λ) is the molar absorptivity constant at 453 nm and t is the film thickness.

Time-resolved terahertz spectroscopy (TRTS) was carried out as described in detail elsewhere.[21,135,137,138,140] In sum, the 35 fs pulse of an amplified Ti:sapphire laser (Spectra Physics, 800 nm, 1kHz repetition) is split into three beams: pump, generation, and detection. The generation beam is used to generate terahertz (THz) radiation by frequency doubling to 400 nm, with both the fundamental and second harmonic focused in air to generate a plasma.[141,142] The forward propagating THz radiation generated by the plasma is collected and focused using off-axis paraboloidal mirrors, and is detected using free-space electro-optic sampling with a ZnTe(110) crystal.[143] Finally, the pump beam is frequency doubled to 400 nm and a variable neutral density filter used to adjust the power to 100 mW/cm2 (6 mm diameter spot).

The TRTS scans were fit to the following function:

$$\Delta\mathrm{THz} = \left\{\Delta\mathrm{THz}_0 + \sum_{i=1}^{n} A_i \left[\exp\left(-\frac{t-t_0}{\tau_i}\right) - 1\right]\right\} \otimes \mathrm{G(fwhm)} \qquad \text{(Eq. C.1)}$$

where ΔTHz0 is the baseline before t=0, n is the number of exponentials included in the fit, t0 corresponds to the injection time (i.e., t=0), Ai is the amplitude of a given component, τi is the lifetime of a given component, G(FWHM) is a Gaussian instrument response function (determined to be 0.5 ps) and ⊗ represents a convolution.

Results

Table C.1. Fitting parameters from equation C.1 for TRTS traces in Figure 4.2

Shell thickness (Å)	A_1 (%)	τ_1 (ps)	A_2 (%)	τ_2 (ps)	A_3 (%)	τ_3 (ps)	A_4 (%)	τ_4 (ps)	scaling factor*	$\langle\tau_w\rangle$ (ps)
0.63	0.48	2.8	0.45	17	0.07	154			1.57	20
0.63	0.37	2.1	0.50	11	0.13	47			1.31	12
1.26	0.43	3.4	0.43	18	0.14	111			1.32	25
1.26	0.26	2.0	0.49	9	0.25	51			1.63	18
3.15	0.44	5.36	0.41	30	0.19	201			1.11	52
3.15	0.30	3.1	0.45	22	0.25	151			1.16	48
6.30	0.13	<0.5	0.43	28	0.44	217			0.81	108
6.30	0.10	<0.5	0.47	24	0.43	213			1.07	102
12.6	0.09	<0.5	-0.03	0.59	0.42	41	0.48	300	0.64	163
12.6	0.07	<0.5	-0.04	1.1	0.42	71	0.51	348	0.80	207
25.2	0.16	<0.5	-0.15	1.1	0.60	78	0.24	356	0.63	133
25.2	0.30	<0.5	-0.18	0.6	0.42	54	0.11	340	0.40	118

*Scaling factor is the sum of all A components before normalization

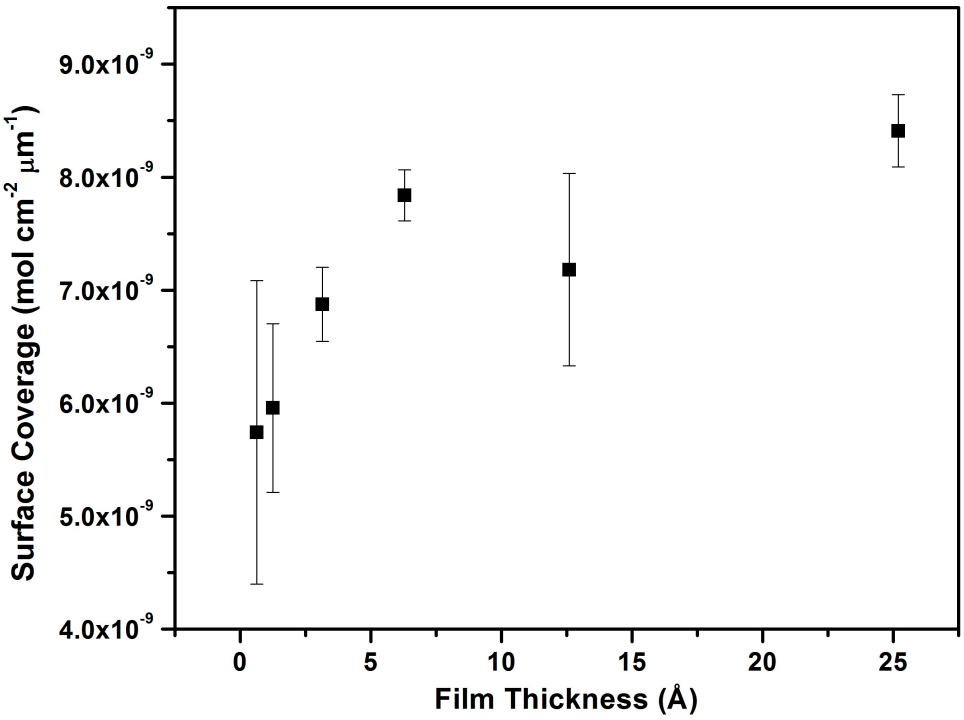

Figure C.1. Surface coverage of Ru(II)phos on the surface of the SnO_2/TiO_2 electrodes with increasing thickness of the TiO_2 shell. Surface coverage calculated from the absorbance of dry films at 453 nm.

Appendix D

Supporting Information for Chapter 5

Table D.1. Fitting Parameters for SnO_2/ZrO_2 core/shell structures from Figure 5.3.

shell oxide	Shell thickness (Å)	A_1 (%)	τ_1 (ps)	A_2 (%)	τ_2 (ps)	A_3 (%)	τ_3 (ps)	A_4 (%)	τ_4 (ps)	scaling factor	$<\tau_w>$ (ps)
Bare	0	0.20	1.1	0.58	7.5	0.22	38	-0.55	9644	1.32	17
Zr	1.02	0.36	2.8	0.52	12	0.12	67			1.45	16
	2.04	0.39	2.8	0.49	15	0.12	103			1.62	21
	2.04	0.39	2.7	0.49	14	0.12	107			1.67	20
	5.10	0.38	2.8	0.46	17	0.16	101			1.16	25
	5.10	0.42	3.2	0.46	16	0.11	106			1.21	21
	10.2	0.38	3.1	0.47	17	0.15	127			0.90	28
	10.2	0.61	5.2	0.24	24	0.16	277			0.71	52
	20.4	0.30	2.8	0.54	14	0.16	111			0.70	26
	20.4	0.45	3.6	0.44	16	0.12	98			0.68	20
	40.8	0.32	2.8	0.50	20	0.18	227			0.62	52
	40.8	0.26	2.4	0.47	18	0.27	209			0.42	66

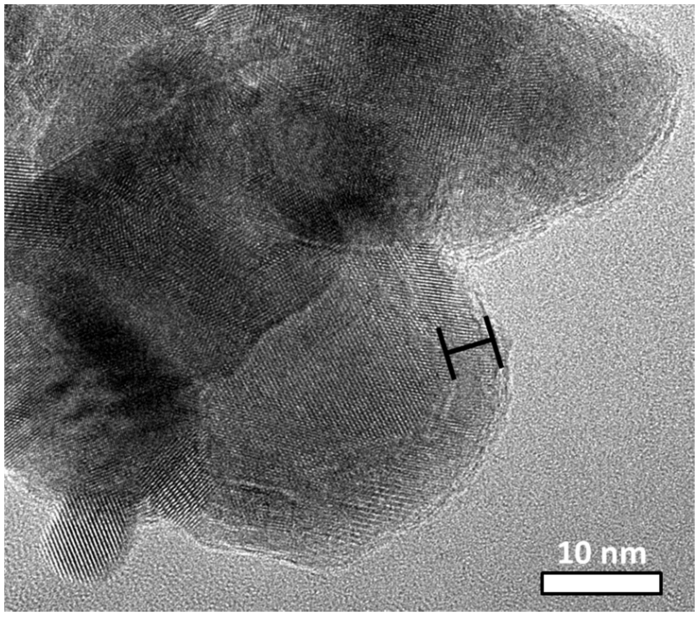

Figure D.1. High resolution TEM image of a SnO_2/40p ZrO_2 (~40 Å) scraped up nanoparticle film after use for TRTS experiment. Brackets indicate ZrO_2 film on the SnO_2 core.

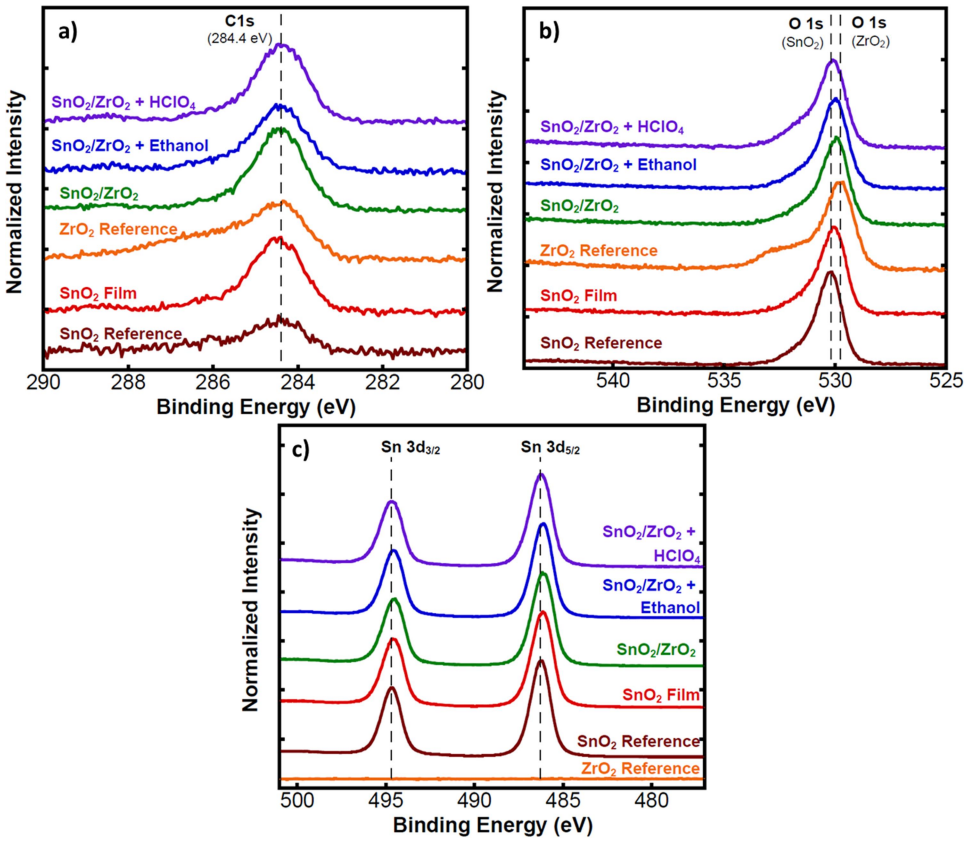

Figure D.2. High resolution XPS spectra for (a) C 1s, (b) O 1s, and (c) Sn 3d regions. Dashed lines indicate reference points for adventitious carbon and pure metal oxide spectra.

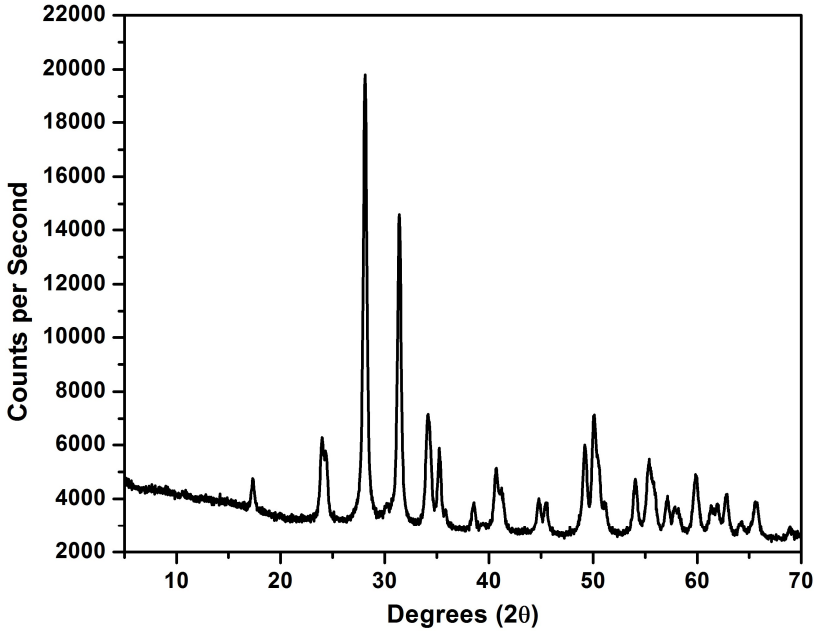

Figure D.3. X-ray diffraction pattern for ZrO_2 reference powder. Pattern matches to the monoclinic phase from ref [229].

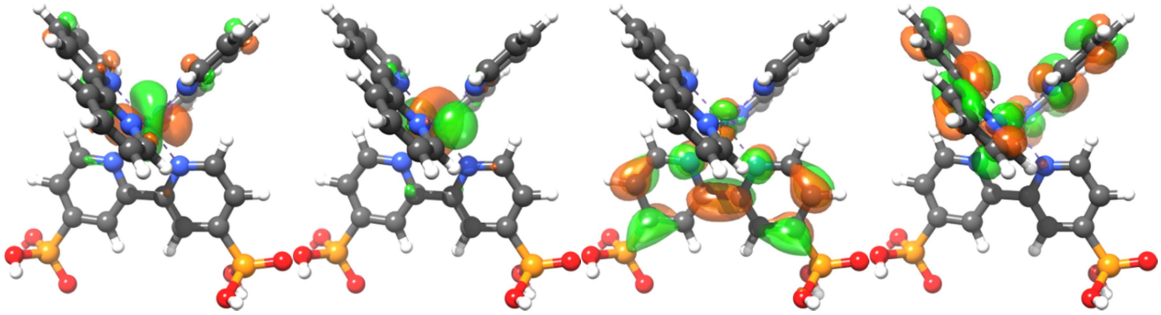

Figure D.4. Isodensity plots (isovalue=0.035) of HOMO−1, HOMO, LUMO, and LUMO+1 of the Ru(II)phos dye in its ground state, as calculated at the B3LYP/Def2SVP//Def2TZVP level of theory in a water implicit solvent.

References

(1) Hanson, K.; Brennaman, M. K.; Ito, A.; Luo, H.; Song, W.; Parker, K. A.; Ghosh, R.; Norris, M. R.; Glasson, C. R. K.; Concepcion, J. J.; Lopez, R.; Meyer, T. J. *J. Phys. Chem. C* **2012**, *116* (28), 14837.

(2) O'Regan, B.; Grätzel, M. *Nature* **1991**, *353* (6346), 737.

(3) Youngblood, W. J.; Lee, S.-H. A.; Kobayashi, Y.; Hernandez-Pagan, E. A.; Hoertz, P. G.; Moore, T. A.; Moore, A. L.; Gust, D.; Mallouk, T. E. *J. Am. Chem. Soc.* **2009**, *131* (3), 926.

(4) Limburg, B.; Bouwman, E.; Bonnet, S. *Coord. Chem. Rev.* **2012**, *256* (15-16), 1451.

(5) Swierk, J. R.; Mallouk, T. E. *Chem. Soc. Rev.* **2013**, *42* (6), 2357.

(6) Blakemore, J. D.; Crabtree, R. H.; Brudvig, G. W. *Chem. Rev.* **2015**, *115* (23), 12974.

(7) Parent, A. R.; Sakai, K. *ChemSusChem* **2014**, *7* (8), 2070.

(8) Osterloh, F. E. *Chem. Mater.* **2008**, *20*, 35.

(9) Chandiran, A. K.; Abdi-Jalebi, M.; Nazeeruddin, M. K.; Grätzel, M. *ACS Nano* **2014**, *8* (3), 2261.

(10) Asbury, J. B.; Hao, E.; Wang, Y.; Ghosh, H. N.; Lian, T. *J. Phys. Chem. B* **2001**, *105* (20), 4545.

(11) Anderson, N. A.; Ai, X.; Lian, T. *J. Phys. Chem. B* **2003**, *107* (51), 14414.

(12) Ai, X.; Anderson, N. A.; Guo, J.; Lian, T. *J. Phys. Chem. B* **2005**, *109* (15), 7088.

(13) Enright, B.; Fitzmaurice, D. *J. Phys. Chem.* **1996**, *100* (3), 1027.

(14) Tiwana, P.; Docampo, P.; Johnston, M. B.; Snaith, H. J.; Herz, L. M. *ACS Nano* **2011**, *5* (6), 5158.

(15) Tiwana, P.; Parkinson, P.; Johnston, M. B.; Snaith, H. J.; Herz, L. M. *J. Phys. Chem. C* **2010**, *114* (2), 1365.

(16) Benkö, G.; Kallioinen, J.; Korppi-Tommola, J. E. I.; Yartsev, A. P.; Sundström, V. *J. Am. Chem. Soc.* **2002**, *124* (3), 489.

(17) Benko, G.; Kallioinen, J.; Myllyperkio, P.; Trif, F.; Korppi-tommola, J. E. I.; Yartsev, A. P.; Sundstrom, V. *J. Phys. Chem. B* **2004**, *108* (Figure 2), 2862.

(18) Tachibana, Y.; Nazeeruddin, K.; Gr, M.; Klug, D. R.; Durrant, J. R. *Chem. Phys.* **2002**, *285*, 127.

(19) Asbury, J. B.; Ellingson, R. J.; Ghosh, H. N.; Ferrere, S.; Nozik, A. J.; Lian, T. *J.*

Phys. Chem. B **1999**, *103* (16), 3110.

(20) Asbury, J. B.; Anderson, N. a; Hao, E.; Ai, X.; Lian, T. *J. Phys. Chem. B* **2003**, *107* (30), 7376.

(21) Swierk, J. R.; McCool, N. S.; Nemes, C. T.; Mallouk, T. E.; Schmuttenmaer, C. A. *J. Phys. Chem. C* **2016**, *120* (11), 5940.

(22) Asbury, J. B.; Wang, Y.-Q.; Hao, E.; Ghosh, H. N.; Lian, T. *Res. Chem. Intermed.* **2001**, *27* (4-5), 393.

(23) Damrauer, N. H.; Cerullo, G.; Yeh, A.; Boussie, T. R.; Shank, C. V; Mccusker, J. K. *Science (80-.).* **1997**, *275*, 54.

(24) Milot, R. L.; Moore, G. F.; Crabtree, R. H.; Brudvig, G. W.; Schmuttenmaer, C. A. *J. Phys. Chem. C* **2013**, *117* (42), 21662.

(25) Milot, R. L.; Schmuttenmaer, C. A. *Acc. Chem. Res.* **2015**, *48* (5), 1423.

(26) Swierk, J. R.; Méndez-Hernández, D. D.; McCool, N. S.; Liddell, P.; Terazono, Y.; Pahk, I.; Tomlin, J. J.; Oster, N. V; Moore, T. A.; Moore, A. L.; Gust, D.; Mallouk, T. E. *Proc. Natl. Acad. Sci. U. S. A.* **2015**, *112* (6), 1681.

(27) Sorantin, P.; Schwarz, K. *Inorg. Chem.* **1992**, *31* (17), 567.

(28) Tachibana, Y.; Haque, S. a; Mercer, I. P.; Durrant, J. R.; Klug, D. R. *J. Phys. Chem. B* **2000**, *104* (6), 1198.

(29) Hannappel, T.; Burfeindt, B.; Storck, W.; Willig, F. *J. Phys. Chem. B* **1997**, *101* (35), 6799.

(30) Kelly, C. A.; Farzad, F.; Thompson, D. W.; Stipkala, J. M.; Meyer, G. J. *Langmuir* **1999**, *15* (20), 7047.

(31) Asbury, J. B.; Hao, E.; Wang, Y.; Lian, T. *J. Phys. Chem. B* **2000**, *104*, 11957.

(32) Heimer, T. A.; D'Arcangelis, S. T.; Farzad, F.; Stipkala, J. M.; Meyer, G. J. *Inorg. Chem.* **1996**, *35* (18), 5319.

(33) Warnan, J.; Guerin, V.-M.; Anne, F. B.; Pellegrin, Y.; Blart, E.; Jacquemin, D.; Pauporté, T.; Odobel, F. *J. Phys. Chem. C* **2013**, *117* (17), 8652.

(34) Tachibana, Y.; Haque, S. a; Mercer, I. P.; Moser, J.-E.; Klug, D. R.; Durrant, J. R. *J. Phys. Chem. B* **2001**, *105* (31), 7424.

(35) Qu, P.; Meyer, G. J. *Langmuir* **2001**, *17* (21), 6720.

(36) Park, N. G.; Chang, S. H.; Van de Lagemaat, J.; Kim, K. J.; Frank, A. J. *Bull. Korean Chem. Soc.* **2000**, *21* (10), 985.

(37) Jennings, J. R.; Wang, Q. *J. Phys. Chem. C* **2010**, *114* (3), 1715.

(38) Swierk, J. R.; McCool, N. S.; Saunders, T. P.; Barber, G. D.; Mallouk, T. E. *J. Am. Chem. Soc.* **2014**, *136* (31), 10974.

(39) Nelson, J.; Haque, S.; Klug, D.; Durrant, J. *Phys. Rev. B* **2001**, *63*, 205321.

(40) Nelson, J.; Chandler, R. E. *Coord. Chem. Rev.* **2004**, *248* (13-14), 1181.

(41) Cahen, D.; Hodes, G.; Gra, M. *J. Phys. Chem. B* **2000**, *9* (104), 2053.

(42) Lagemaat, J. Van De; Frank, A. J. *J. Phys. Chem. B* **2000**, *104* (18), 4292.

(43) Lagemaat, J. Van De; Frank, A. J. *J. Phys. Chem. B* **2001**, *105* (45), 11194.

(44) Austin, I. G.; Mott, N. F. *Adv. Phys.* **2000**, *50* (7), 757.

(45) Swierk, J. R.; McCool, N. S.; Mallouk, T. E. *J. Phys. Chem. C* **2015**, *119* (24), 13858.

(46) Haque, S. A.; Tachibana, Y.; Willis, R. L.; Moser, J. E.; Grätzel, M.; Klug, D. R.; Durrant, J. R. *J. Phys. Chem. B* **2000**, *104* (3), 538.

(47) Haque, S. A.; Tachibana, Y.; Klug, D. R.; Durrant, J. R. *J. Phys. Chem. B* **1998**, *102* (10), 1745.

(48) Subramanian, A.; Bow, J. S.; Wang, H. W. *Thin Solid Films* **2012**, *520* (23), 7011.

(49) Halverson, A. F.; Zhu, K.; Erslev, P. T.; Kim, J. Y.; Neale, N. R.; Frank, A. J. *Nano Lett.* **2012**, *12* (4), 2112.

(50) Savory, D. M.; McQuillan, A. J. *J. Phys. Chem. C* **2013**, *117* (45), 23645.

(51) Kavan, L.; Tétreault, N.; Moehl, T.; Grätzel, M. *J. Phys. Chem. C* **2014**, *118* (30), 16408.

(52) Betz, G.; Tributsch, H.; Marchand, R. *J. Appl. Electrochem.* **1984**, *14* (3), 315.

(53) Chen, X.; Liu, L.; Liu, Z.; Marcus, M. A.; Wang, W.-C.; Oyler, N. a; Grass, M. E.; Mao, B.; Glans, P.-A.; Yu, P. Y.; Guo, J.; Mao, S. S. *Sci. Rep.* **2013**, *3*, 1510.

(54) Chen, X.; Liu, L.; Yu, P. Y.; Mao, S. S. *Science* **2011**, *331* (6018), 746.

(55) Cass, M. J.; Qiu, F. L.; Walker, A. B.; Fisher, A. C.; Peter, L. M. *J. Phys. Chem. B* **2003**, *107* (1), 113.

(56) Kroeze, J. E.; Savenije, T. J.; Warman, J. M. *J. Am. Chem. Soc.* **2004**, *126* (24), 7608.

(57) Benkstein, K. D.; Kopidakis, N.; van de Lagemaat, J.; Frank, A. J. *J. Phys. Chem. B* **2003**, *107* (31), 7759.

(58) Rao, P.; Schiff, E. A.; Tsybeskov, L.; Fauchet, P. M. *MRS Online Proc. Libr.* **1997**, *452*, 613.

(59) Němec, H.; Rochford, J.; Taratula, O.; Galoppini, E.; Kužel, P.; Polívka, T.; Yartsev, A.; Sundström, V. *Phys. Rev. Lett.* **2010**, *104* (19), 197401.

(60) Němec, H.; Kužel, P.; Sundström, V. *Phys. Rev. B - Condens. Matter Mater. Phys.* **2009**, *79* (11), 115309.

(61) Jarzebski, Z. M.; Marton, J. P. *J. Electrochem. Soc.* **1976**, *123* (9), 299C.

(62) Jousse, D.; Constantino, C.; Chambouleyron, I. *J. Appl. Phys.* **1983**, *54* (1), 431.

(63) Shanthi, E.; Dutta, V.; Banerjee, A.; Chopra, K. L. *J. Appl. Phys.* **1980**, *51* (12), 6243.

(64) Green, A. N. M.; Palomares, E.; Haque, S. A.; Kroon, J. M.; Durrant, J. R. *J. Phys. Chem. B* **2005**, *109* (25), 12525.

(65) Grätzel, M. *Nature* **2001**, *414* (6861), 338.

(66) Birkel, A.; Lee, Y.-G.; Koll, D.; Meerbeek, X. Van; Frank, S.; Choi, M. J.; Kang, Y. S.; Char, K.; Tremel, W. *Energy Environ. Sci.* **2012**, *5* (1), 5392.

(67) Lee, J. H.; Park, N. G.; Shin, Y. J. *Sol. Energy Mater. Sol. Cells* **2011**, *95* (1), 179.

(68) Ramasamy, E.; Lee, J. *J. Phys. Chem. C* **2010**, *114* (50), 22032.

(69) Benkö, G.; Myllyperkio, P.; Pan, J.; Yartsev, A. P.; Sundstro, V. *J. Am. Chem. Soc.* **2003**, *125*, 1118.

(70) Knauf, R. R.; Brennaman, M. K.; Alibabaei, L.; Norris, M. R.; Dempsey, J. L. *J. Phys. Chem. C* **2013**, *117* (48), 25259.

(71) Kamat, P. V; Bedja, I.; Hotchandani, S.; Patterson, L. K. *J. Phys. Chem.* **1996**, *100* (12), 4900.

(72) Diamant, Y.; Chappel, S.; Chen, S. G.; Melamed, O.; Zaban, A. *Coord. Chem. Rev.* **2004**, *248* (13-14), 1271.

(73) Lee, S. A.; Zhao, Y.; Hernandez-pagan, E. a.; Blasdel, L.; Youngblood, W. J.; Mallouk, T. E.; Justin, W.; Mallouk, T. E. *Faraday Discuss.* **2012**, *155*, 165.

(74) Hanson, K.; Losego, M. D.; Kalanyan, B. B.; Parsons, G. N.; Meyer, T. J. *Nano Lett.* **2013**, *13* (10), 4802.

(75) Hanson, K.; Losego, M. D.; Kalanyan, B. B.; Ashford, D. L.; Parsons, G. N.; Meyer, T. J. *Chem. Mater.* **2013**, *25* (1), 3.

(76) Prasittichai, C.; Avila, J. R.; Farha, O. K.; Hupp, J. T. *J. Am. Chem. Soc.* **2013**, *135* (44), 16328.

(77) Menzies, D. B.; Cervini, R.; Cheng, Y.; Simon, G. P. *J. Sol-Gel Sci. Technol.* **2004**, *32*, 363.

(78) Sherman, B. D.; Ashford, D. L.; Lapides, A. M.; Sheridan, M. V; Wee, K. R.; Meyer, T. J. *J. Phys. Chem. Lett.* **2015**, *6* (16), 3213.

(79) Wee, K.-R.; Sherman, B. D.; Brennaman, M. K.; Sheridan, M. V.; Nayak, A.; Alibabaei, L.; Meyer, T. J. *J. Mater. Chem. A* **2016**, *4* (8), 2969.

(80) Knauf, R. R.; Kalanyan, B.; Parsons, G. N.; Dempsey, J. L. *J. Phys. Chem. C* **2015**, *119* (51), 28353.

(81) Pawsey, S.; Yach, K.; Reven, L. *Langmuir* **2002**, *18* (13), 5205.

(82) Lapides, A. M.; Sherman, B. D.; Brennaman, M. K.; Dares, C. J.; Skinner, K. R.; Templeton, J. L.; Meyer, T. J. *Chem. Sci.* **2015**, *6* (11), 6398.

(83) Neouze, M.-A.; Schubert, U. *Monatshefte für Chemie - Chem. Mon.* **2008**, *139* (3), 183.

(84) Mutin, P. H.; Guerrero, G.; Vioux, A. *J. Mater. Chem.* **2005**, *15* (35-36), 3761.

(85) Viornery, C.; Chevolot, Y.; Léonard, D.; Aronsson, B.-O.; Péchy, P.; Mathieu, H. J.; Descouts, P.; Grätzel, M. *Langmuir* **2002**, *18* (7), 2582.

(86) Adden, N.; Gamble, L. J.; Castner, D. G.; Hoffmann, A.; Gross, G.; Menzel, H. *Langmuir* **2006**, *22* (19), 8197.

(87) Bae, E.; Choi, W.; Park, J.; Shin, H. S.; Kim, S. Bin; Lee, J. S. *J. Phys. Chem. B* **2004**, *108* (37), 14093.

(88) Negre, C. F. A.; Milot, R. L.; Martini, L. A.; Ding, W.; Crabtree, R. H.; Schmuttenmaer, C. A.; Batista, V. S. *J. Phys. Chem. C* **2013**, *117*, 24462.

(89) Nazeeruddin, M. K.; Kay, A.; Rodicio, I.; Humphry-Baker, R.; Mueller, P.; Liska, P.; Vlachopoulos, N.; Gratzel, M. *J. Am. Chem. Soc.* **1993**, *115* (4), 6382.

(90) Grätzel, M. *J. Photochem. Photobiol. A Chem.* **2004**, *164* (1-3), 3.

(91) Galoppini, E. *Coord. Chem. Rev.* **2004**, *248* (13-14), 1283.

(92) Young, K. J.; Martini, L. A.; Milot, R. L.; Snoeberger, R. C.; Batista, V. S.; Schmuttenmaer, C. A.; Crabtree, R. H.; Brudvig, G. W. *Coord. Chem. Rev.* **2012**, *256* (21-22), 2503.

(93) Hanson, K.; Brennaman, M. K.; Luo, H.; Glasson, C. R. K.; Concepcion, J. J.; Song, W.; Meyer, T. J. *Appl. Mater. Interfaces* **2012**, *4* (3), 1462.

(94) Gillaizeau-Gauthier, I.; Odobel, F.; Alebbi, M.; Argazzi, R.; Costa, E.; Bignozzi, C. A.; Qu, P.; Meyer, G. J. *Inorg. Chem.* **2001**, *40* (23), 6073.

(95) Péchy, P.; Rotzinger, F. P.; Nazeeruddin, M. K.; Kohle, O.; Zakeeruddin, S. M.; Humphry-Baker, R.; Grätzel, M. *J. Chem. Soc. Chem. Commun.* **1995**, No. 1, 65.

(96) Pawsey, S.; McCormick, M.; De Paul, S.; Graf, R.; Lee, Y. S.; Reven, L.; Spiess, H. W. *J. Am. Chem. Soc.* **2003**, *125* (14), 4174.

(97) Ernstorfer, R.; Gundlach, L.; Felber, S.; Storck, W.; Eichberger, R.; Willig, F. *J. Phys. Chem. B* **2006**, *110* (50), 25383.

(98) McNamara, W. R.; Snoeberger III, R. C.; Li, G.; Richter, C.; Allen, L. J.; Milot, R. L.; Schmuttenmaer, C. A.; Crabtree, R. H.; Brudvig, G. W.; Batista, V. S. *Energy Environ. Sci.* **2009**, *2* (11), 1173.

(99) McConnell, I.; Li, G.; Brudvig, G. W. *Chem. Biol.* **2010**, *17* (5), 434.

(100) Trammell, S. A.; Wimbish, J. C.; Odobel, F.; Gallagher, L. A.; Narula, P. M.; Meyer, T. J. *J. Am. Chem. Soc.* **1998**, *120* (50), 13248.

(101) Abuabara, S. G.; Cady, C. W.; Baxter, J. B.; Schmuttenmaer, C. A.; Crabtree, R. H.; Brudvig, G. W.; Batista, V. S. *J. Phys. Chem. C* **2007**, *111* (32), 11982.

(102) Ramakrishna, G.; Verma, S.; Jose, D. A.; Krishna Kumar, O.; Das, A.; Palit, D. K.; Ghosh, H. N. *J. Phys. Chem. B* **2006**, *110* (18), 9012.

(103) Verma, S.; Kar, P.; Das, A.; Palit, D. K.; Ghosh, H. N.; Emission, C. *J. Phys. Chem. C* **2008**, *112* (8), 2918.

(104) Mcnamara, W. R.; Snoeberger (III), R. C.; Li, G.; Schleicher, J. M.; Cady, C. W.; Poyatos, M.; Schmuttenmaer, C. A.; Crabtree, R. H.; Brudvig, G. W.; Batista, V. S. *J. Am. Chem. Soc.* **2008**, *130* (43), 14329.

(105) Materna, K. L.; Brennan, B. J.; Brudvig, G. W. *Dalt. Trans.* **2015**, *44*, 1.

(106) Brennan, B. J.; Llansola Portolés, M. J.; Liddell, P. a; Moore, T. a; Moore, A. L.; Gust, D. *Phys. Chem. Chem. Phys.* **2013**, *15*, 16605.

(107) Brewster, T. P.; Konezny, S. J.; Sheehan, S. W.; Martini, L. A.; Schmuttenmaer, C. A.; Batista, V. S.; Crabtree, R. H. *Inorg. Chem.* **2013**, *52* (11), 6752.

(108) Martini, L. A.; Moore, G. F.; Milot, R. L.; Cai, L. Z.; Sheehan, S. W.; Schmuttenmaer, C. A.; Brudvig, G. W.; Crabtree, R. H. *J. Phys. Chem. C* **2013**, *117* (28), 14526.

(109) McNamara, W. R.; Milot, R. L.; Song, H.; Snoeberger III, R. C.; Batista, V. S.; Schmuttenmaer, C. A.; Brudvig, G. W.; Crabtree, R. H. *Energy Environ. Sci.* **2010**, *3* (7), 917.

(110) Moser, J. E.; Grätzel, M. *Chem. Phys.* **1993**, *176* (2-3), 493.

(111) Rajh, T.; Chen, L. X.; Lukas, K.; Liu, T.; Thurnauer, M. C.; Tiede, D. M. *J. Phys. Chem. B* **2002**, *106* (41), 10543.

(112) Folkers, J. P.; Gorman, C. B.; Laibinis, P. E.; Buchholz, S.; Whitesides, G. M.; Nuzzo, R. G. *Langmuir* **1995**, *11* (4), 813.

(113) She, C.; Guo, J.; Irle, S.; Morokuma, K.; Mohler, D. L.; Zabri, H.; Odobel, F.; Youm, K. T.; Liu, F.; Hupp, J. T.; Lian, T. *J. Phys. Chem. A* **2007**, *111* (29), 6832.

(114) Persson, P.; Lundqvist, M. J.; Ernstorfer, R.; Goddard, W. A.; Willig, F. *J. Chem. Theory Comput.* **2006**, *2* (2), 441.

(115) Duncan, W. R.; Prezhdo, O. V. *J. Phys. Chem. B* **2005**, *109* (1), 365.

(116) Persson, P.; Bergström, R.; Lunell, S. *J. Phys. Chem. B* **2000**, *104* (44), 10348.

(117) Xu, Y.; Chen, W.-K.; Liu, S.-H.; Cao, M.-J.; Li, J.-Q. *Chem. Phys.* **2007**, *331* (2-3), 275.

(118) Park, H.; Bae, E.; Lee, J. J.; Park, J.; Choi, W. *J. Phys. Chem. B* **2006**, *110* (17), 8740.

(119) Moore, G. F.; Brudvig, G. W. *Annu. Rev. Condens. Matter Phys.* **2011**, *2* (1), 303.

(120) McEvoy, J. P.; Brudvig, G. W. *Chem. Rev.* **2006**, *106* (11), 4455.

(121) Brennan, B. J.; Durrell, A. C.; Koepf, M.; Crabtree, R. H.; Brudvig, G. W. *Phys. Chem. Chem. Phys.* **2015**, *17* (19), 12728.

(122) Zhao, Y.; Swierk, J. R.; Megiatto, J. D.; Sherman, B.; Youngblood, W. J.; Qin, D.; Lentz, D. M.; Moore, A. L.; Moore, T. A.; Gust, D.; Mallouk, T. E. *Proc. Natl. Acad. Sci. U. S. A.* **2012**, *109* (39), 15612.

(123) Swierk, J. R.; McCool, N. S.; Saunders, T. P.; Barber, G. D.; Strayer, M. E.; Vargas-Barbosa, N. M.; Mallouk, T. E. *J. Phys. Chem. C* **2014**, *118* (30), 17046.

(124) Gao, Y.; Ding, X.; Liu, J.; Wang, L.; Lu, Z.; Li, L.; Sun, L. *J. Am. Chem. Soc.* **2013**, *135* (11), 4219.

(125) Li, L.; Duan, L.; Xu, Y.; Gorlov, M.; Hagfeldt, A.; Sun, L. *Chem. Commun.* **2010**, *46* (39), 7307.

(126) Li, F.; Fan, K.; Xu, B.; Gabrielsson, E.; Daniel, Q.; Li, L.; Sun, L. *J. Am. Chem. Soc.* **2015**, *137* (28), 9153.

(127) Moore, G. F.; Blakemore, J. D.; Milot, R. L.; Hull, J. F.; Song, H.; Cai, L.; Schmuttenmaer, C. a.; Crabtree, R. H.; Brudvig, G. W. *Energy Environ. Sci.* **2011**, *4* (7), 2389.

(128) Poddutoori, P. K.; Thomsen, J. M.; Milot, R. L.; Sheehan, S. W.; Negre, C. F. A.; Garapati, V. K. R.; Schmuttenmaer, C. A.; Batista, V. S.; Brudvig, G. W.; van der Est, A. *J. Mater. Chem. A* **2015**, *3* (7), 3868.

(129) Alibabaei, L.; Brennaman, M. K.; Norris, M. R.; Kalanyan, B.; Song, W.; Losego, M. D.; Concepcion, J. J.; Binstead, R. a.; Parsons, G. N.; Meyer, T. J. *Proc. Nat. Acad. Sci. USA* **2013**, *110* (50), 20008.

(130) Michaux, K. E.; Gambardella, A. A.; Alibabaei, L.; Ashford, D. L.; Sherman, B. D.; Binstead, R. A.; Meyer, T. J.; Murray, R. W. *J. Phys. Chem. C* **2015**, *119* (29), 17023.

(131) Xiang, X.; Fielden, J.; Rodríguez-Córdoba, W.; Huang, Z.; Zhang, N.; Luo, Z.; Musaev, D. G.; Lian, T.; Hill, C. L. *J. Phys. Chem. C* **2013**, *117* (2), 918.

(132) Fielden, J.; Sumliner, J. M.; Han, N.; Geletii, Y. V.; Xiang, X.; Musaev, D. G.; Lian, T.; Hill, C. L. *Chem. Sci.* **2015**, *6* (10), 5531.

(133) Creutz, C.; Sutin, N. *Proc. Natl. Acad. Sci. U. S. A.* **1975**, *72* (8), 2858.

(134) Giokas, P. G.; Miller, S. A.; Hanson, K.; Norris, M. R.; Glasson, C. R. K.; Concepcion, J. J.; Bettis, S. E.; Meyer, T. J.; Moran, A. M. *J. Phys. Chem. C* **2013**, *117* (2), 812.

(135) Beard, M. C.; Turner, G. M.; Schmuttenmaer, C. A. *Phys. Rev. B - Condens. Matter Mater. Phys.* **2000**, *62* (23), 15764.

(136) Ito, S.; Chen, P.; Comte, P.; Nazeeruddin, M. K.; Liska, P.; Péchy, P.; Grätzel, M. *Prog. Photovoltaics* **2007**, *15* (7), 603.

(137) Turner, G. M.; Beard, M. C.; Schmuttenmaer, C. A. *J. Phys. Chem. B* **2002**, *106* (45), 11716.

(138) Baxter, J. B.; Schmuttenmaer, C. A. *J. Phys. Chem. B* **2006**, *110* (50), 25229.

(139) Beard, M. C.; Turner, G. M.; Schmuttenmaer, C. A. *J. Appl. Phys.* **2001**, *90* (12), 5915.

(140) Nemes, C. T.; Koenigsmann, C.; Schmuttenmaer, C. A. *J. Phys. Chem. Lett.* **2015**, *6* (16), 3257.

(141) Cook, D. J.; Hochstrasser, R. M. *Opt. Lett.* **2000**, *25* (16), 1210.

(142) Bartel, T.; Gaal, P.; Reimann, K.; Woerner, M.; Elsaesser, T. *Opt. Lett.* **2005**, *30* (20), 2805.

(143) Wu, Q.; Zhang, X. C. *Appl. Phys. Lett.* **1995**, *67* (1995), 3523.

(144) Pijpers, J. J. H.; Ulbricht, R.; Derossi, S.; Reek, J. N. H.; Bonn, M. *J. Phys. Chem. C* **2011**, *115* (5), 2578.

(145) Furube, A.; Katoh, R.; Hara, K.; Murata, S.; Arakawa, H.; Tachiya, M. *J. Phys. Chem. B* **2003**, *107* (17), 4162.

(146) Furube, A.; Katoh, R.; Yoshihara, T.; Hara, K.; Murata, S.; Arakawa, H.; Tachiya, M. *J. Phys. Chem. B* **2004**, *108* (33), 12583.

(147) Listorti, A.; O'Regan, B.; Durrant, J. R. *Chem. Mater.* **2011**, *23* (15), 3381.

(148) Li, T. T. T.; Weaver, M. J. *1Journal Am. Chem. Soc.* **1984**, *106* (20), 6107.

(149) Diebold, U. *Surf. Sci. Rep.* **2003**, *48* (5-8), 53.

(150) Fujishima, A.; Zhang, X.; Tryk, D. *Surf. Sci. Rep.* **2008**, *63* (12), 515.

(151) Nakata, K.; Fujishima, A. *J. Photochem. Photobiol. C* **2012**, *13* (3), 169.

(152) Hendry, E.; Koeberg, M.; O'Regan, B.; Bonn, M. *Nano Lett.* **2006**, *6* (4), 755.

(153) Kopidakis, N.; Schiff, E. A.; Park, N.-G.; van de Lagemaat, J.; Frank, A. J. *J. Phys. Chem. B* **2000**, *104* (16), 3930.

(154) Wang, Q.; Zhang, Z.; Zakeeruddin, S. M.; Gratzel, M. *J. Phys. Chem. C* **2008**, *112* (17), 7084.

(155) Savory, D. M.; McQuillan, A. J. *J. Phys. Chem. C* **2014**, *118* (25), 13680.

(156) Lyon, L. A.; Hupp, J. T. *J. Phys. Chem. B* **1999**, *103* (22), 4623.

(157) Kılıç, C.; Zunger, A. *Appl. Phys. Lett.* **2002**, *81* (1), 73.

(158) Peacock, P. W.; Robertson, J. *Appl. Phys. Lett.* **2003**, *83* (10), 2025.

(159) Walle, C. G. Van De; Neugebauer, J. *Nature* **2003**, *423* (6940), 626.

(160) Koudriachova, M. V.; de Leeuw, S. W.; Harrison, N. M. *Phys. Rev. B* **2004**, *70* (16), 165421.

(161) Chen, W. P.; Wang, Y.; Chan, H. L. W. *Appl. Phys. Lett.* **2008**, *92* (11), 112907.

(162) McIntyre, P. C.; Ahn, J.-H.; Becker, R. J.; Wang, R.-V.; Gilbert, S. R.; Mirkarimi, L. W.; Schulberg, M. T. *J. Appl. Phys.* **2001**, *89* (11), 6378.

(163) Caramori, S.; Cristino, V.; Argazzi, R.; Meda, L.; Bignozzi, C. A. *Inorg. Chem.* **2010**, *49* (7), 3320.

(164) Ito, S.; Murakami, T. N.; Comte, P.; Liska, P.; Grätzel, C.; Nazeeruddin, M. K.; Grätzel, M. *Thin Solid Films* **2008**, *516* (14), 4613.

(165) Roger, I.; Symes, M. D. *J. Am. Chem. Soc.* **2015**, *137* (43), 13980.

(166) Trotochaud, L.; Young, S. L.; Ranney, J. K.; Boettcher, S. W. *J. Am. Chem. Soc.* **2014**, *136* (18), 6744.

(167) Du, C.; Zhang, M.; Jang, J.; Liu, Y.; Liu, G.; Wang, D. *J. Phys. Chem. C* **2014**, *118*, 17054.

(168) Lindsey, C. P.; Patterson, G. D. *J. Chem. Phys.* **1980**, *73* (7), 3348.

(169) Abrahamsson, M.; Johansson, P. G.; Ardo, S.; Kopecky, A.; Galoppini, E.; Meyer, G. J. *J. Phys. Chem. Lett.* **2010**, *1*, 1725.

(170) Rebbah, H.; Hervieu, M.; Raveau, B. *Mater. Res. Bull.* **1981**, *16* (2), 149.

(171) Tournoux, M.; Marchand, R.; Brohan, L. *Prog. Solid State Chem.* **1986**, *17* (1), 33.

(172) Yin, S.; Uchida, S.; Fujishiro, Y.; Aki, M.; Sato, T. *J. Mater. Chem.* **1999**, *9* (5), 1191.

(173) Lemon, B. I.; Hupp, J. T. *J. Phys. Chem.* **1996**, *100* (35), 14578.

(174) Lewis, N. S.; Nocera, D. G. *Proc. Natl. Acad. Sci.* **2006**, *103* (43), 15729.

(175) Nealson, K. H.; Conrad, P. G. *Philos. Trans. R. Soc. B Biol. Sci.* **1999**, *354* (1392), 1923.

(176) Blankenship, R. E.; Tiede, D. M.; Barber, J.; Brudvig, G. W.; Fleming, G.; Ghirardi, M.; Gunner, M. R.; Junge, W.; Kramer, D. M.; Melis, A.; Moore, T. a; Moser, C. C.; Nocera, D. G.; Nozik, A. J.; Ort, D. R.; Parson, W. W.; Prince, R. C.; Sayre, R. T. *Science (80-.).* **2011**, *332* (6031), 805.

(177) Grabolle, M.; Dau, H. *Biochim. Biophys. Acta - Bioenerg.* **2005**, *1708* (2), 209.

(178) Gust, D.; Moore, T. A.; Moore, A. L. *Acc. Chem. Res.* **2009**, *42* (12), 1890.

(179) Wasielewski, M. R. *Acc. Chem. Res.* **2009**, *42* (12), 1910.

(180) Kärkäs, M. D.; Johnston, E. V.; Verho, O.; Åkermark, B. *Acc. Chem. Res.* **2014**, *47* (1), 100.

(181) Dendooven, J.; Devloo-Casier, K.; Levrau, E.; Van Hove, R.; Sree, S. P.; Baklanov, M. R.; Martens, J. A.; Detavernier, C. *Langmuir* **2012**, *28* (8), 3852.

(182) Johnson, R. W.; Hultqvist, A.; Bent, S. F. *Mater. Today* **2014**, *17* (5), 236.

(183) Sakai, N.; Ebina, Y.; Takada, K.; Sasaki, T. *J. Am. Chem. Soc.* **2004**, *126* (18), 5851.

(184) Parkinson, P.; Joyce, H. J.; Gao, Q.; Tan, H. H.; Zhang, X.; Zou, J.; Jagadish, C.; Herz, L. M.; Johnston, M. B. *Nano Lett.* **2009**, *9* (9), 3349.

(185) Boland, J. L.; Casadei, A.; Tütüncüoglu, G.; Matteini, F.; Davies, C. L.; Jabeen, F.; Joyce, H. J.; Herz, L. M.; Fontcuberta i Morral, A.; Johnston, M. B. *ACS Nano* **2016**, *10* (4), 4219.

(186) Lee, J.-J.; Rahman, M. M.; Sarker, S.; Nath, N. C. D.; Ahammad, A. J. S.; Lee, J. K. In *Advances in Composite Materials for Medicine and Nanotechnology*; Attaf, B., Ed.; InTech, 2011; pp 181–210.

(187) Menzies, D. B.; Dai, Q.; Bourgeois, L.; Caruso, R. A.; Cheng, Y.-B.; Simon, G. P.; Spiccia, L. *Nanotechnology* **2007**, *18* (12), 125608.

(188) Gaussian 09, Revision D.01, Frisch, M. J.; Trucks, G. W.; Schlegel, H. B.;

Scuseria, G. E.; Robb, M. A.; Cheeseman, J. R.; Scalmani, G.; Barone, V.; Mennucci, B.; Petersson, G. A.; Nakatsuji, H.; Caricato, M.; Li, X.; Hratchian, H. P.; Izmaylov, A. F.; Bloino, J.; Zheng, G.; Sonnenberg, J. L.; Hada, M.; Ehara, M.; Toyota, K.; Fukuda, R.; Hasegawa, J.; Ishida, M.; Nakajima, T.; Honda, Y.; Kitao, O.; Nakai, H.; Vreven, T.; Montgomery, J. A., Jr.; Peralta, J. E.; Ogliaro, F.; Bearpark, M.; Heyd, J. J.; Brothers, E.; Kudin, K. N.; Staroverov, V. N.; Kobayashi, R.; Normand, J.; Raghavachari, K.; Rendell, A.; Burant, J. C.; Iyengar, S. S.; Tomasi, J.; Cossi, M.; Rega, N.; Millam, J. M.; Klene, M.; Knox, J. E.; Cross, J. B.; Bakken, V.; Adamo, C.; Jaramillo, J.; Gomperts, R.; Stratmann, R. E.; Yazyev, O.; Austin, A. J.; Cammi, R.; Pomelli, C.; Ochterski, J. W.; Martin, R. L.; Morokuma, K.; Zakrzewski, V. G.; Voth, G. A.; Salvador, P.; Dannenberg, J. J.; Dapprich, S.; Daniels, A. D.; Farkas, Ö.; Foresman, J. B.; Ortiz, J. V.; Cioslowski, J.; Fox, D. J. Gaussian, Inc., Wallingford CT, 2009.

(189) Becke, A. D. *J. Chem. Phys.* **1993**, *98* (7), 5648.

(190) Marenich, A. V.; Cramer, C. J.; Truhlar, D. G. *J. Phys. Chem. B* **2009**, *113* (18), 6378.

(191) Weigend, F.; Ahlrichs, R. *Phys. Chem. Chem. Phys.* **2005**, *7* (18), 3297.

(192) IUPAC. In *IUPAC Compendium of Chemical Terminology*; IUPAC: Research Triagle Park, NC.

(193) Hush, N. S. *Electrochim. Acta* **1968**, *13* (5), 1005.

(194) Lyons, J. L.; Janotti, A.; Van de Walle, C. G. *Microelectron. Eng.* **2011**, *88* (7), 1452.

(195) Krishnan Rajeshwar. In *Encyclopedia of Electrochemistry*; Bard, A. J., Ed.; Wiley-VCH Verlag GmbH & Co. KGaA: Weinheim, Germany, 2007.

(196) Matsuoka, M.; Isotani, S.; Miyake, S.; Setsuhara, Y.; Ogata, K.; Kuratani, N. *J. Appl. Phys.* **1996**, *80* (2), 1177.

(197) Mondal, A.; Ram, S. *Chem. Phys. Lett.* **2003**, *382* (3-4), 297.

(198) Howard, C. J.; Hill, R. J.; Reichert, B. E. *Acta Crystallogr. Sect. B Struct. Sci.* **1988**, *44* (2), 116.

(199) Shojai, F.; Mäntylä, T. . *J. Eur. Ceram. Soc.* **2001**, *21* (1), 37.

(200) Annamalai, V. E.; Gokularathnam, C. V.; Krishnamurthy, R. *J. Mater. Sci. Lett.* **1992**, *11* (12), 824.

(201) Chen, W. P.; He, K. F.; Wang, Y.; Hu, Y. M.; Cao, J. L.; Chan, H. L. W. *Jpn. J. Appl. Phys.* **2010**, *49* (5), 051103.

(202) Özer, N.; Chen, D.-G.; Lampert, C. M. *Thin Solid Films* **1996**, *277* (1-2), 162.

(203) Bae, K.; Son, K. S.; Kim, J. W.; Park, S. W.; An, J.; Prinz, F. B.; Shim, J. H. *Int. J.*

Hydrogen Energy **2014**, *39* (6), 2621.

(204) Ardizzone, S.; Bianchi, C. . *J. Electroanal. Chem.* **1999**, *465* (2), 136.

(205) Houssa, M.; Stesmans, A.; Naili, M.; Heyns, M. M. *Appl. Phys. Lett.* **2000**, *77* (9), 1381.

(206) Chen, Y. R.; Zhou, P.; Li, J.; Chen, L. Y. *J. Vac. Sci. Technol. B Microelectron. Nanom. Struct.* **2009**, *27* (3), 1030.

(207) Rauk, A. *Orbital Interaction Theory of Organic Chemistry*, 2nd ed.; John Wiley & Sons, Inc.: New York, USA, 2000.

(208) Hedström, S.; Tao, Q.; Wang, E.; Persson, P. *Phys. Chem. Chem. Phys.* **2015**, *17* (40), 26677.

(209) Wenger, O. S. *Acc. Chem. Res.* **2011**, *44* (1), 25.

(210) Edwards, P. P.; Gray, H. B.; Lodge, M. T. J.; Williams, R. J. P. *Angew. Chemie Int. Ed.* **2008**, *47* (36), 6758.

(211) Seo, Y.; Lee, S.; An, I.; Song, C.; Jeong, H. *Semicond. Sci. Technol.* **2009**, *24* (11), 115016.

(212) Gray, H. B.; Winkler, J. R. *Proc. Natl. Acad. Sci.* **2005**, *102* (10), 3534.

(213) Rath, M. C.; Ramakrishna, G.; Mukherjee, T.; Ghosh, H. N. *J. Phys. Chem. B* **2005**, 20485.

(214) Ramakrishna, G.; Ghosh, H. N. *Langmuir* **2004**, *20* (17), 7342.

(215) Richter, M. M.; Brewer, K. J. *Inorganica Chim. Acta* **1991**, *180* (1), 125.

(216) Tuominen, M. *J. Appl. Phys.* **2000**, *87* (12), 8615.

(217) Chou, A. I.; Lai, K.; Kumar, K.; Chowdhury, P.; Lee, J. C. *Appl. Phys. Lett.* **1997**, *25*, 3407.

(218) Houng, M. P.; Wang, Y. H.; Chang, W. J. *J. Appl. Phys.* **1999**, *86* (3), 1488.

(219) Houssa, M.; Naili, M.; Heyns, M. M.; Stesmans, A. *J. Appl. Phys.* **2001**, *89* (1), 792.

(220) Li, T. C.; Góes, M. S.; Fabregat-Santiago, F.; Bisquert, J.; Bueno, P. R.; Prasittichai, C.; Hupp, J. T.; Marks, T. J. *J. Phys. Chem. C* **2009**, *113* (42), 18385.

(221) McCrory, C. C. L.; Jung, S.; Peters, J. C.; Jaramillo, T. F. *J. Am. Chem. Soc.* **2013**, *135* (45), 16977.

(222) Ahn, H. S.; Yano, J.; Tilley, T. D. *Energy Environ. Sci.* **2013**, *6* (10), 3080.

(223) Zhao, Y.; Vargas-Barbosa, N. M.; Strayer, M. E.; McCool, N. S.; Pandelia, M.-E.;

Saunders, T. P.; Swierk, J. R.; Callejas, J. F.; Jensen, L.; Mallouk, T. E. *J. Am. Chem. Soc.* **2015**, *137* (27), 8749.

(224) Zhao, Y.; Vargas-Barbosa, N. M.; Hernandez-Pagan, E. a.; Mallouk, T. E. *Small* **2011**, *7* (14), 2087.

(225) Nakagawa, T.; Bjorge, N. S.; Murray, R. W. *J. Am. Chem. Soc.* **2009**, *131* (43), 15578.

(226) Busch, M.; Ahlberg, E.; Panas, I. *J. Phys. Chem. C* **2013**, *117* (1), 288.

(227) Xu, P.; Milstein, T. J.; Mallouk, T. E. *ACS Appl. Mater. Interfaces* **2016**, *8* (18), 11539.

(228) Hernández-Pagán, E. a.; Vargas-Barbosa, N. M.; Wang, T.; Zhao, Y.; Smotkin, E. S.; Mallouk, T. E. *Energy Environ. Sci.* **2012**, *5* (6), 7582.

(229) Smith, D. K.; Newkirk, H. W. *Acta Crystallogr.* **1965**, *18* (6), 983.

VITA – Nicholas S. McCool

EDUCATION

Ph. D. Chemistry, The Pennsylvania State University, University Park, PA August 2016

B. A. in Chemistry, Rutgers University of New Jersey May 2011

PUBLICATIONS

11. **McCool, N. S.**; Swierk, J. R.; Nemes, C. T.; Schmuttenmaer, C. A.; Mallouk, T. E. Dynamics of Electron Injection in SnO_2/TiO_2 Core/Shell Electrodes for Water-Splitting Dye-Sensitized Photoelectrochemical Cells. *J. Phys. Chem. Lett.* Submitted.
10. **McCool, N. S.**; Swierk, J. R.; Nemes, C. T.; Saunders, T. P.; Schmuttenmaer, C. A.; Mallouk, T. E. Proton-Induced Trap States, Injection and Recombination Dynamics in Water-Splitting Dye-Sensitized Photoelectrochemical Cells. *ACS Appl. Mater. Interfaces*. Accepted. DOI: 10.1021/acsami.6b05362
9. Swierk, J. R.*; **McCool, N. S.***; Nemes, C. T.; Mallouk, T. E.; Schmuttenmaer, C. A. Ultrafast Electron Injection Dynamics of Photoanodes for Water-Splitting Dye-Sensitized Photoelectrochemical Cells. *J. Phys. Chem. C* **2016**, *120* (11), 5940–5948. (* equal contribution authors)
8. Zhao, Y.; Vargas-Barbosa, N. M.; Strayer, M. E.; **McCool, N. S.**; Pandelia, M.-E.; Saunders, T. P.; Swierk, J. R.; Callejas, J. F.; Jensen, L.; Mallouk, T. E. Understanding the Effect of Monomeric Iridium(III/IV) Aquo Complexes on the Photoelectrochemistry of IrO(x)·nH2O-Catalyzed Water-Splitting Systems. *J. Am. Chem. Soc.* **2015**, *137* (27), 8749–8757.
7. Swierk, J. R.; **McCool, N. S.**; Mallouk, T. E. Dynamics of Electron Recombination and Transport in Water-Splitting Dye-Sensitized Photoanodes. *J. Phys. Chem. C* **2015**, *119* (24), 13858–13867.
6. Swierk, J. R.; Méndez-Hernández, D. D.; **McCool, N. S.**; Liddell, P.; Terazono, Y.; Pahk, I.; Tomlin, J. J.; Oster, N. V; Moore, T. A.; Moore, A. L.; Gust, D.; Mallouk, T. E. Metal-Free Organic Sensitizers for Use in Water-Splitting Dye-Sensitized Photoelectrochemical Cells. *Proc. Natl. Acad. Sci. U. S. A.* **2015**, *112* (6), 1681–1686
5. Saboe, P. O.; Lubner, C. E.; **McCool, N. S.**; Vargas-Barbosa, N. M.; Yan, H.; Chan, S.; Ferlez, B.; Bazan, G. C.; Golbeck, J. H.; Kumar, M. Two-Dimensional Protein Crystals for Solar Energy Conversion. *Adv. Mater.* **2014**, *26* (41), 7064–7069.
4. Swierk, J. R.; **McCool, N. S.**; Saunders, T. P.; Barber, G. D.; Mallouk, T. E. Effects of Electron Trapping and Protonation on the Efficiency of Water-Splitting Dye-Sensitized Solar Cells. *J. Am. Chem. Soc.* **2014**, *136* (31), 10974–10982.
3. Smith, P. F.; Kaplan, C.; Sheats, J. E.; Robinson, D. M.; **McCool, N. S.**; Mezle, N.; Dismukes, G. C. What Determines Catalyst Functionality in Molecular Water Oxidation? Dependence on Ligands and Metal Nuclearity in Cobalt Clusters. *Inorg. Chem.* **2014**, *53* (4), 2113–2121.
2. Swierk, J. R.; **McCool, N. S.**; Saunders, T. P.; Barber, G. D.; Strayer, M. E.; Vargas-Barbosa, N. M.; Mallouk, T. E. Photovoltage Effects of Sintered IrO2 Nanoparticle Catalysts in Water-Splitting Dye-Sensitized Photoelectrochemical Cells. *J. Phys. Chem. C* **2014**, *118* (30), 17046–17053.
1. **McCool, N. S.**; Robinson, D. M.; Sheats, J. E.; Dismukes, G. C. A Co4O4 Cubane Water Oxidation Catalyst Inspired by Photosynthesis. *J. Am. Chem. Soc.* **2011**, *133* (30), 11446–11449.

HONORS AND AWARDS

- Braucher Fellowship for Excellence in Research 2015
- NSF Graduate Research Fellowship in Nanochemistry 2013-2016
- Dan G. Waugh Memorial Teaching Award 2012
- Van Dyke Award for Academic and Research Achievement 2011
- Henry Rutgers Award for Research and Thesis Achievement 2011